Impact Mechanics of PMMA/PC Multi-Laminates with Soft Polymer Interlayers

Joshua Saul Stenzler

Thesis submitted to the faculty of the Virginia Polytechnic Institute and State University in partial fulfillment of the requirements for the degree of

Master of Science

In

Mechanical Engineering

Committee:

Nakhiah Goulbourne, Chair

David Dillard

Alfred Wicks

Timothy Long

November 30, 2009

Blacksburg, VA

Keywords: Impact Mechanics, Gas Gun, Instrumented Impact

PMMA, PC, Thermoplastic Polyurethane, Polyacrylate

Impact Mechanics of PMMA/PC Multi-Laminates with Soft Polymer Interlayers

Joshua Saul Stenzler

ABSTRACT

The main purpose of this thesis is the systematic, experimental investigation of how a soft interlayer affects the impact response and energy dissipation mechanisms of all-polymer multi-laminates. An instrumented, intermediate impact velocity experimental setup with strain rates on the order of 100 s^{-1}, is used to assess the impact mechanics of three-layered samples consisting of a poly(methyl methacrylate) (PMMA) front, polymer interlayer or adhesive, and polycarbonate (PC) back layer. Instrumentation of the gas gun is achieved with a shock accelerometer measuring contact force and optical displacement sensors recording deflection. Previous impact research utilizing instrumented gas guns by Levy and Goldsmith, and Delfosse et al. have measured contact force, but did not record simultaneous out-of-plane displacement. Signals acquired are temporally aligned allowing for insight into the response of the multi-laminate during impact, which is inaccessible with typical gas guns.

Impact testing is completed on bonded and unbonded sample configurations, with two thermoplastic polyurethane and four polyacrylate interlayers. Quantitative metrics from force and displacement signals, along with post-impact damage observations, are used to compare impact performance between configurations and impact velocities (12 and 22 m/s). In general, the presence and bonding of an interlayer increases impact resistance by mitigating and localizing the impact load. The interlayers are characterized at various strain rates in tension, compression, and shear adhesion. In tension, all interlayers display rate dependence, non-linearity, and hysteretic behavior showing varying degrees of increasing energy dissipation with strain rate. Several trends between sample fracture and energy absorption mechanisms, quasi-static and low rate interlayer response, and metric results are established and discussed.

Acknowledgements

I would first like to thank my advisor, Dr. Nakhiah Goulbourne, for her support and guidance throughout my time under her supervision. With an entirely experimental project, it took a lot of patience on both of our parts to take time to instrument the experimental setup, develop correct testing procedure and data acquisition, and finally conduct impact testing. I'd also like to thank my committee members, Dr. Dillard, Dr. Wicks, and Dr. Long.

There are many people who have helped me the past few years at CIMSS. I'd like to start with Beth Howell, who it seemed like I was visiting every few days ordering various things for my research. I'd also like to thank Dr. Inman, who kept me laughing in the lab, for his support and sense of humor. Lastly, all the CIMianSS who were always there for me. Whether it was discussing LabVIEW code, machining, data interpretation, or just talking during down time. I'd also like to acknowledge Danny Reed and Mac McCord from the ESM department who assisted me with using the hot press and various Instrons for material testing.

To the members of Team Unforgivable, thanks for all the fun times in between (and during) work weeks. Kayaking and fishing on the New River, football Saturdays with tailgating and Lane Stadium, intramural football and basketball, road trips, food, and drinks kept me sane when I really needed breaks from classes and research.

Lastly, I'd like to thank my parents for their love and encouragement throughout my life, especially with graduate school. You have always been there for me to listen when things have been tough and celebrate my successes. This graduation is a big accomplishment and milestone in my life, and I'm looking forward to sharing many more with you. I am lucky to have such caring parents to give me guidance and advice. I love you both very much.

I'd also like to acknowledge my funding from ARL: this research was sponsored by the Army Research Laboratory and was accomplished under Cooperative Agreement Number W911NF-06-2-0014. The views and conclusions contained in this document are those of the authors and should not be interpreted as representing official policies, either expressed or implied, of the Army Research Laboratory or the U.S. Government. The U.S. Government is authorized to reproduce and distribute reprints for Government purposes notwithstanding any copyright notation heron.

Table of Contents

List of Figures

List of Tables

Chapter 1

Introduction

Optically clear multi-layered polymer laminates are employed in military defense applications such as transparent armor for personnel protection (visors/shields/goggles) and air/ground vehicle windows. The general requirements for transparent armor are to defeat incoming threats, withstand multiple impacts, and maintain optical clarity with minimal fragmentation and visual distortion for the user [1-3]. A typical configuration of transparent armor consists of multiple tough thermoplastic polymer outerlayers with rubbery interlayer adhesives. For many years, the component materials have consisted of the glassy polymers polycarbonate (PC) and poly(methyl methacrylate) (PMMA) with thermoplastic polyurethane (TPU) adhesives [4-5]. The transparency, toughness, and rate dependence of these three materials are the main reasons they are excellent choices for use in transparent armor to withstand projectile impact. While widely utilized, the impact mechanics of multi-layered, impact resistant, polymer structures is not well understood. Therefore, it is desirable to gain insight into how a low modulus adhesive affects the fracture and energy dissipation mechanisms of the entire composite. A correlation is sought between microstructure and quasi-static material properties of the interlayers to impact performance in order to improve impact t resistance. Correlations of this sort would be useful in tailoring future polymers with superior impact performance. Furthermore, the purpose of this research is to examine the role of the soft interlayer in the impact response of these multi-laminates.

1.1 Motivation

To the author's knowledge, this paper presents the first reported experimental, systematic impact analysis for three-layered multi-laminates consisting of PMMA, a soft interlayer/adhesive, and PC for intermediate impact velocities. Hsieh and Song have reported incident/residual impactor velocities and V_{50} data for high speed impact on layered PMMA/PC composites, but with no interlayer or instrumentation [6-8]. Previous impact testing of monolithic polymer layers has

typically been at low impact velocities (drop towers/pendulum), high impact speeds (large gas guns), and very high strain rate (split Hopkinson pressure bar) material testing. Therefore, a gap exists in the intermediate velocity range for polymer testing. Using a novel instrumented gas-gun setup, the impact response, damage mechanisms, and energy absorption mechanisms are analyzed both quantitatively and qualitatively. In total, six interlayers with varying material properties and microstructures are mechanically characterized using rate dependent tensile, quasi-static compression, and shear adhesion testing. These materials are two TPUs (DF A4700 and IM 800A) and four 3M VHB polyacrylates (VHB 4905, VHB 5925, VHB 4936 and VHB 4930). Nine configurations are impacted (six bonded, two unbonded, and a control without an interlayer) at the two impact speeds of 12 m/s and 22 m/s. Results from this research can help develop a better understanding of the impact mechanics of multi-layered structures. Specifically, how the individual material characteristics of the interlayer affect the overall impact response and damage of the specimen. Quantitative force and displacement metrics, post-impact fracture observations, and quasi-static interlayer mechanical characterization are correlated to impact mechanics.

1.2 Previous Monolithic Material Testing

1.2.1 Interlayer and Outerlayer Characterization

The impact behavior of multi-layered PMMA, PC, and polyurethane (PU) adhesive laminates has been minimally studied [4-5, 9-10], but on the other hand, polymer monolithic high strain rate response has been studied extensively. Several researchers have conducted compression testing on polyurethanes from quasi-static to very high strain rates and observed strong rate dependence [11-13]. Qi and Boyce, Yi et al., and Sarva et al. completed uni-axial cyclic compression testing over seven decades of strain rate (0.001–10000 s^{-1}) and observed a highly non-linear response, strong rate dependence, hysteresis, cyclic softening, and residual strains following unloading. Using a high speed tensile test instrument, Roland et al. were able to show that polyurethanes display strong rate dependence through a large range of strain rates in tension as well [14].

For the outerlayers PMMA and PC, many researchers have demonstrated that the Young's modulus, yield stress, and strain hardening rate are dependent on the applied strain rate [15-26]. Although both PC and PMMA appear similar (comparable transparency and density), their monolithic high strain rate responses are quite different. Fleck, Stronge, and Liu, Blumenthal et al., Li and Lambros, Mulliken and Boyce, and Richeton et al. conducted quasi-static Instron compression testing (10^{-5}–10 s^{-1}) and dynamic high strain rate impact testing (10^{3}–10^{4} s^{-1}) on individual samples of PC and PMMA and have shown that the polymers respond in contrasting ways for various strain rates. These researchers mainly characterized strain rate dependence without reporting failure mechanisms for different deformation rates.

1.2.2 PC and PMMA Impact Testing

Widespread research on the impact response and fracture mechanisms of monolithic PC and PMMA, including various additives and additional material layers, has been conducted with high speed gas guns. Three important observations made about PC are that failure was ductile in nature, impact resistance increased with thickness and, based on specimen geometry, deflection is a main mode of impact energy absorption [10, 24-25, 27-31]. Radin and Goldsmith demonstrated superior polymer impact performance when comparing PC and Aluminum samples of similar areal densities. They concluded that the polymer exhibited a "15% greater perforation resistance" than the metal's for the velocity range of 50–210 m/s [32]. Substantially less research has been conducted on monolithic PMMA. Both Rittel and Moy et al. found that when dynamically loading PMMA disks at high strain rates (3000–15000 s^{-1}), it behaved as a brittle material able to withstand a relatively small threshold of plastic deformation before complete fracture [33-34]. Sarva et al. used a single stage gas gun with impact velocities of 300–550 m/s to verify the brittle and ductile behavior of PMMA and PC respectively using high speed photography [35]. Despite the plethora of results published, there is a gap in strain rates that hasn't been examined. Testing has been completed at the two extreme ends of the strain rate spectrum, but intermediate rate impact has been largely unexplored. Therefore, this research aims to gain insight into the impact mechanics of PMMA and PC during intermediate impact velocity testing when incorporated into multi-laminates with soft, polymer interlayers. Toqueboeuf et al. conducted both experiments and modeling of PC and polyurethane multi-

layered samples [9]. In order to completely understand impact behavior of multi-layered polymers, both individual components, as well as the complete structural response, must be characterized. Although both individual impact responses of monolithic PC and PMMA have been researched, it is important to analyze PC/PMMA polymers in the form of sequentially layered with adhesives, coextruded, or hybrid multi-layered structures.

1.3 Combined PC/PMMA Material Testing

1.3.1 Monolithic vs. Hybrid/Coextruded Polymers

It has been established that the impact response of PMMA and PC are quite different, but both have high impact resistance (with adequate thickness). Typical transparent armor consists of several optically clear layers, with each material serving a purpose. Using a high-velocity impact device (100–520 m/s), Song and Hsieh tested monolithic samples of PC and PMMA as well as hybrid co-extruded PC/PMMA composites. They found that for all velocities, PC failed in a ductile manner while PMMA failed in a brittle manner for low velocities, developing increased localized fracture at higher velocities. When using the V_{50} (velocity at which complete target perforation occurs 50% of the time) of the specimens as a metric, the hybrid composite PMMA/PC performed better than monolithic PC or PMMA for the tested total thicknesses [8, 36]. This widely used metric is of limited value since it is indicative of perforation resistance but provides no insight into the mechanics of the response. Song and Hsieh found that overall impact resistance is improved, when compared to monolithic PMMA and PC, for a hybrid system with a brittle PMMA front layer and ductile PC backing. The superior impact performance of the PMMA/PC hybrid system is due to the different ways each component material absorbs impact energy. When combining these two polymers with dissimilar high rate responses, the PMMA acts as a sacrificial layer with the PC behaving as an energy absorber resulting in increased impact performance. Due to complexities arising from interactions between layers with differing impact responses, component materials, layering order, and thicknesses all need to be considered for enhancing a composite's impact performance. For example, it was concluded that the overall impact response of coextruded PMMA/PC was dominated by PMMA; it was more dependent on the thickness of PMMA than that of PC [7].

This implies that in order to maximize the impact performance of a multi-layered polymer, it is vital to obtain a thorough understanding of each layer's role and its effect on adjacent materials. Stress wave propagation is also modulated, with amplitudes attenuated, by boundary interference arising from neighboring layers with dissimilar component material impedances. Note that Song and Hsieh's hybrid PMMA/PC samples are coextruded with no interlayer and may be considered an integrated polymer.

1.3.2 Impact Response of Multi-Layered Composites

In a multi-layered system, an individual layer's response is dependent on its own material properties as well as that of the adjacent layers [37]. For PMMA/PC composites, the brittle and ductile layers work synergistically to improve impact resistance, although the specific mechanisms yielding this performance enhancement are not well understood. Furthermore, the specific mechanisms responsible for improved performance of a multi-layered structure bonded by polymeric adhesive layers are not known. In order to improve understanding, there have been research efforts to investigate the impact performance and failure modes of multi-layered glass, metal, opaque polymer, and fiber reinforced composites [38-41], but few have examined multi-layered composites consisting of only polymers. Some researchers have studied the impact performance of optically clear co-extruded PC/PMMA [7, 42] and various configurations of PC, PMMA, polyurethane (PU) and glass in multi-laminate composites [6, 43]. These impact tests were conducted at high impact velocities (greater than 200 m/s) but did not record contact force or deformation, with post impact visual inspection and V_{50} used as performance metrics. Using the V_{50} metric is very "expensive" as it requires many target specimens, iterations, and time. Therefore, other methods and metrics for quantifying impact performance are more desirable. With advancements in modeling capabilities, Fountzolus et al. were able to simulate impacts on samples with the stacking sequence of PC/PU/PMMA/PU/PC. When comparing to the previous experimental work of Hsieh [6], they were able to accurately predict V_{50} values and crack propagation/fracture shapes observed after impact [44]. Post-impact damage analysis and numerical prediction is helpful in determining what modes of failure exist and which energy absorption mechanisms are pronounced. However, capturing information during the impact can contribute greatly to understanding the dynamic response, impact mechanics, and specific energy

absorption mechanisms, as well as validate numerical models [45-46]. Therefore, it is beneficial to have an instrumented experimental setup capable of recording data during impact that can be analyzed after testing is complete. A unique experimental setup capable of accomplishing this has been developed in this research and is described in Chapter 4.

1.4 Instrumented Testing at Various Strain Rates

1.4.1 Very Low to Low Impact Velocities

For impact testing at low velocities (typically less than 8 m/s), instrumentation of an impactor can be accomplished in several ways. The two most common instrumentation methods are drop towers and pendulums, which use load cells or strain gauges in instrumented tups [47-54]. Both of these methods are typically employed to study a sample's structural response. Impact velocities are low because the speed is dependent on the height from which the impactor is released and is restricted by the size of the experiment. In some cases, they are only capable of an individual impact velocity. Other methods utilized for low speed instrumented impact are pendulum/drop tower Charpy and Izod tests, which characterize fracture toughness of notched specimens. The idea behind these approaches is that all materials contain flaws and micro-cracks, and that valid metrics for sample comparison are resistance to crack propagation and energy required to expand cracks [55]. Some issues with these tests include: fluctuating stress intensity factors, excitation of natural frequencies of specimen and/or clamping system, and subsequent lack of constant loading rate [56]. Ultimately, these tests have been misinterpreted and used as indicative of ballistic response as opposed to their intended use: to characterize notch sensitivity.

1.4.2 Intermediate to High Impact Velocities

Several researchers have conducted instrumented impact testing at slightly higher velocities using a hydraulically driven mechanism [57-58]. Both Kamal et al. and Peraro developed hydraulically powered, rheometric impact testers capable of variable speeds (0.0127 m/s–12.7 m/s) that can record contact force and displacement at the impact site. Hydraulic ram driven

impact devices have even been able to approach speeds of 20 m/s [59], but in order to achieve higher impact velocities, compressed air launched projectiles (gas guns) are necessary. Gas guns, consisting of a barrel, valve, regulator, and pressurized gas can be fabricated in many different sizes. Most are built quite large in order to obtain high impact speeds and are focused on impact velocity more than instrumentation. Typically, these experimental setups are unable to measure contact forces or sample deflection. They rely on analysis through measuring V_{50}, incident/residual impactor velocities to characterize energy dissipation, and post-impact visual inspection [6-8, 28, 32, 38-39, 60-63]. Due to signal transmission issues as well as the intensity of collisions, possible target perforation, and resulting fracture of high speed impact, instrumentation can be difficult and dangerous for both sensors and users. Therefore, only several research groups have attempted instrumentation of gas gun projectiles. Delfosse et al. used a 1.83 m long gas gun (44.5 mm inner diameter) capable of intermediate impact velocities of 7–50 m/s with a piezoelectric accelerometer instrumented impactor [64]. Their projectile had a trail wire leading to a digital oscilloscope as well as a relief valve to prevent double impact and to facilitate rebound of the impactor back into the launch tube. Optical sensors near the end of the barrel measured impact velocity. Levy and Goldsmith's gas gun was 1.37 m long with interchangeable barrels of inner diameters 6.35 and 12.7 mm capable of impact velocities from approximately 25–300 m/s. A silver-plated X-cut quartz disc instrumented the projectile and the signal is read by an oscilloscope [65]. For both instrumented gas guns, calibration is required for the load cells based on the masses ahead and behind the transducer. This is unnecessary for this research as the supplier of the load cell implemented (Section 4.1.2) provides a calibration factor calculated for the internal seismic mass of the shock accelerometer.

1.4.3 Very High Strain Rate Material Testing

To reach the realm of very high strain rate instrumented material testing, a method was developed based on the original work of Kolsky [66] and is called a Kolsky Bar or split Hopkinson pressure bar (SHPB). This experimental setup, considered a material and not a structural test, is used to determine a material's constitutive stress-strain response for very high strain rates. A SHPB uses strain gauges to measure incident, transmitted, and reflected stress waves as they propagate through a specimen and are modulated at dissimilar interfaces. In order

to correctly implement a SHPB and measure a material's stress/strain constitutive relationship, several assumptions need to be made and enforced in experimental practice, most notably that of linear elastic wave propagation. It is assumed that the specimen is a linear, elastic, isotropic material with a homogeneous stress distribution during testing (not multiple materials) and similar impedance to the incident/transmission bars.

1.5 Effect of a Soft Interlayer on Multi-Layered Samples

Tasdemirci and Hall used a SHPB for intermediate velocity (10–23.5 m/s) impact testing on 16 mm diameter, three-layered ceramic/EPDM (ethylene propylene diene M-class) rubber/composite specimens. The testing of multi-layered samples consisting of materials of varying impedances violates the necessary assumptions used for data reduction (as specified above). Therefore, the researchers used the SHPB in an atypical manner to analyze stress wave magnitudes and how they correspond to outlerlayer damage. Similar to this research, their main focus was to observe how the low modulus interlayer affected fracture and stress wave propagation through the multi-layered samples. Simulations and experimental results show that the inclusion of the rubber layer significantly increased the fraction of the incident stress wave that was reflected [67]. The stress in the direction of wave propagation was also greatly reduced in the ceramic (front) and composite (back) with the introduction of the rubber interlayer. This will be referenced in the fracture analysis for similar configurations in this research: unbonded two-layered PMMA/PC and three-layered PMMA/TPU/PC (Sections 5.2.1 and 5.2.2). Decreased stresses in the outerlayers are an indication of improved impact performance as the outerlayers are less likely to deform plastically causing fracture. However, it is noted that as the rubber interlayer is compressed considerably, its impedance rises resulting in increasing wave transmission to the composite backing. As this occurs, highly inhomogeneous stress distributions throughout the component materials occur.

1.5.1 Constrained vs. Unconstrained Interlayer

Tasdemirci and Hall completed similar SHPB tests on three-layered samples with two different low modulus interlayers, EPDM rubber and expanded Teflon foam. They compared results for

both laterally constrained and unconstrained unbonded interlayers. Similarly in this research investigating the effect of semi-constrained (bonded) and unconstrained (unbonded) boundary conditions in three-layered multi-laminates is investigated (through-thickness constraints). It was confirmed with previous research by Gama et al. that a low modulus interlayer slightly attenuates and delays wave transmission to a backing plate, while a higher modulus interlayer (similar to outerlayers) facilitates wave transmission [68]. SHPB impact at 20.5 m/s on a ceramic/EPDM rubber/composite showed that an unconstrained rubber interlayer resulted in more reflection and less transmission of stress waves than a constrained rubber interlayer [69]. In general, for both EPDM rubber and Teflon interlayers, the constrained three-layered samples were less likely than unconstrained samples to cause fragmentation in the front ceramic layer. This is due to reduced compressive stress wave reflection at the ceramic/interlayer interface. Note that in typical military applications, the true boundary conditions of a bonded interlayer in structural transparent armor are assumed to be between fully constrained and unconstrained [69-70]. Tasdemirci and Hall's research gives insight into the complexities of stress wave propagation and inhomogeneous stress distributions occurring in a multi-layered sample. These are particularly pronounced for unbonded multi-layered systems with a low modulus interlayer. While the current experimental setup's impact velocities are similar to Tasdemirci and Hall (12 and 22 m/s), the soft interlayers in this research are implemented in multi-layered polymers for bonded and unbonded configurations. In this case, the bonding of layers increases the interfacial shear strength at the material interfaces imitating a semi-constraint boundary condition on the adhesive. Furthermore, this work assesses the structural response of multi-layered polymer panels due to normal impact applied at the center of the samples with a hemi-spherical impactor.

1.6 Summary and Organization

The focus of this research is a multi-layered, all-polymer composite consisting of PMMA and PC outerlayers with a soft elastomeric interlayer. Six interlayers consisting of two rubbery TPU interlayer/adhesives and four 3M VHB polyacrylates are utilized. To the author's knowledge, this is the first published account to systematically quantify and qualify the effect of a rubbery interlayer on the impact mechanics of an all-polymer multi-laminate. A soft adhesive is used to bond the PMMA to PC, potentially enhance multi-hit capability by maintaining panel integrity,

and reduce impact damage. The specific goal of this thesis is to determine the effect of different interlayers on the normal impact response of multi-laminates for two impact velocities: 12 and 22 m/s. Correlations are determined between quasi-static and low rate responses of the interlayers with impact performance and observed energy dissipation mechanisms. The interlayers are mechanically characterized in three ways: tension at three strain rates, quasi-static compression, and quasi-static shear adhesion testing. In this research, the experimental setup is similar to those developed by to Delfosse et al. and Levy and Goldsmith, with additional sensors for measuring displacement [64-65]. Impact testing of the panels is completed using a single stage, fully instrumented gas gun capable of recording force at the impact site and off-center displacement during the impact event. A shock accelerometer embedded in the impactor measures contact force, while optical displacement sensors monitor deflection. By implementing a common "zero" triggering time for the sensors, force and displacement traces are aligned temporally and can be superimposed in order to give insight into loading conditions during panel deflection and rebound. The impact response of the specimens is quantitatively analyzed using ten force and displacement metrics. Force metrics include: force peak values, loading rate, loading pulsewidth, and impulse. Displacement metrics include: out-of-plane deflection, transient response frequency, 2% settling time, and decay rate. Post impact visual inspection of nine impacted configurations of multi-laminates at two impact velocities evaluates impact performance and compares fracture mechanisms. Mechanical characterization of the interlayers, quantitative force and displacement metrics, and energy absorption mechanisms trends are related to observed damage and impact mechanics.

This paper is organized into 7 chapters. Mechanical characterization of the six interlayers, are outlined in Chapter 2. In Chapter 3, bonded and unbonded multi-laminate assembly methods are described. Chapter 4 discusses the instrumented experimental setup operation, data acquisition, and LabVIEW VI procedure. Force and displacement time traces during impact are reported, and energy dissipation mechanisms and fractography analysis are summarized in Chapter 5. In Chapter 6, quantitative results from the impact tests regarding force and displacement metrics are summarized and compared for interlayer, impact velocity, and bonding condition. Finally, a thesis summary, research conclusions, and future work suggestions are given in Chapter 7.

Chapter 2

Material Characterization

This chapter discusses the mechanical characterization of the component materials of the multi-laminates. In the multi-layered polymer samples, the outerlayers are composed of commercially available glassy polymers PC and PMMA. These materials have been extensively researched through a wide range of strain rates in compression and different impact velocities (Section 1.2.2). In total, six adhesives/interlayers are mechanically characterized. These include two thermoplastic polyurethanes: Deerfield A4700 (DF A4700), Inter Materials 800A (IM 800A) and four 3M polyacrylates (VHB 4905, VHB 5925, VHB 4936, and VHB 4930). The methods for conducting tensile, compression, and shear adhesion testing on the interlayers are outlined. Material properties (measured and supplied) are shown in Table 2.1. Glass is included for comparison purposes with the optically clear PMMA and PC polymer substitutes. Glass has a significantly larger tensile elastic modulus, density, and glass transition temperature, with a smaller Poisson ratio. Glass transition temperatures (T_g) are measured using dynamic mechanical analysis for the TPUs (Section 2.1.1) and are supplied for the remaining materials.

Table 2.1 Reported and measured interlayer material properties

Material	As Received Thickness (mm)	Tensile Elastic Modulus (MPa)	Poisson Ratio	Density (kg/m^3)	T_g (ºC)
Glass	N/A	7750	0.196	2600	560
PMMA	1.5875	3378	0.375	1190	114
PC	1.5875	2344	0.38	1200	145
DFA4700	0.635	5.12	0.49	1080	-23.4
IM800A	0.635	3.16	0.49	1040	-51
VHB4905	0.5	0.127	0.49	960	-40
VHB5925	0.635	0.351	0.49	590	-45.6
VHB4936	0.635	0.559	0.49	720	-34.4
VHB4930	0.635	0.553	0.49	800	-34.4

2.1 Component Material Microstructure and Properties

PMMA and PC are two optically clear, amorphous polymers typically utilized as an alternative to glass. These thermoplastic polymers are less expensive, easier to manufacture and mold, and have superior impact resistance when compared to glass. As shown in Figure 2.1.1a, polycarbonate consists of organic building blocks, such as bisphenol A (BPA), linked by carbonate groups (O-(C=O)-O). The monomer used for synthesis of poly(methyl methacrylate) is shown in Figure 2.1.1b.

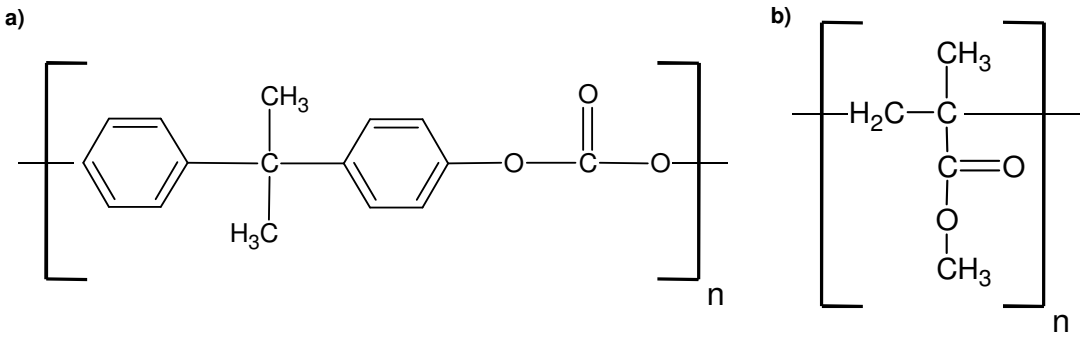

Figure 2.1.1 Chemical structures of a) polycarbonate of BPA and b) poly(methyl methacrylate)

As shown in Figure 2.1.2, thermoplastic polyurethanes are segmented block copolymers with a unique two-phase microstructure consisting of amorphous soft and crystalline hard segments [11, 71]. This allows TPUs to be highly customizable allowing for material properties and characteristics ranging from soft elastomers to tough thermoplastics and can be tailored to best suit the intended use. The basic chemical structure of polyurethane is shown in Figure 2.1.3a.

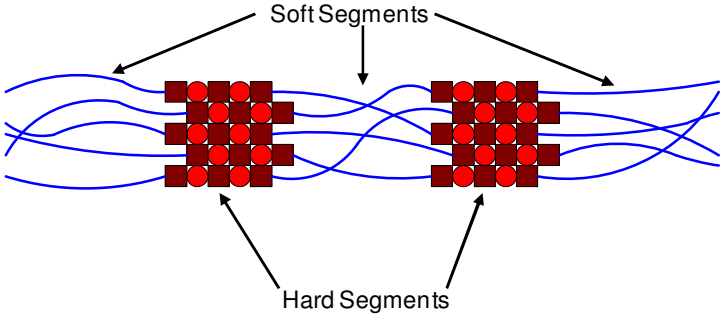

Figure 2.1.2 Schematic illustrating two-phase structure of TPUs

The VHB interlayers are soft, polyacrylates of varying colors and conformabilities with the chemical structure of the acrylate monomer shown in Figure 2.1.3b. They are all commercially available from 3M. All materials are used in as-received condition, where the TPU interlayers tested are tacky after a heat/pressure treatment and the 3M adhesives are tacky at room temperature. Since all component materials are polymers displaying strain rate dependence, the moduli of the TPUs and VHB polyacrylates are calculated from the linear portion of the quasi-static tensile testing results (strain rate of 0.01 s^{-1}) discussed in Section 2.2. The Poisson ratio for representative TPUs was calculated by MacAloney and Goulbourne experimentally, and reported by 3M for the VHB polyacrylates, to be approximately 0.49 [72]. This value is typical for elastomeric, rubbery materials and reflects near incompressibility. Note how close the densities of PMMA and PC, and DF A4700 and IM 800A are in magnitude, with dissimilar tensile elastic moduli resulting in quite differing acoustic wave speeds. Outlined in Table 2.1, properties for the four VHB polyacrylates vary substantially, although VHB 4936 and VHB 4930 have comparable values for tensile modulus (0.559/0.553 MPa) and density (720/800 kg/m^3). As discussed in Chapter 1, the outerlayers PMMA (predominantly brittle) and PC (ductile) exhibit strong strain rate dependence, and the remainder of this chapter will show how the interlayers respond to various strain rates and loading modes.

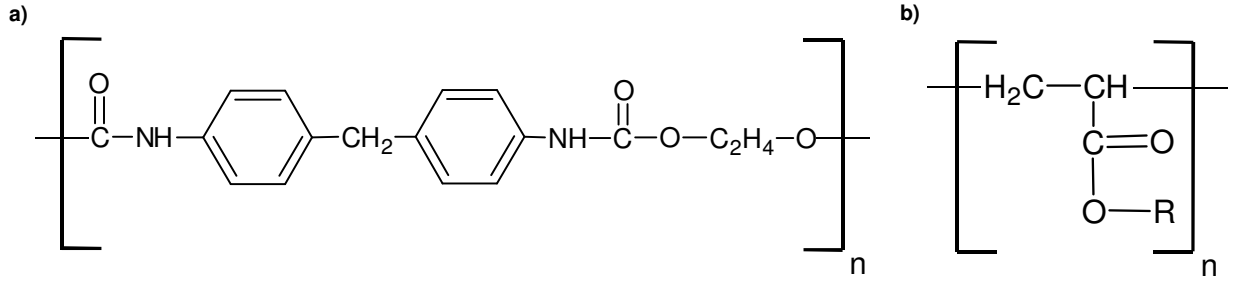

Figure 2.1.3 Chemical structures of a a) polyurethane and b) polyacrylate

Through communication with a 3M technical service scientist and visual inspection using an Omano OM3344 stereo microscope, the microstructure of each material is visualized and components are identified. Despite a common acrylic matrix material, the VHB polyacrylates have quite differing microstructures. Representative schematics of the four polyacrylates are shown in Figure 2.1.4. These pictures are taken of the top surface of the VHB polyacrylates at a

zoom of 45 times to see the microstructure (Figure 2.1.5). Note that VHB 4905 has no appreciable microstructure because it is a solid acrylic adhesive and can be considered incompressible (Figure 2.14a and Figure 2.1.5a). VHB 5925 has collapsible air bubbles of varying sizes (~100 µm) with a distribution of approximately 44.4 per mm^2 and therefore is considered somewhat compressible (Figure 2.1.4b and Figure 2.1.5b). VHB 4930 is similar to VHB 4905 in that it is solid acrylic and can be considered incompressible, but has rigid microspheres of equal diameter (~70 µm) dispersed at approximately 100 per mm^2 (Figure 2.1.4c and Figure 2.1.5c). Like VHB 5925, VHB 4936 has compressible spaces but also has the microspheres similar to VHB 4930 (Figure 2.1.4d and Figure 2.1.5d). In summary, VHB 4905 and VHB 4930 may be considered incompressible with a solid acrylic structure, VHB 5925 and VHB 4936 are compressible with collapsible air gaps/bubbles, and VHB 4936 and VHB 4930 have rigid microspheres incorporated into the acrylic matrix.

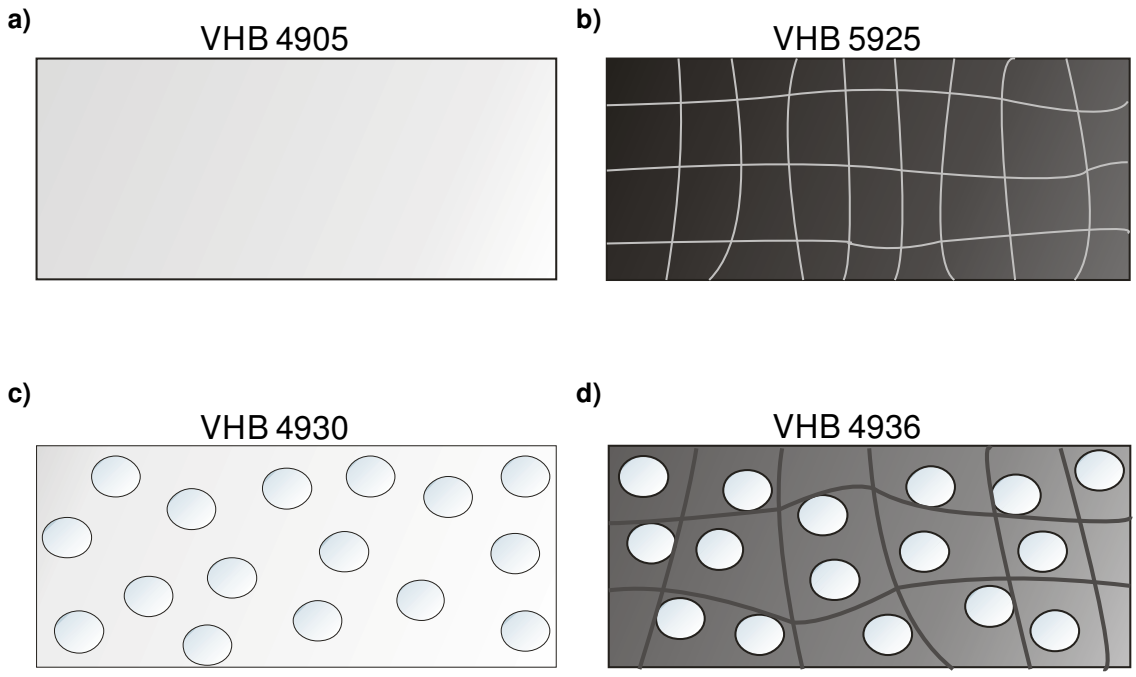

Figure 2.1.4 Schematics of microstructure of VHB a) 4905, b) 5925, c) 4930, and d) 4936

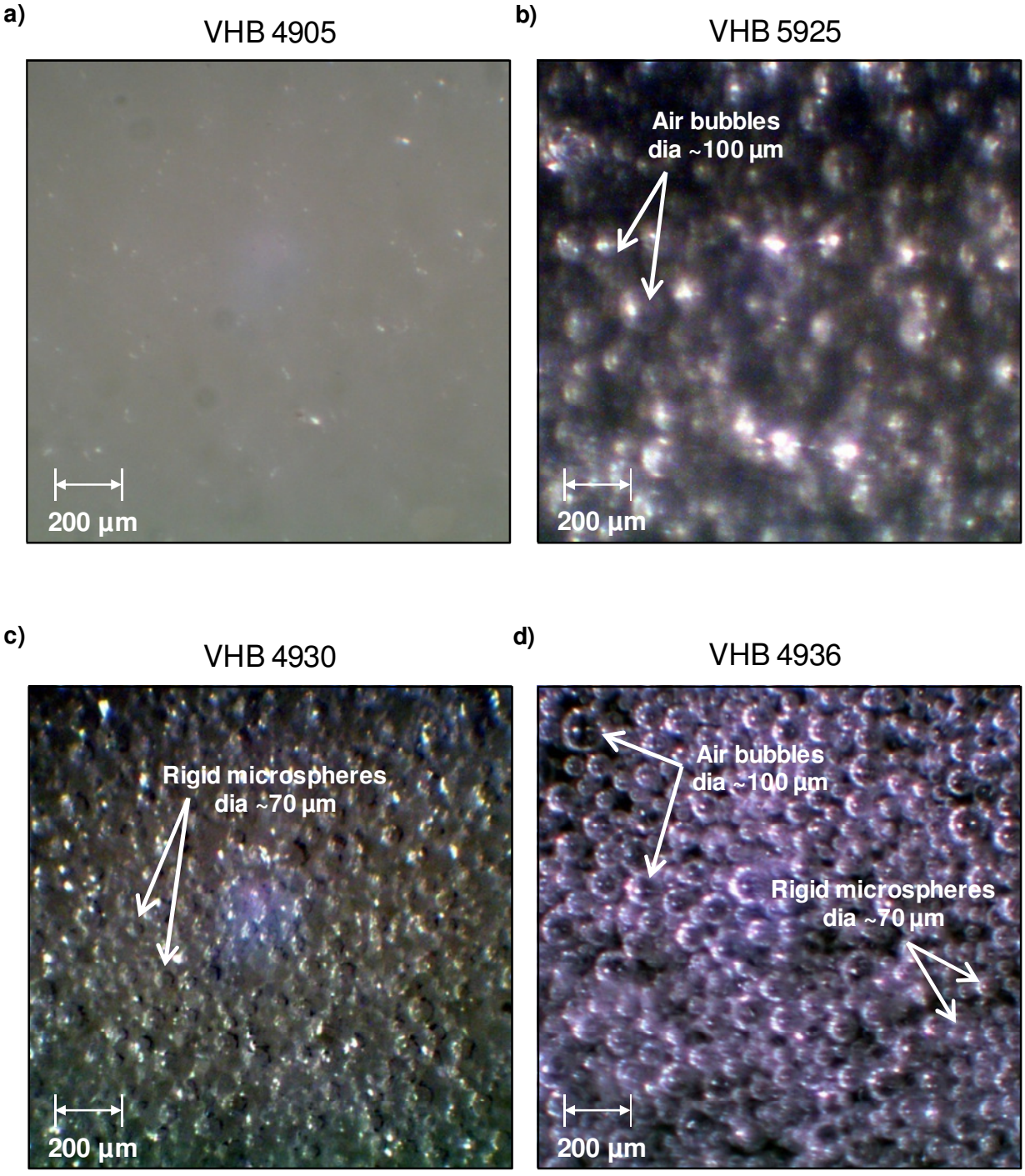

Figure 2.1.5 Stereo microscope microstructure pictures (45X of 1.5 mm square sections) of a) VHB 4905, b) VHB 5925, c) VHB 4930, and d) VHB 4936

2.1.1 Dynamic Mechanical Analysis (DMA)

Dynamic mechanical analysis (DMA) provides insight into how a material responds under high rates of loading when the viscosity is high at low temperatures, as well as how this response changes as temperature is slowly increased. Rectangular samples are cyclically loaded (1 Hz) in tension to small strains from -150 to 100°C at a rate of 5°C/min using a TA Instruments DMA Q800. Figure 2.1.6a–c shows the storage modulus, loss modulus, and tangent delta traces as a function of temperature. Storage modulus (E') is indicative of the elastic response of the material, the loss modulus (E") is representative of the energy loss in internal motion, and the tangent delta (response phase delay) can be described as the "damping" of the material (E"/E'). From this data, the glass transition temperature (T_g) can be approximated in three ways: temperature at which the storage modulus begins to decrease, and the peaks of the loss modulus or tangent delta traces. Results in Figure 2.1.6d show that these values can significantly vary between methods of T_g measurement. No loss modulus peak is observed for DF A4700, so a T_g for that method is not reported. Data is unavailable for the three remaining polyacrylates, but as shown in Table 2.1, the supplied VHB T_g's are comparable. Note that the value for VHB 4905 is 16 degrees lower than the experimental T_g from the storage modulus. DMA strains are typically less than 0.001, therefore it is advantageous to also consider cyclic tensile loading since it shows the non-linear large deformation response not achievable in DMA. Linear time-temperature superposition is not anticipated to be useful for these materials given their non-linear behavior and large deformations as it was not considered in a rigorous manner in this work.

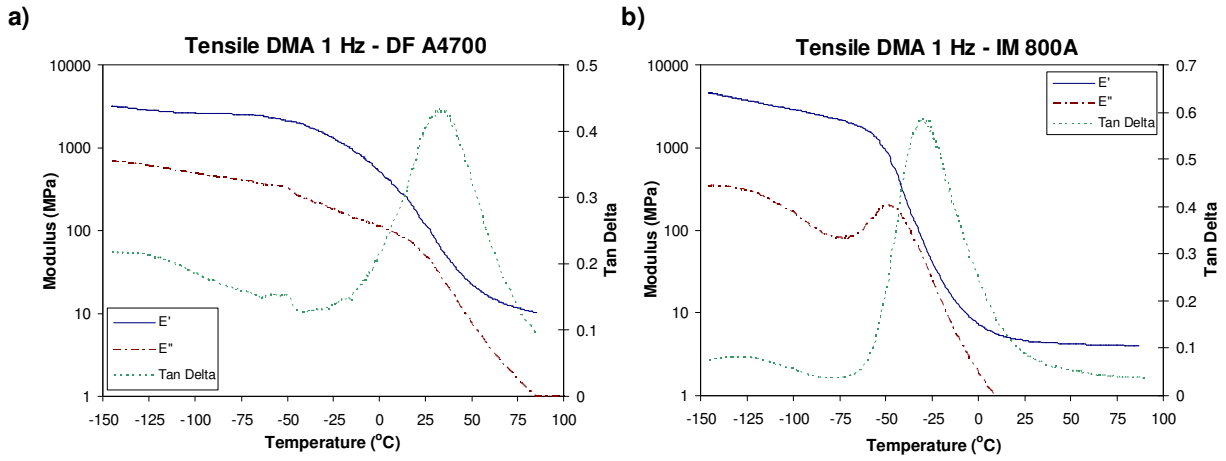

c)

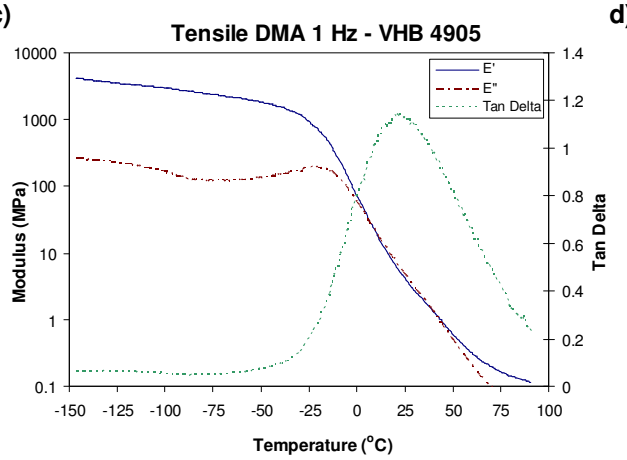

d)

Interlayer	Glass Transition Temp (°C)		
	Storage	Loss	Tan(δ)
DF A4700	-23.4	N/A	33.5
IM 800A	-51	-48.9	-29.2
VHB 4905	-24	-22.1	22.4

Figure 2.1.6 Tensile DMA results at 1 Hz for a temperature sweep of -150–100ºC at 5ºC/min for the thermoplastic polyurethanes a) DF A4700 and b) IM 800A, and c) the polyacrylate VHB 4905, with a d) glass transition temperature summary table

2.2 Tensile Testing

As a baseline comparison for the six interlayers, tensile testing is completed at three different strain rates (0.01, 0.1, and 1 s^{-1}). Dogbone samples are cut using an ASTM standard die (D-638 Type IV) and mechanical press from Qualitest. If a rectangular test specimen were used, the strain in the sample cannot be considered uniform. The dogbone shape allows us to assume that, for the 15×3.175 mm rectangular gauge length, that there is uniform strain. Samples are loaded to a strain of 1.0 (15 mm) and then unloaded back to the starting position. An Instron ElectroPULS with a 250 N load cell is used for the TPUs (all rates) and highest rate VHB testing (1 s^{-1}). An Instron 5848 Micro-tester with a 50 N load cell is used for the lower rate VHB testing. Note that the Instron's crosshead displacement, not an extensometer, is used to calculate strain due to the large deformations tested. This is important because it is assumed that the dogbone facilitates a mostly uniform elongation of the gauge length of the polymer. For small strains, an extensometer should be utilized (especially for polymers) to measure the actual elongation of a very small material section. Figure 2.2.1 shows the tensile testing results (engineering stress as a function of strain) for the six interlayers at three strain rates, with each trace being the average of eight samples. Note the stress unit difference between the two less compliant TPUs (MPa) and the four softer VHB polyacrylates (kPa).

It is clear from these results that all six materials are non-linear and have strong rate dependence, hysteresis, strain softening, and residual strains. As the strain rate increases, the compliance decreases as the soft material is stretched at faster rates. It is also observed that for all of the materials, except IM 800A and VHB 5925, as strain rate increases the residual strain increases as well. Note this is not plastic strain as some is recovered with time, but is more indicative of the strain at which the sample is no longer in tension, or buckles over, during unloading. A summary of residual strains and stress recorded at a strain of 1.0 for each interlayer and strain rate is given in Table 2.2. For the four interlayers that showed increasing residual strain with strain rate, two trends were observed. The residual strain increments between strain rates 0.1 s^{-1} and 1 s^{-1} for DF A4700 and VHB 4905 are approximately double that between strain rates of 0.01 s^{-1} and 0.1 s^{-1}. For VHB 4936 and VHB 4930, the residual strain increments between strain rates 0.01 s^{-1} and 0.1 s^{-1} are approximately equal (0.05), but the increments between strain rates 0.1 s^{-1} and 1 s^{-1} are different (0.025 and 0.042 respectively). Note the interlayers' order of increasing tensile compliance is: DF A4700, IM 800A, VHB 4936/4930, VHB 5925, and VHB 4905. To visualize how interlayers compare at various strain rates, Figure 2.2.2 shows the plots for each. It is observed that VHB 4936 and VHB 4930 have similar responses for all strain rates.

Table 2.2 Residual strain and maximum stress summary

	Residual Tensile Strain			**Stress at Strain of 1 (kPa)**		
Interlayer	**0.01 s^{-1}**	**0.1 s^{-1}**	**1 s^{-1}**	**0.01 s^{-1}**	**0.1 s^{-1}**	**1 s^{-1}**
DF A4700	0.08	0.103	0.145	3051	3551	4599
IM 800A	0.064	0.059	0.056	2303	2464	2598
VHB 4905	0.143	0.201	0.298	55.58	73.76	109.2
VHB 5925	0.397	0.31	0.196	68.21	118.5	210.2
VHB 4936	0.241	0.292	0.317	207.4	308.2	428.6
VHB 4930	0.274	0.326	0.368	187.8	309.0	443.4

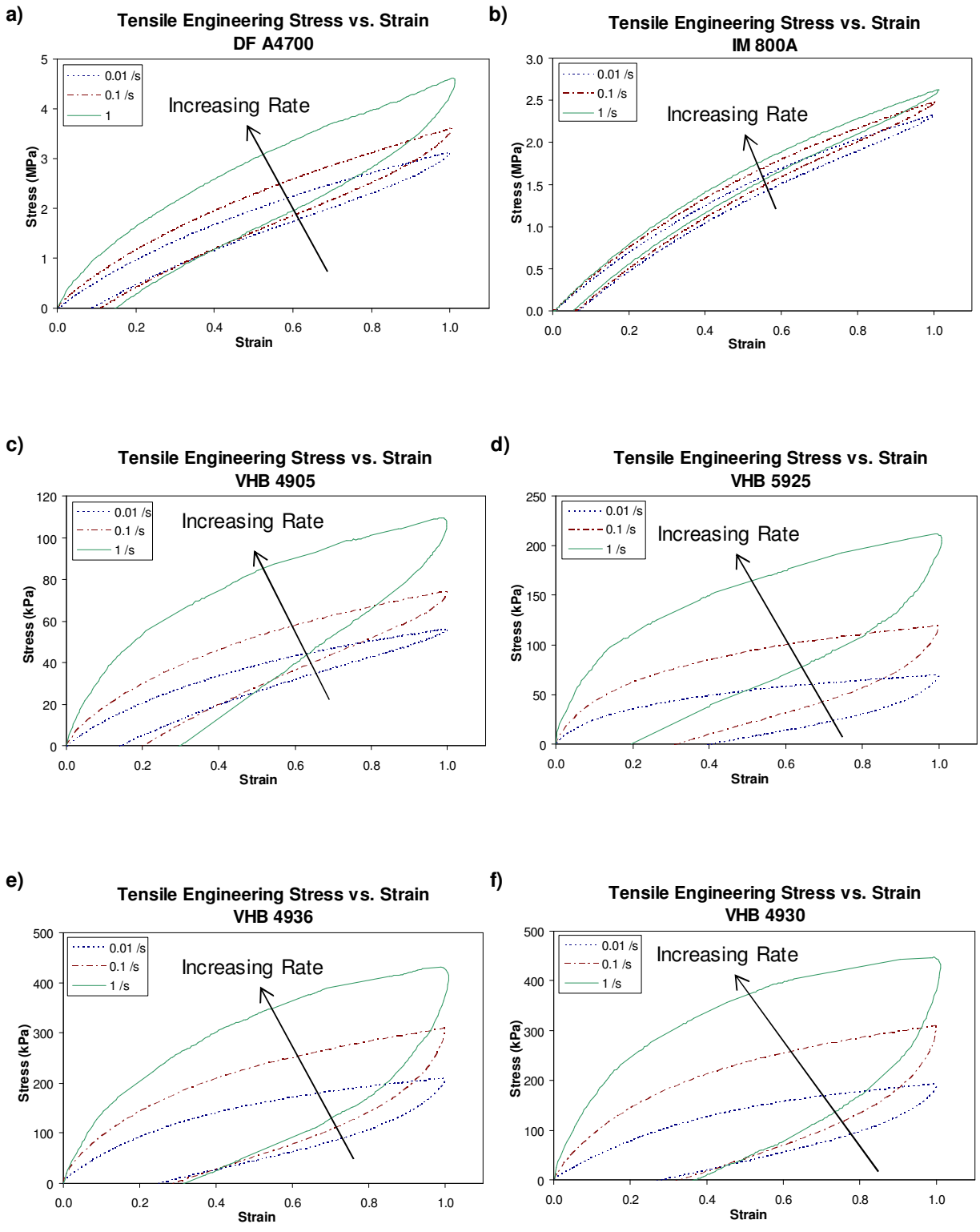

Figure 2.2.1 Engineering stress as a function of strain for three strain rates (0.01, 0.1 and 1 s^{-1}) of a) DF A4700, b) IM 800A, c) VHB 4905, d) VHB 5925, e) VHB 4936 and f) VHB4930

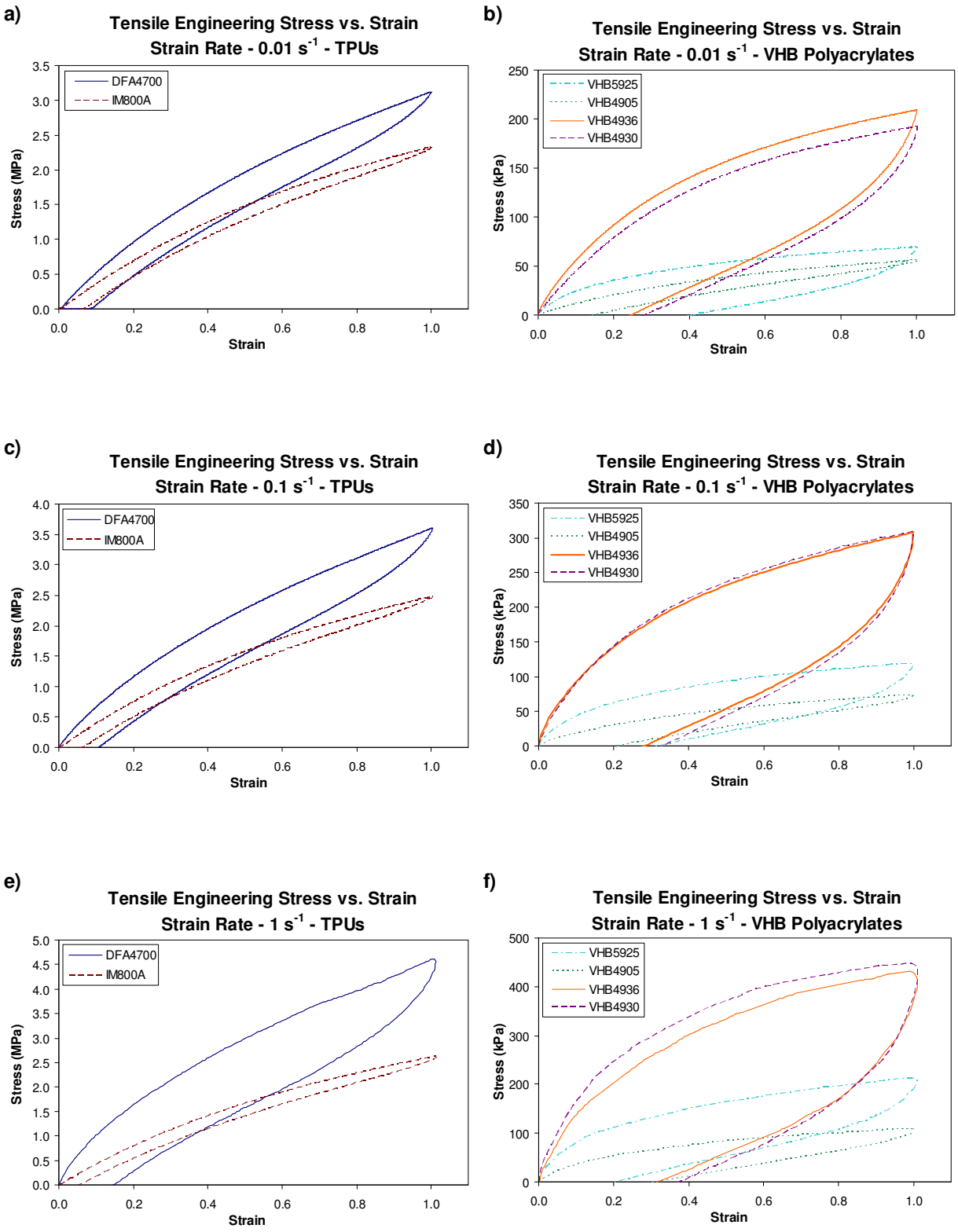

Figure 2.2.2 Engineering stress as a function of strain for three strain rates: 0.01 s^{-1} a) TPUs and b) polyacrylates, 0.1 s^{-1} c) TPUs and d) polyacrylates, and 1 s^{-1} e) TPUs and f) polyacrylates

To quantify the traces shown in Figure 2.2.2, plots of true stress as a function of strain are plotted for loading (Figure 2.2.3) and unloading (Figure 2.2.4) of interlayers in tension. For each strain rate, engineering stress values are recorded for strain increments of 10% from 0.1 to 1.0. Note that engineering stress is converted to true stress using conservation of volume and incompressibility assumptions for this strain range. Although VHB 5925 and VHB 4936 have compressible air gaps in their microstructures, the incompressibility approximation can be maintained for tensile loading through this small strain. As expected, stress values for a given strain increase with strain rate during loading for all materials reflecting rate dependence (Figure 2.2.3). It is apparent that the TPUs increase in stress is relatively the same increment for all strain rates with nearly parallel traces for each strain measured. VHB polyacrylates show an increasing stress increment with strain rate, resulting in an observed "spreading" of strain traces going from 0.01 s^{-1} to 1 s^{-1}. While the loading data appears to be quite consistent for stress increase with strain increments of 10%, the unloading traces are non-linear. Figure 2.2.4 shows that a substantial amount of load decrease occurs in the first 10% strain of unloading. The stress increments of DF A4700 and IM 800A become more linear soon after (approximately 20%), but the VHBs take up to 40% strain for this to be observed. Stress data becomes negative as the sample returns to its starting position as buckling occurs resulting from residual strains. Therefore, negative stresses that are recorded at positive strains aren't included in Figure 2.2.4. Positive data points are shown and labeled for the lowest applicable strain. As discussed above, IM 800A and VHB 5925 displayed decreasing residual strain with increase rate, and this is reflected in their unloading plots (Figure 2.2.4b and Figure 2.2.4d).

These plots can be used to phenomenologically propose a rate evolution law for the elastomers. Rate dependence in tough thermoplastics and elastomers have been shown to follow an Eyring dependence with yield being related to ease of molecular movement [73]. Typically, a bi-linear or exponential dependence is observed over several decades of strain rate. The experimental data presented in Figures 2.2.3 and 2.2.4 is consistent with previously reported trends. Note that the rate dependence observed here is independent of strain magnitude, up to 100% strain. The steep deformation recovery during unloading is indicative of significantly altered molecule chain entanglements (Figure 2.2.4).

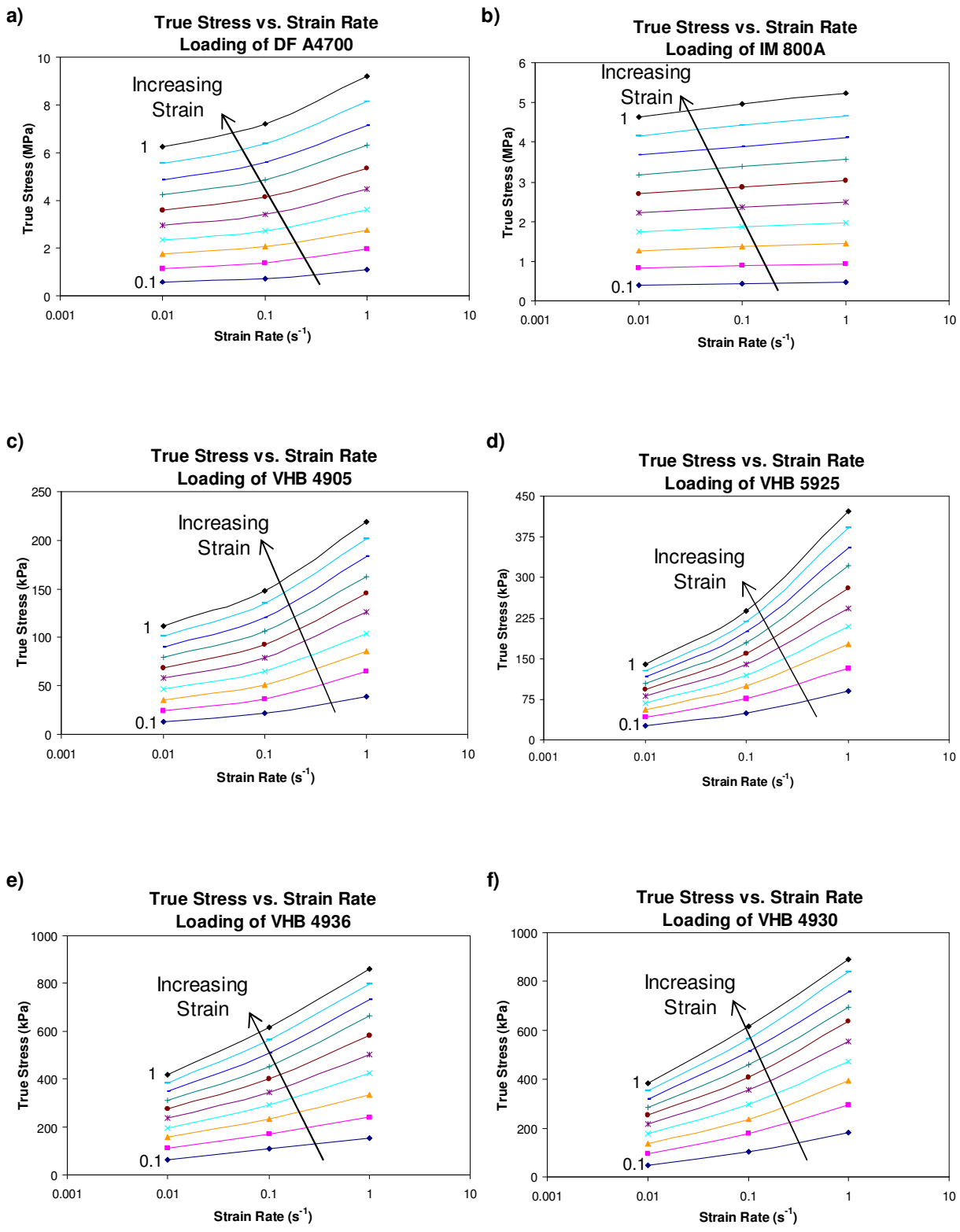

Figure 2.2.3 True stress as a function of strain rate measured at loading strain increments of 10% for: a) DF A4700, b) IM 800A, c) VHB 4905, d) VHB 5925, e) VHB 4936, and f) VHB 4930

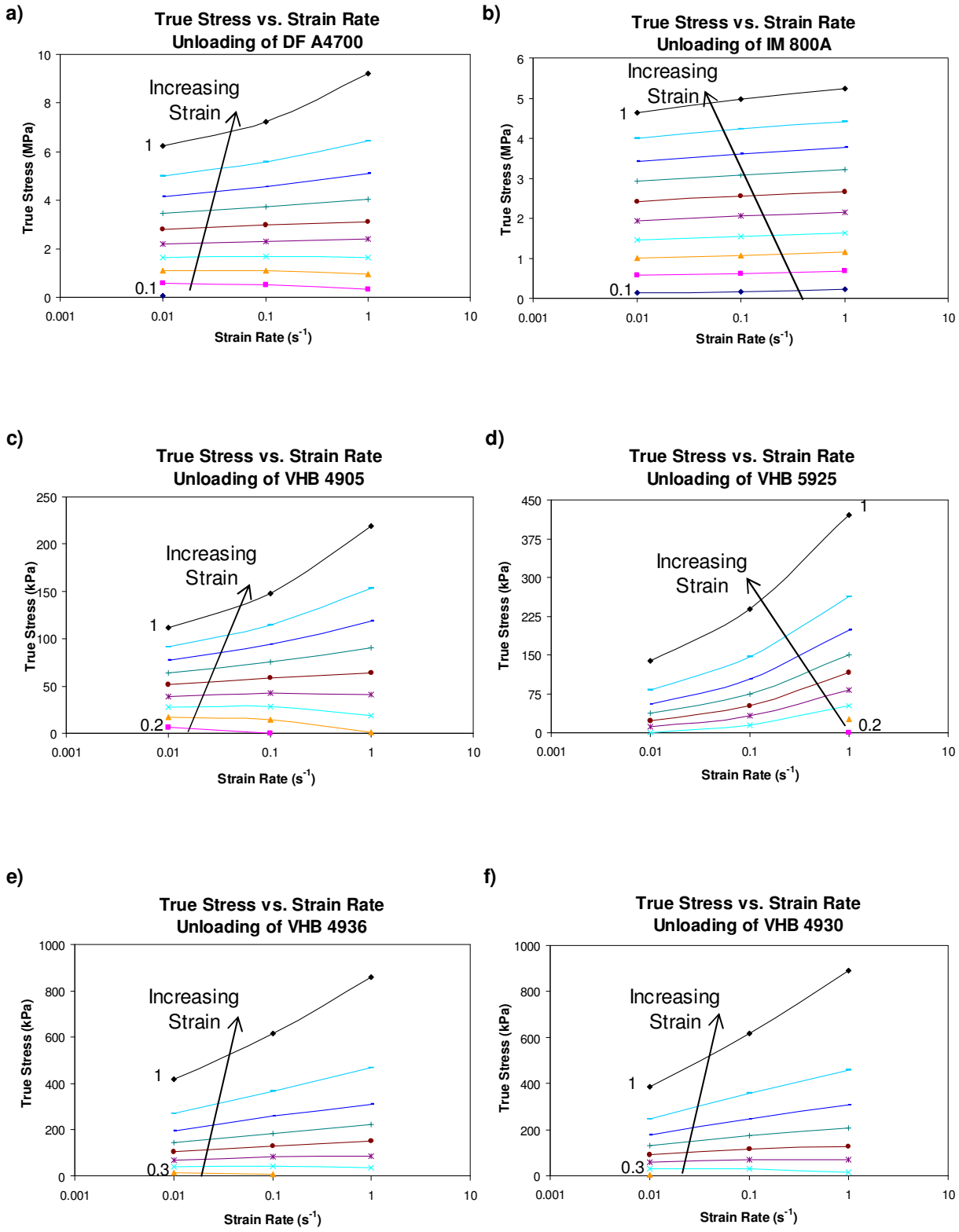

Figure 2.2.4 True stress as a function of strain rate measured at unloading strain change of 10% for: a) DF A4700, b) IM 800A, c) VHB 4905, d) VHB 5925, e) VHB 4936, and f) VHB 4930

2.2.1 Hysteresis Loop Areas

Hysteresis is observed for all interlayers indicating that less force is required to unload than load the materials. Although the mechanisms for hysteresis are not well understood, it is known that it is not a rate effect and is reflective of energy absorption. Loop areas under the stress/strain curves are considered the strain energy of the material or energy that the material dissipates during loading and unloading (Figure 2.2.5). A fully elastic material would have the same loading and unloading curve with no energy being dissipated or stored. Loop areas are calculated using a numerical integration Mathematica code (Appendix A.1) that sums areas of successive trapezoids that approximate the raw data. This method consistently over and underestimates magnitudes to the point where error is negligible and the algorithm is an acceptable approximation. The measured areas of these loops are normalized by the area of the quasi-static strain rate (0.01 s^{-1}) for each interlayer with results shown in Table 2.3. Since each material is normalized with respect to its own quasi-static area, all six interlayers may be compared in terms of relative increase of loop area.

It is important to observe how the interlayers' energy dissipation capabilities translate with increasing strain rate. Increase in loop size with strain rate is representative of the material's ability to scale energy dissipation/absorption mechanisms with rate. For example, while all of the other five interlayers have an increase in loop size of more than 2.5 times through two decades of strain rate, IM 800A only has an increase of 1.67 times. VHB 4905, the most compliant of all the interlayers, had the largest increase in hysteresis loop area (4.5 times). Relative loop increase for DF A4700 is multiplicatively equal between strain rates with differences of approximately 1.5 and 3.0 times for 0.1 s^{-1} and 1 s^{-1} respectively. VHB 5925 and VHB 4936 have very similar relative increases in loop areas, despite loop areas being quite different. The other solid acrylic sample (VHB 4930) showed the second largest relative increase in loop area behind VHB 4905 (both considered incompressible).

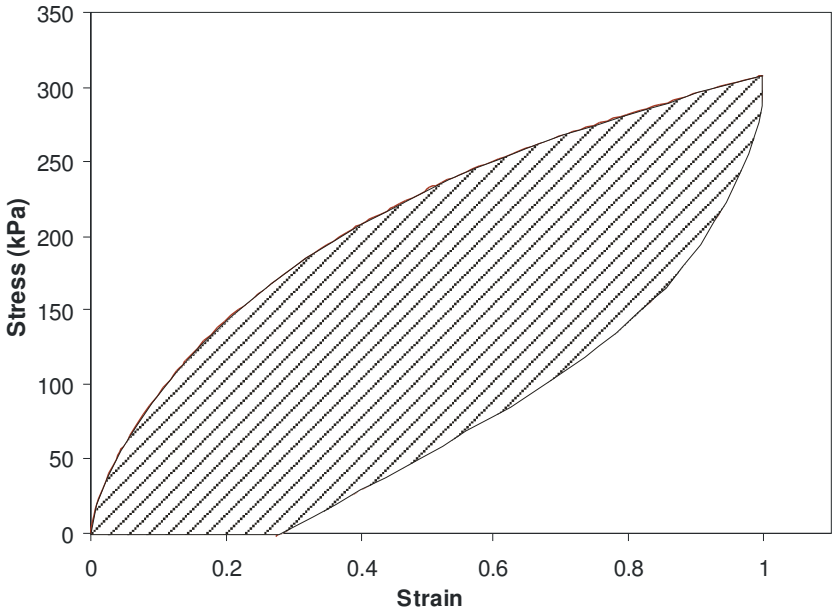

Figure 2.2.5 Hysteresis loop area shown shaded on representative trace

Table 2.3 Calculated and normalized hysteresis loop areas for interlayer tensile results

Interlayer		Strain Rate		
		0.01 s^{-1}	0.1 s^{-1}	1 s^{-1}
DF A4700	Area (MPa)	0.424	0.646	1.275
	$A/A_{quasi\text{-}static}$	1	1.52	3.01
IM 800A	Area (MPa)	0.169	0.201	0.282
	$A/A_{quasi\text{-}static}$	1	1.19	1.67
VHB 4905	Area (kPa)	9.928	18.794	44.91
	$A/A_{quasi\text{-}static}$	1	1.89	4.52
VHB 5925	Area (kPa)	34.473	55.196	93.91
	$A/A_{quasi\text{-}static}$	1	1.60	2.72
VHB 4936	Area (kPa)	84.696	141.24	221.69
	$A/A_{quasi\text{-}static}$	1	1.67	2.61
VHB 4930	Area (kPa)	77.326	144.1	254.2
	$A/A_{quasi\text{-}static}$	1	1.86	3.29

2.2.2 Cyclic TPU Tensile Testing

To further understand the response of the TPUs with regard to stress history, cyclic testing is completed using an Instron 5500R. Dogbone samples are loaded and unloaded at the three strain rates of 0.01, 0.1, and 0.5 /s. Specimens are elongated to a strain of 1.0 and then unloaded to the original position and allowed 30 seconds for some strain recovery. This loading/unloading sequence is repeated three more times to strains of 2.0, 3.0, and 4.0. Results for DF A4700 and IM 800A are shown in Figure 2.2.6, with traces being averages of five samples. As can be seen, both materials display cyclic softening showing that stress history has a strong correlation to mechanical response [74-77]. Dorfmann and Ogden modeled the cyclic response of carbon-black particle-reinforced rubbers. In their work, a sample was loaded/unloaded six times to a strain of 0.5, and then six times to a strain of 1 and finally six times to a strain of 1.5. Common observations between their results and the TPUs shown in Figure 2.2.6 include: degree of stress softening is dependent on previous maximum strain and a larger strain loading results in larger residual unloading strains [76]. For example, stress softening and residual strains observed in the traces of the TPUs are more significant for the cycle loaded to a maximum strain of 4.0 than a strain of 2.0.

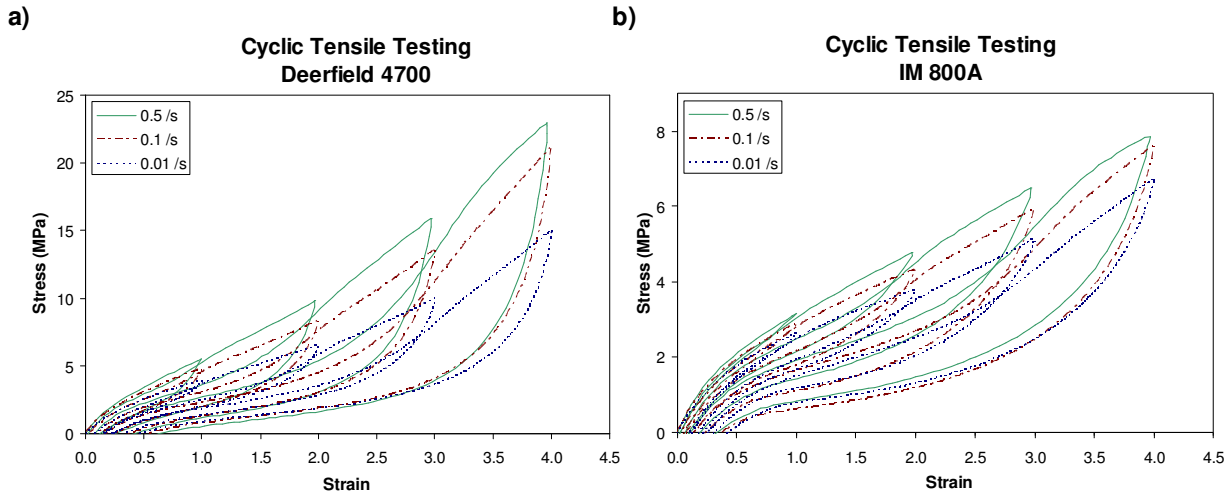

Figure 2.2.6 Cyclic tensile results at 0.01, 0.1 and 0.5 s^{-1} for a) DF A4700 and b) IM 800A

2.2.3 Mooney-Rivlin Model Fit

It is desirable to fit the tensile loading data of the interlayers with a phenomenological model for all three strain rates. The Neo-Hookean model, which assumes that stress is proportional to the first invariant of the strain, is the simplest finite deformation formulation for an elastic body. But for an elastomer/soft polymer, the Mooney-Rivlin model is a much better description of the stress/strain response. For the strain domains modeled (up to 100%), no strain hardening is observed; otherwise an Ogden model would be more appropriate. For the model, it is reasonable to assume that the material is isotropic as well as incompressible (constant volume). Therefore, with the assumption of uni-axial deformation in the 1-direction, a representative schematic shows contraction in the 2- and 3-directions (Figure 2.2.7a) of the sample. In this schematic, the primed and un-primed variables are initial and final lengths respectively, where λ_i is the stretch in the *i*-direction. The Mooney-Rivlin model parameters are derived from a strain energy minimization analysis and the force in the 1-direction on the end of an elastomeric sample is obtained by applying suitable boundary conditions [78-80] (Figure 2.2.7b). The two constants (C_1 and C_2) are calculated from experimental data using a Mathematica algorithm (Appendix A.2). As shown in Figure 2.2.8, the Mooney-Rivlin model fits the raw tensile loading data quite well. The data points are the experimental results while the solid lines are from the model fit derived from the equation shown in Figure 2.2.7b.

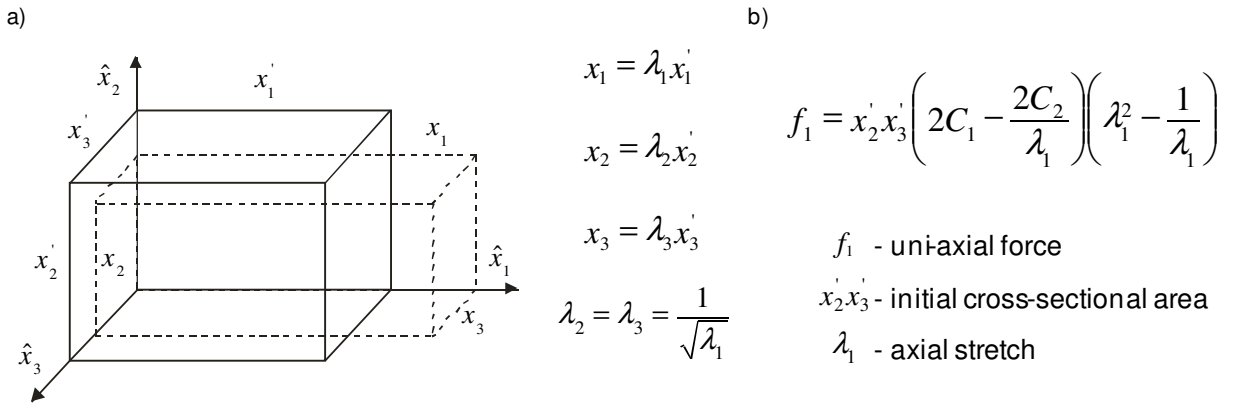

Figure 2.2.7 a) Schematic of a uni-axially deformed incompressible rubber and b) equation of force in the 1-direction

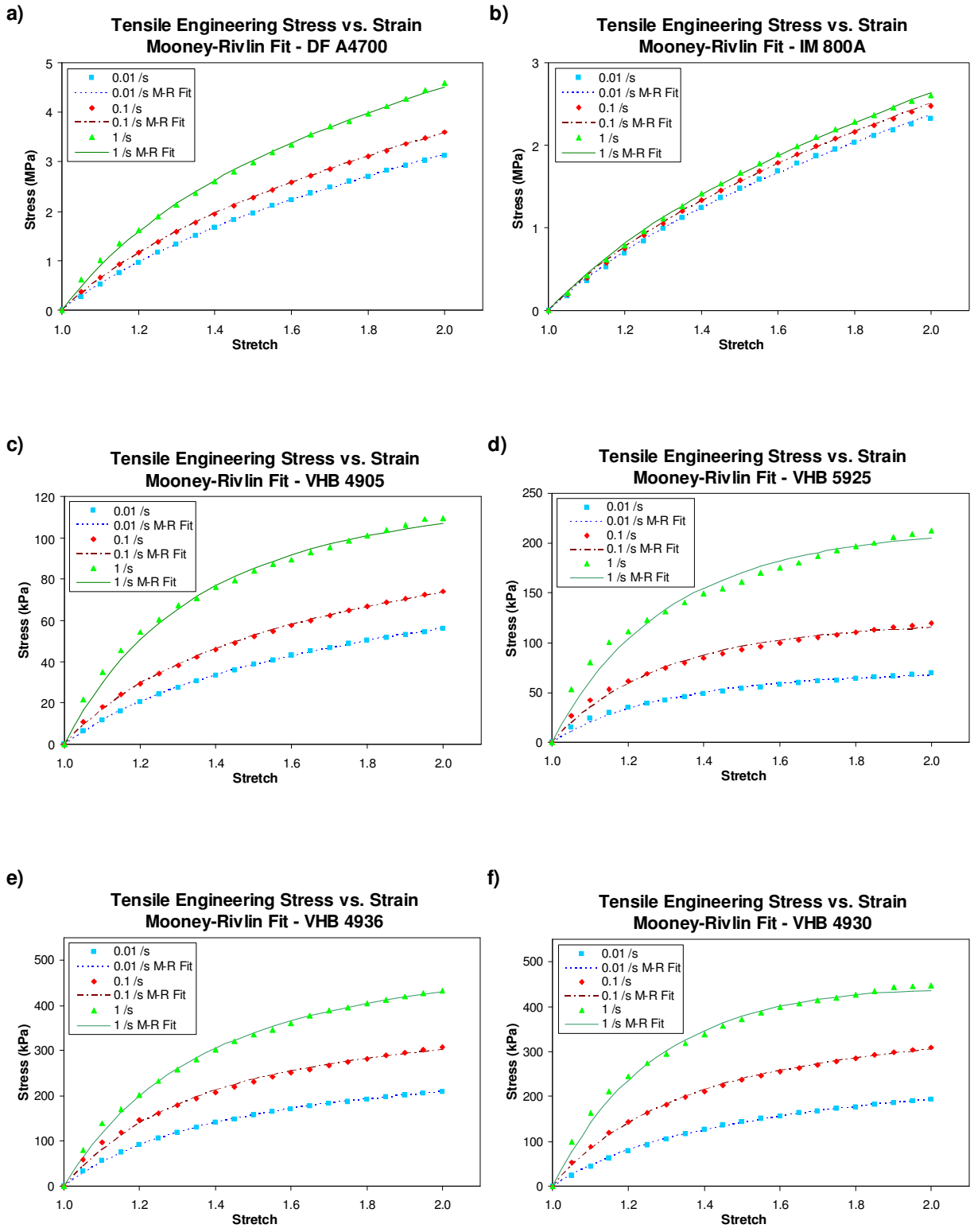

Figure 2.2.8 Three strain rate Mooney-Rivlin model fit results for a) DF A4700, b) IM 800A, c) VHB 4905, d) VHB 5925, e) VHB 4936 and f) VHB 4930

2.3 Interlayer Compression Testing

Compression of the interlayers is completed using an Instron 4204 frame with a 1 KN load cell for the VHB foams and a 5 KN load cell for the TPUs. Since the interlayers are very thin (less than 1 mm), it is necessary to stack 19.05 mm (0.75 in) diameter samples to approximately 3 mm in height to ensure an adequate amount of strain could be achieved. A circular punch was used to cut consistently circular specimens. While the VHB polyacrylates are adhesives, the TPUs (DFA4700 and IM800A) are not sticky until after heat treatment. Therefore, a fine layer of silicone grease is applied between each layer of the TPU stacks (as well as at the sample/platen interface) so that each layer compresses independently. The grease minimizes barreling at the center of the stack by reducing friction between the sample and platen, allowing all layers to expand equally in the radial direction during compression [81]. On the other hand, since the VHB foams are sticky, barreling of the stacks is inevitable and slippage between layers is impossible. The VHB stacks may be considered one solid material that compresses as a whole.

The materials are compressed at a strain rate of 0.001 s^{-1} (0.003 mm/s) until a TPU disk slipped or the tests were stopped due to possible machine damage with the VHB samples. Since the VHB stacks are so sticky and soft, they can compress to very high strains without compromising the stack structure. As shown in Figure 2.3.1, the VHB foams are much more compliant than either TPU and the DFA4700 is less compliant than IM800A at this strain rate. The plots shown are averages of three samples. It is observed that VHB 4936 and VHB 4930 have somewhat similar responses, which was also seen in the tensile results. Note that VHB 4936 strain hardens more significantly than VHB 4930 and that VHB 4905 is less compliant in compression than 5925, which is opposite of tensile results. This is due to the common compressible microstructure of VHB 4936 and VHB 5925. Initially, the collapsible air gaps are compressed (more compliant than incompressible samples), but eventually they can no longer be compressed and hardening occurs. This is more pronounced in VHB 4936 than VHB 5925 suggesting VHB 5925 has a larger amount of compressibility. While this compression testing is quasi-static and for loading only, Qi and Boyce and Yi et al. cyclically compressed TPU disks through four decades of strain rate (10^{-3}–1 s^{-1}) and found that the mechanical response displays strong rate

dependence and hysteresis [11, 13]. Note the interlayers' order of increasing compressive compliance is: DF A4700, IM 800A, VHB 4930, VHB 4936, VHB 4905, and VHB 5925.

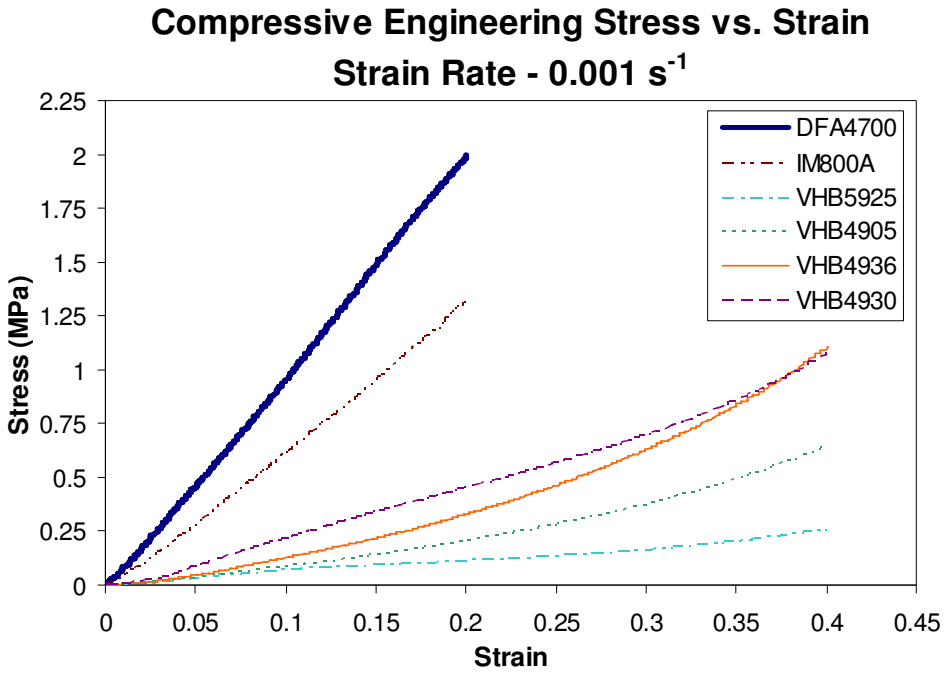

Figure 2.3.1 Compressive engineering stress as a function of strain for six interlayers

2.4 Shear Adhesion Testing

It has been established that the interlayers are rate dependent in tension, but it is desirable to understand how shear adhesion strength and response is affected by rate. Section 2.4.1 will discuss low rate lap shear joint testing, which is quite common, but few researchers have developed testing methods for dynamic shear adhesion testing at higher strain rates. The following setups are all based on split Hopkinson pressure bars (SHPB), with modified samples and/or geometries. Kihara et al. developed a unique impact experimental setup for testing shear strength of adhesives using a modified SHPB with a hexagonal incident bar containing several adhered surfaces [82]. While Kihara developed a novel technique, both Yokoyama and Shimizu, and Srivastava et al. developed a cylindrical specimen to be used with a compressive SHPB. Yokoyama and Shimizu utilized a pin and collar specimen where the adhesive layer is between a central cylinder (impact surface) and outer collar [83]. This geometry is ideal for optimizing

loading in pure shear using the SHPB, but may be difficult if the adhesive is a film (VHBs), requires pressure and heat (TPUs), has low viscosity, or if it is desirable to test at lower rates without a SHPB. Srivastava et al. developed a cylindrical lap joint that can examine adhesive shear strength for a wide range of strain rates [84-85]. As will be discussed in Section 2.4.2, this geometry is investigated for retrofitting the instrumented setup for impact shear adhesion testing.

2.4.1 Quasi-Static Shear Characterization

In order to characterize the adhesive strength of the adhesives, a quasi-static shear test is conducted. A lap joint with the dimensions of ASTM D1002, modified with added tabs to reduce eccentricities [86-87], is implemented to assess shear adhesion strength (Figure 2.4.1). In order to match the boundary conditions of the three-layered multi-laminates, the lap joint is composed of both PMMA and PC adherends. Lap joints are loaded at an assumed constant shear strain rate of 0.02 s^{-1} (0.0127 mm/s) using an Instron 4204 testing station (5 kN load cell) until complete delamination occurred or the bond strength was weakened to the point of showing a decreasing load. Note that this strain rate is derived from a constant crosshead speed and therefore assumes rigid adherends that do not deform [88].

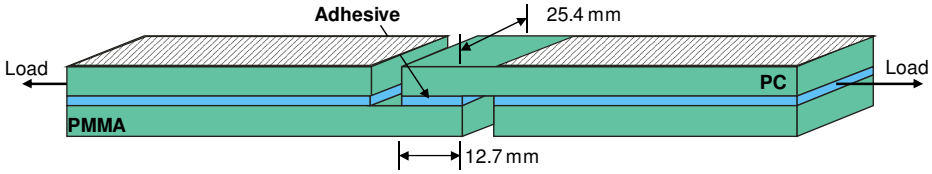

Figure 2.4.1 Modified lap joint for quasi-static shear adhesion testing (gripped area shaded)

When in the clamps, the added tabs are completely gripped (shaded region in Figure 2.4.1) with the only exposed area being the bond and adjacent gaps. This focuses the load directly into the bond and ensures it is as close to pure shear as possible. The traces shown in Figure 2.4.2 are averages of six samples for shear stress as a function of shear strain. While all responses are non-linear in nature, the TPUs appear to be slightly linear with the VHBs behavior appearing highly non-linear. Note that shear stress is inhomogeneous with stress concentrations at the edges of the bond, so stresses reported can be considered the average. As shown in Figure 2.4.2a, both TPUs have significantly higher adhesive strength than all of the VHBs (Figure

2.4.2b), with DF A4700 having stronger adhesion than IM 800A. Once again, VHB 4936 and VHB 4930 have very similar results, while VHB 4905 fails at a significantly lower shear strain than the other VHB adhesives due to local delaminations resulting in bond weakening.

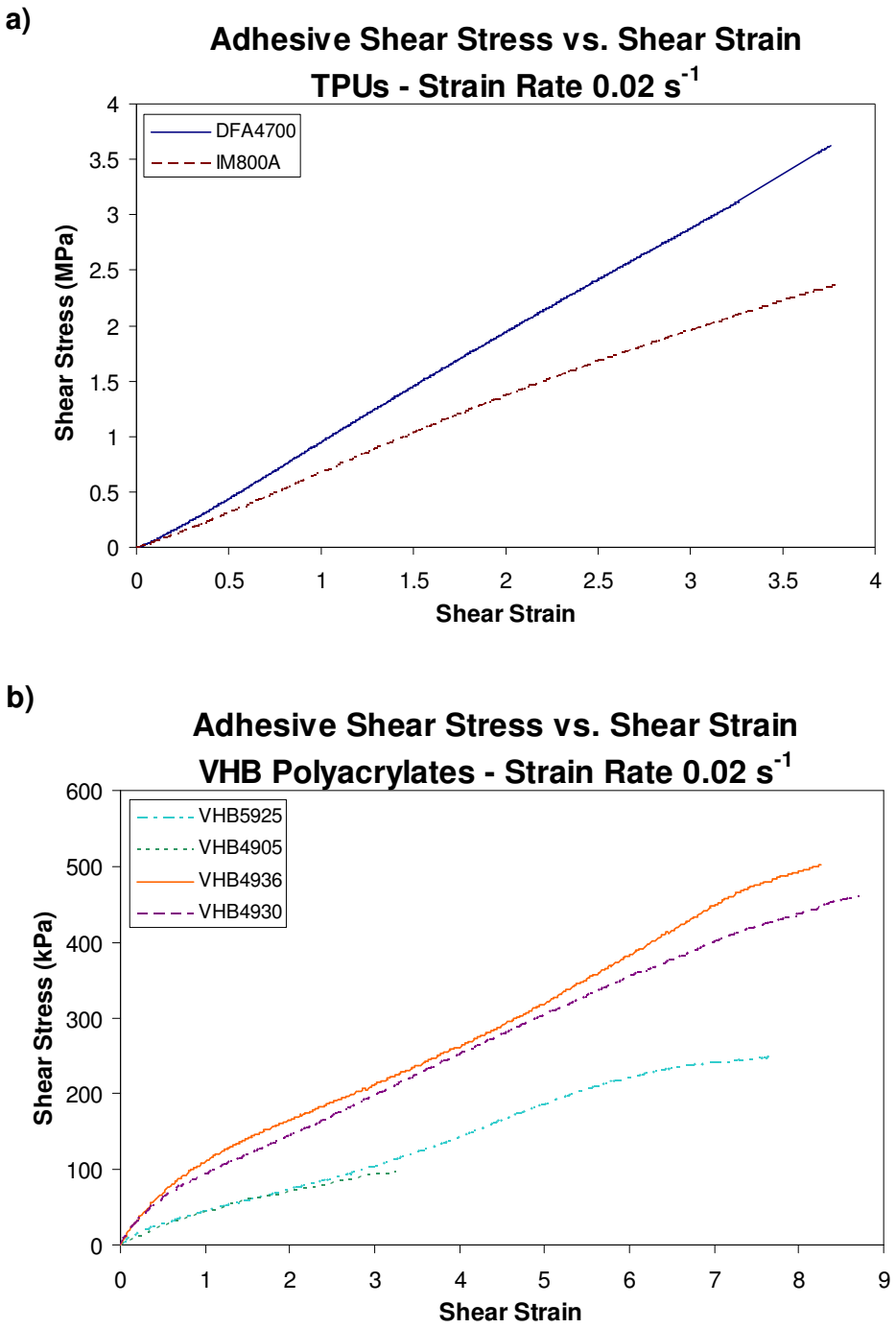

Figure 2.4.2 Engineering shear stress as a function of strain: a) TPUs and b) VHB polyacrylates

The results of the shear adhesion testing are outlined in Table 2.4. The strain at failure is the strain at which the bond was observed to have a maximum shear strength or completely delaminate. In the case of both TPUs, there was a complete and catastrophic delamination resulting in the fully intact adhesive remaining bonded to the PC adherend. The VHB polyacrylates (besides 4905) strained to very large shear strains before the maximum shear strength was reached. Following the tests, the VHB 5925, VHB 4936 and VHB 4930 adhesives completely recovered elastically with no visible delaminations. These quasi-static results can be compared to reported dynamic adhesion performance metrics from 3M Adhesives (Table 2.5). The 90º peel adhesion tests are conducted using a stainless steel adherend with displacement of 5 mm/s with the average force to remove the adhesive measured (ASTM D-3330). Normal tensile (T-block tensile) tests have aluminum adherends with 6.45 cm^2 (1 in^2) adhesive area and adherends are pulled apart at a rate of 0.83 mm/s with the peak force being reported (ASTM D-897). Dynamic shear tests were also carried out by 3M using overlap shear joints with stainless steel adherends and a displacement rate of 0.21 mm/s with the peak force being recorded (ASTM D-1002). According to Table 2.5, VHB 4930 has the best adhesion properties out of the VHB polyacrylates tested. When comparing 3M reported shear strengths with this research's results, the orders of adhesion strengths do not correlate. This is most likely due to the fact that different delamination modes were used to test the adhesives (opening, shearing, and tearing). In addition, 3M used steel adherends while the results in Table 2.4 are for polymer adherends (PMMA and PC). The adhesives have different adhesion strength to metals when compared to polymers. Note that although experimental and 3M reported shear strength trends don't match with reported 3M results, several of the samples' orders of magnitude are similar (VHB 4936/ 4930).

Table 2.4 Interlayer quasi-static shear adhesion result

Interlayer	Shear Strength (kPa)	Strain at Fail	Delamination
DFA4700	3565	3.75	Complete
IM800A	2373	3.77	Complete
VHB4905	90.95	3.29	Partial
VHB5925	245.5	7.7	None
VHB4936	510.2	8.26	None
VHB4930	441.2	8.7	None

Table 2.5 Reported VHB dynamic adhesion performance from 3M

Interlayer	90º Peel Adhesion (N/m)	Normal Tensile (kPa)	Dynamic Overlap Shear (kPa)
VHB4905	2100	690	480
VHB5925	3000	620	620
VHB4936	3000	620	550
VHB4930	3500	1100	690

2.4.2 Dynamic Shear Characterization

Although this quasi-static compression and tensile data is helpful for material characterization and modeling purposes, it is desirable to obtain data for a wider strain rate range since the material response is non-linear and evolves with rate. Chalkley and Chiu's results showed strain rate dependence of shear adhesive strength for a Cyanamid adhesive through a range of low strain rates from 10^{-4}–10^{-1} s^{-1} [88]. Shear adhesion tests conducted dynamically at impact speeds [82-85] varied loading rates and not strain rates, and found that shear strength increases substantially with rate. Characterization of the higher rate response of adhesion strength is especially important for a rate dependent interlayer in a multi-laminate subjected to impacts at various speeds. In an effort to examine shear response at higher rates, a steel bracket and specimen geometry are developed to retrofit the current experimental setup. As shown in Figure 2.4.3a, the specimen geometry is a cylindrical lap joint based on the sample configuration of Srivastava et al. but with different dimensions [85]. Similarly to the quasi-static lap joint testing, adherends are PMMA and PC to match the boundary conditions of the multi-laminates. As discussed in the Srivastava publications, this specimen is beneficial as it may be tested at a wide range of strain rates, including a SHPB (Figure 2.4.3b). In an attempt to retrofit the current experimental setup (Chapter 4), a steel holder is developed to fit directly into the bracket designed for six inch square multi-laminates (Appendix B.1). The gas gun barrel slides directly into a steel tube with the sample sitting flush against the end. A flat-headed impactor is propelled by the compressed air and impacts the lap joint, recording contact force and monitoring adhesion strength during impact.

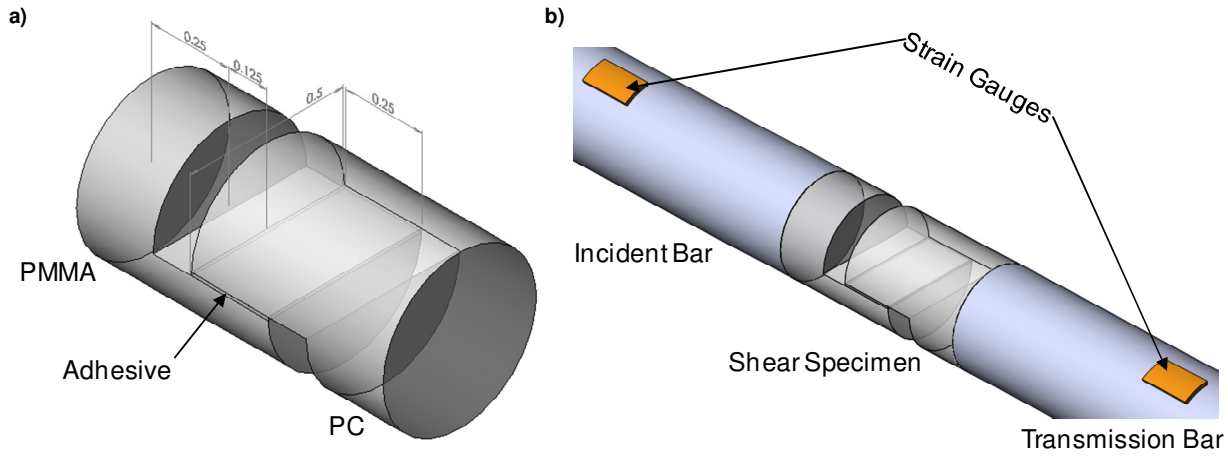

Figure 2.4.3 High rate shear adhesion testing a) specimen geometry and b) implemented in a split Hopkinson pressure bar

In order to ensure that the bond is loaded purely in shear, alignment of the samples is very important and assembly is not easy. The cylindrical sample has to slide into the barrel with minimal friction, which requires near-perfect alignment. As discussed in further detail in Chapter 3, the TPUs require heat and pressure to become an adhesive. Therefore, an aluminum bracket is fabricated in order to press the cylindrical lap joints in the hot press to bond the adherends (Figure 2.4.4a). High temperature Kapton tape is used to keep the components in place during pressing. Great care is taken to properly assemble these samples using tape and bracket rods to prevent rolling. Assembled samples made with polymer and steel adherends are shown in Figure 2.4.4b. At this point in the research, data has not yet been obtained since more attention has been on normal impacts. Many issues exist for this proposed new setup, such as: specimen alignment, damage of the adherends during impact, and inconsistent force readings resulting in difficulties measuring adhesion strength. Since too many complications arise with the developed retrofitted bracket, a SHPB of similar diameter to the cylindrical shear specimens will be used to conduct dynamic shear adhesion testing on the adhesives characterized in this chapter. While the current chapter focuses on uni-axial testing in various modes (tension, compression, and shear), in actuality the interlayer and outerlayers undergo multi-axial states of stress and inhomogeneous stress distributions during impact [67].

a) b)

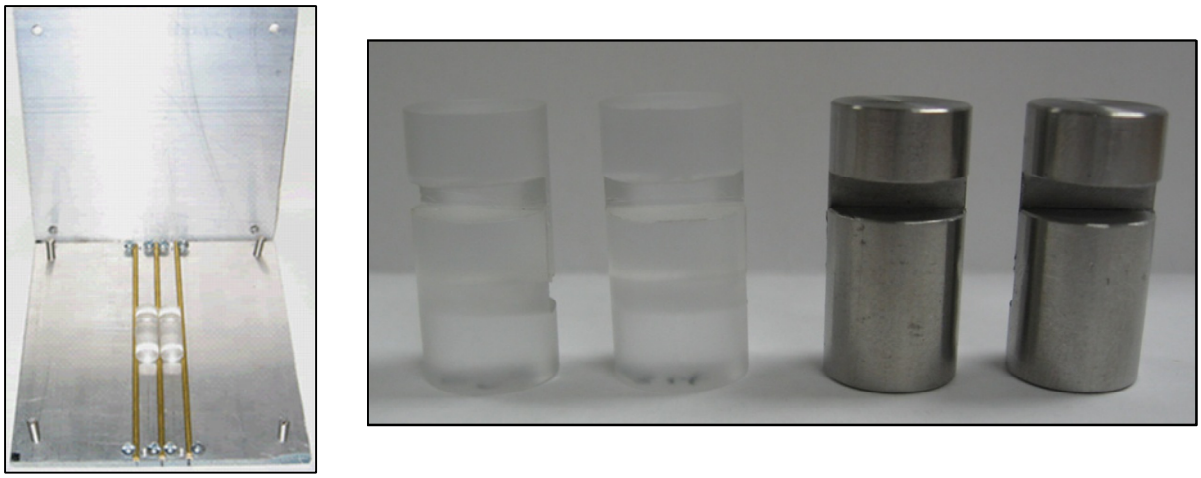

Figure 2.4.4 a) Bracket for assembly of cylindrical lap joints and b) polymer and steel samples

Chapter 3

Multi-Laminate Preparation and Assembly

This chapter discusses the procedure for preparing samples for impact testing. This includes unbonded samples as well as bonded multi-laminates. It will also outline methods and the thermal/pressure profile developed for assembly of TPU multi-laminates when assembled on site using a miniature autoclave, hot press, and temperature controller.

3.1 Unbonded Multi-Laminates

For unbonded samples, 1.5875 mm (1/16 in) PC and PMMA obtained from McMaster are cut into 15.24 cm (6 in) square pieces using a band saw. The edges are de-burred and surfaces are cleaned using isopropyl alcohol (IPA). At this point, the unbonded two-layered samples can be assembled by stacking a PMMA layer on top of a PC layer. For the unbonded three-layer samples with a thermoplastic polyurethane (TPU) interlayer, a wooden and metal rubber cutting die is used to cut 15.25 cm (6 in) square pieces of DF A4700 and IM 800A. The TPU surfaces are then cleaned with IPA and allowed to dry. Following drying, the three-layered samples are stacked with a PMMA front, TPU middle, and PC back layer.

3.2 Bonded Multi-Laminates

3.2.1 Thermoplastic Polyurethane Adhesives

The TPUs tested are not tacky and are semi-transparent as-received, so heat and pressure are required to convert them optically clear adhesives. Goulbourne and MacAloney showed that the TPUs can also become transparent by submersion in water [72]. For assembly, an autoclave is required to accurately control both heat and pressure profiles. In order to avoid flow of component materials and create consistent bonds, the materials must be heated slowly at a rate of

2 ºF/min to 160 ºF. Once this temperature is reached, pressure is increased to 50 psi at a rate of 10 psi/min. Temperature is then increased to a saturation temperature of approximately 200 ºF and temperature is maintained for several minutes to allow for a thermal soak. Samples are cooled down in a controlled manner at 5 ºF/min until ambient temperature is reached. Without an autoclave available, a Pneumapress Tetrahedron P-400 hot press with a Blue Micristar digital controller and miniature "autoclave" in the Virginia Tech FAB lab is used instead (Figure 3.2.1). It is composed of two steel halves separated by a rubber gasket. One half is supplied with positive pressure to press the component material layers together, while the other half is supplied with a vacuum to suck out air bubbles between layers. The hot press is used to compress the gasket to maintain both positive and negative pressures in the steel halves, as well as heat up the whole system.

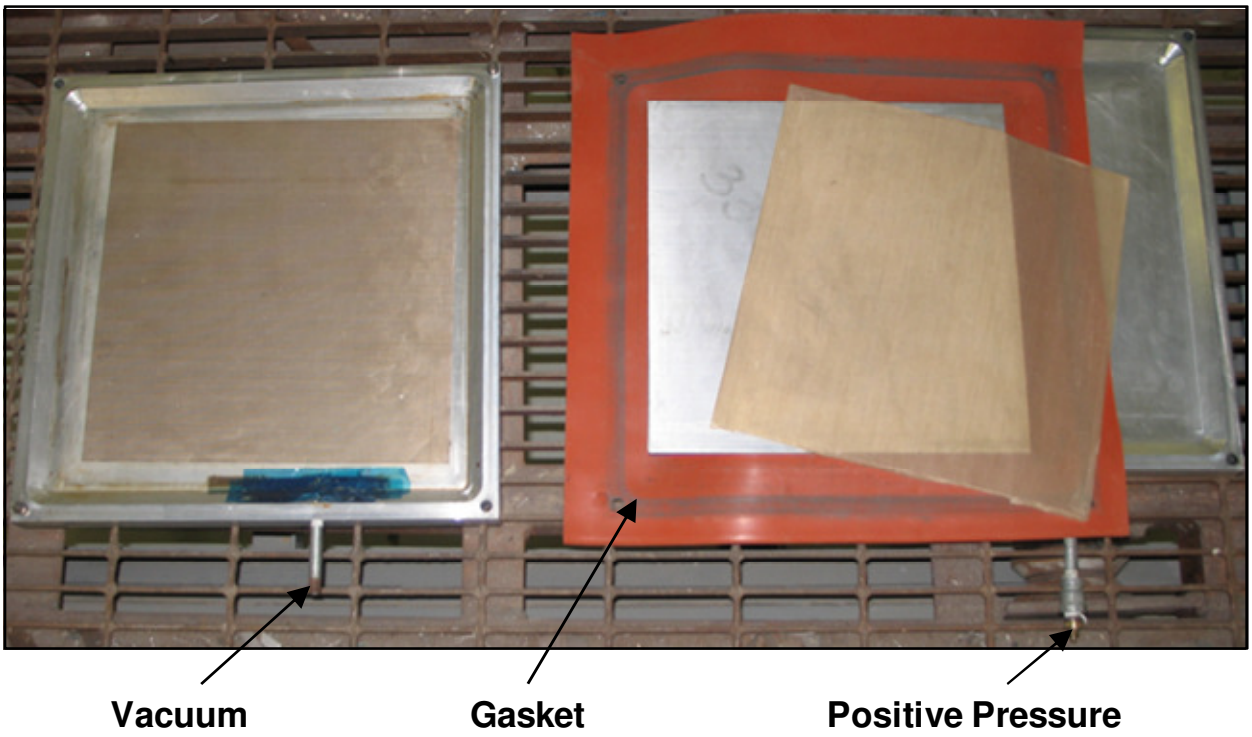

Figure 3.2.1 Miniature "autoclave" used with hot press for assembly of bonded TPU samples

As shown in Figure 3.2.2, thermocouples are used in between sample layers, as well as on the hot press, to verify both the internal temperature of the bondline and the reported hot press temperature. There is a clear discrepancy between the temperature of the hot press and that of the bondline, so many iterations were needed to develop an appropriate thermal profile. Note that bondline temperature at the center of the 60.96 cm (24 in) square TPU multi-laminates is very similar to the temperature measured at the edge. This is indicative of a uniform heating condition in the sample.

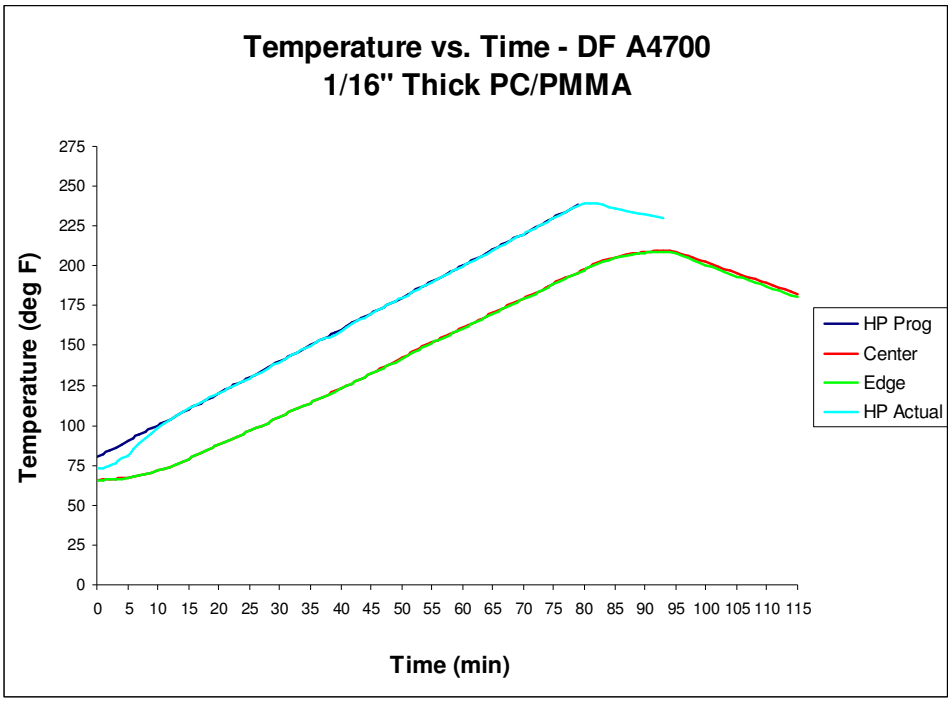

Figure 3.2.2 Comparison of hot press (HP) programmed and actual temperature and center and edge of bondline of multi-laminate

The thermal/pressure profile developed is shown in Figure 3.2.3a. After 45 minutes, the pressure in the "autoclave" is increased to 50 psi, at 10 psi/min, while the hot press temperature steadily increases at 2 deg F/min. Once the bondline has reached at least 200 deg F, temperature is held relatively constant for a final thermal soak of approximately 15 minutes. An example of a resulting sample is shown in Figure 3.2.3b. While mostly transparent, there are many inconsistencies and air bubbles throughout the bondline. Therefore, bonded TPU multi-laminate assembly is outsourced to an autoclave so consistent samples may be used for impact testing.

a)

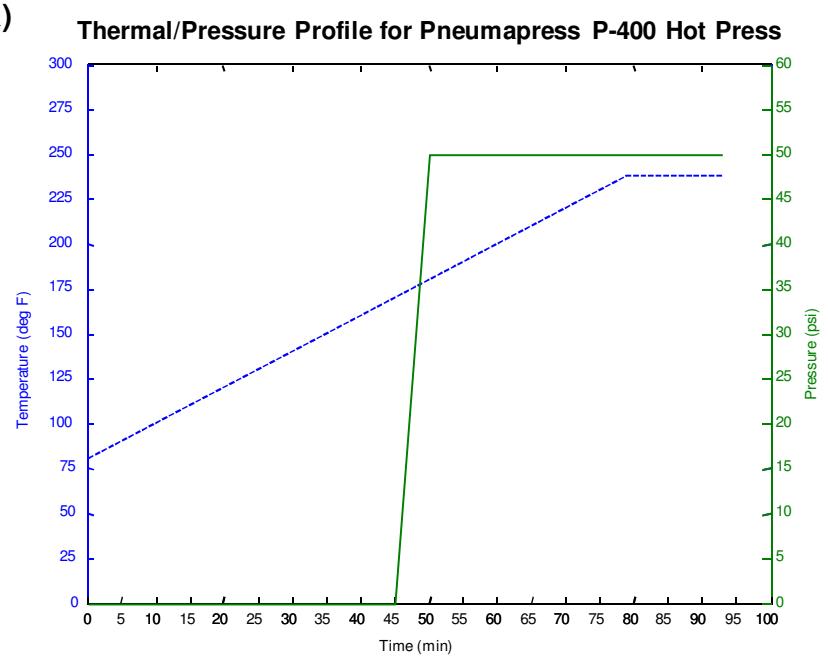

b)

Figure 3.2.3 a) Thermal/pressure profile for hot press and miniature "autoclave" and b) representative bonded multi-laminate assembled on site

3.2.2 VHB Polyacrylate Adhesives

While the two TPUs (DF A4700 and IM 800A) require a thermal and pressure treatment for assembly of multi-laminates, the four VHB adhesives are tacky as-received. Therefore, only pressure is required for assembly. PMMA and PC outerlayers and VHB interlayers are cut to 15.24 cm (6 in) squares and outerlayer surfaces are cleaned with IPA. The VHB adhesive is carefully applied to the PC layer first. Great care is taken to smooth out air bubbles and gaps in the interlayer, but the very low compliance and tacky surfaces of the interlayer makes this quite difficult. Then the PMMA layer is gently applied. It is important to begin smoothing at the impact site and work out towards the edges to ensure that the center of the panel is free of imperfections. Once an initial bond is complete, the whole panel is pressed by hand to eliminate as many air bubbles as possible. These gaps are inevitable, but are considered to be evenly distributed. Note that air gaps are not in the TPU samples, but were observed in varying degrees for all four VHB bonded multi-laminates. It is important that the assembly method is repeatable and consistent for every sample so that it isn't a variable for impact testing.

Chapter 4

Instrumented Gas Gun Experimental Setup

This chapter discusses the low velocity impact experimental setup including: specifications, components, sensors, and LabVIEW VI data acquisition and coordination methods. The intermediate velocity gas gun experimental setup (Figure 4.1) is unique in that it is instrumented, recording contact force and out-of-plane deflection. Typically, high speed gas guns are unable to measure contact forces or sample deflection and rely on analysis through measuring V_{50}, incident/residual velocities, and post-impact visual inspection [6-8, 28, 32, 38-39, 60-63].

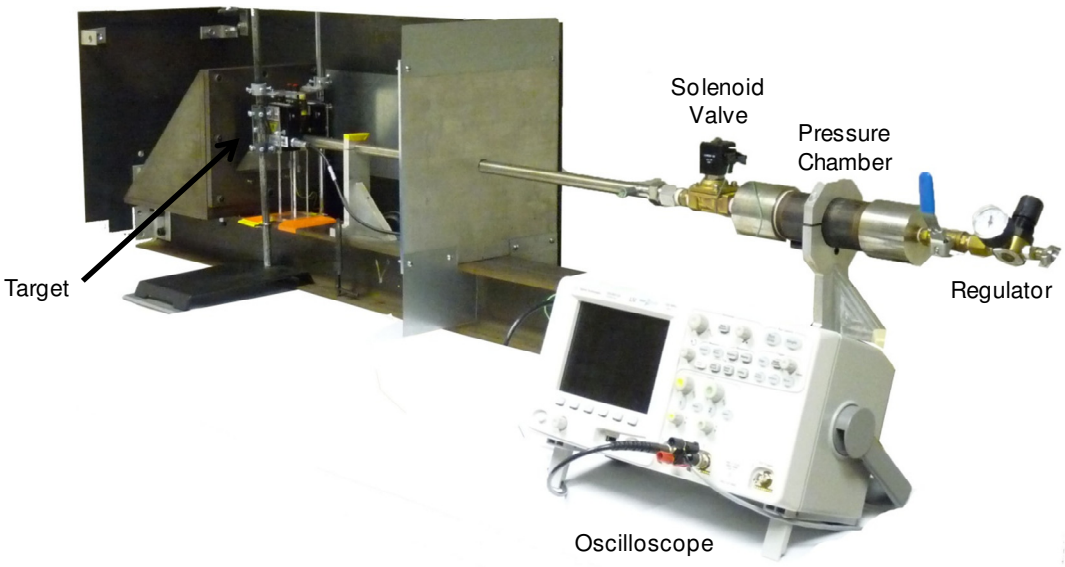

Figure 4.1 Picture of low velocity experimental setup

4.1 Specifications, Components and Sensors

4.1.1 Setup Overview

A custom instrumented test facility was built for impact testing at low to intermediate impact velocities (9–30 m/s) using a lightweight, hemi-spherical, steel impactor (28.5 grams) with a

diameter of 1 cm (0.4") (Figure 4.1.1a). The impact specimens are clamped in place by a steel bracket exposing 161.29 cm^2 (12.7 cm/5 in sides) of the original 232.25 cm^2 (15.24 cm/6 in sides) square panel. The mass ratio between the impactor and the samples (~95 grams) is 3.3. Two ratios inherent of the impactor and experimental setup are the ratios of the diameter of the impactor to the width and thickness of the multi-laminate. The diameter of the impactor (1 cm) to the span of the sample (12.7 cm) is approximately 0.08. The impactor diameter (1 cm) to specimen thickness ratio ranges from 2.62–3.15. The thinnest samples consist solely of unbonded PMMA and PC (3.175 mm), while the 3.81 mm samples represent the three-layered composites (besides VHB 4905–3.675 mm). These ratios are important because they affect the energy absorption mechanisms observed, as well as impact mechanics and performance. Using an air compressor and regulator, air pressure is monitored to control the velocity of the instrumented impactor. The velocity capabilities of the setup are governed by the dimensions of the barrel (1 meter long and 12.7 mm inner diameter). After impact, pressure is relieved by air release holes near the end of the barrel. This allows the impactor to slide back into the barrel and prevent double impacts. If the impactor perforates the sample, a steel protective shield and catcher will trap the projectile. Perforation is outside the limits of the current investigation, but it is necessary for safety precautions.

The impactor consists of a quartz-shear shock accelerometer screwed into a steel impactor (Figure 4.1.1a). A major issue with impactor instrumentation is the trail wire of the sensor as it travels down the barrel during impact, so wireless solutions were investigated. Ultimately, there were no viable options for sensors that could wirelessly transmit the contact force data required. This is due to the robustness that would be necessary for the shock of an impact event, as well as electronic interference from surrounding metals, sensors, and devices. Therefore, a method had to be developed to consistently load the wired impactor to the same location while ensuring minimal friction and interference between the wire and barrel. As shown in Figure 4.1.1b, a HPDE cap is utilized to minimize tension on the wire/accelerometer connection and create a flat contact surface for the pressurized air to propel the impactor. Figure 4.1.1c shows the impactor in the HDPE sheath with only the hemi-spherical tip showing. The trail wire is loaded via a screw with a through-hole to keep the barrel sealed but allow wire entry (Figure 4.1.2). A loading rod pushes the impactor 50.8 cm (20 in) from the tip of the barrel. The trail wire is then

twice looped into the back end of the barrel and the pressure vessel is reattached. Now the slack required to travel to the impact site is available for the impactor. Consistently achieving a desired speed for a given pressure is dependent on the consistency of accelerometer trail wire loading and valve actuation, and has approximately ±5% variability. This was calibrated and practiced for numerous iterations before impact testing began to verify consistency and the pressure required for an impact velocity.

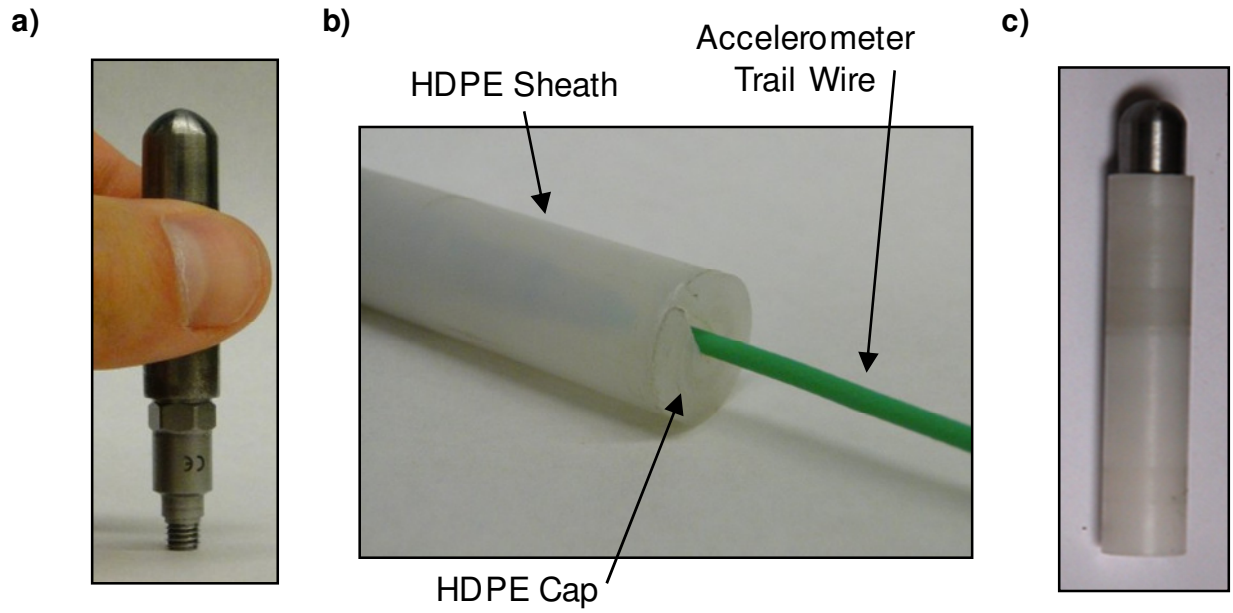

Figure 4.1.1 Pictures of a) steel impactor with shock accelerometer, b) trail wire, HDPE sheath and cap, and c) impactor in HDPE sheath

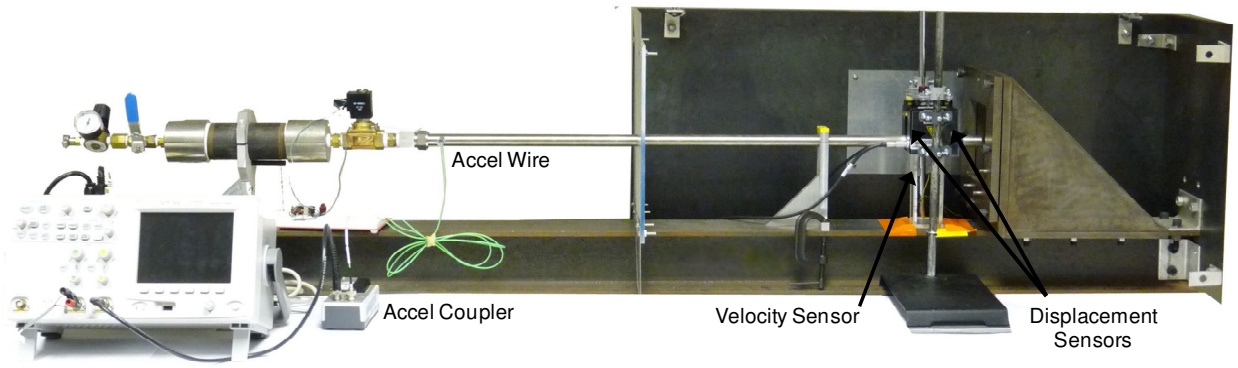

Figure 4.1.2 Picture of intermediate velocity experimental setup

4.1.2 Sensors

A Kistler K-Shear® shock accelerometer (model # 8742A50) is screwed into the back of the impactor to measure contact force (Figure 4.1.3a). An internal seismic mass (ring) is used to preload four quartz crystals and calibrate the sensor with an acceleration conversion factor of 0.102 mV/g (Figure 4.1.3b). A HDPE sheath and cap protects the sensor and cable connection during impact and minimizes friction with the inside of the barrel (Figure 4.1.1b). A Kistler wire (Figure 4.1.3c) with positive 10-32 and positive BNC connections (model # 1631C3) connects the accelerometer to the Kistler Piezotron® coupler (Figure 4.1.3d), which converts a charge per area output from the accelerometer to an AC coupled voltage readable by the digital storage oscilloscope (DSO). The DSO is an Agilent DSO5012A (Figure 4.1.4a), which records data at 2 GSamples/s and can store 8 million data points. To record out-of-plane deflection, two MTI Instruments MicroTRAK II® laser displacement sensors (head model # LTC-50-20) are implemented (Figure 4.1.4b). Data is sampled at 40 kHz and the sensors are capable of reading a range of displacements from positive to negative 10 mm (total range of 20 mm). Since the PMMA front outerlayer is transparent, small pieces of Aluminum reflective tape are required for the sensors to record displacement. Custom brackets (Figure 4.1.4b), secured onto chemistry stands, hold the laser sensors at the correct height and distance in line with the impact site (28.575 mm/1.125" off-center).

A velocity sensor, using two laser sources, photoresistors, and non-inverting operational amplifiers (op-amp) is implemented near the end of the barrel. The lasers shine through the pressure release holes, incident on the photoresistors. These lasers and photoresistors, used to be secured directly to the barrel, but too many inconsistencies and false readings were observed in the signal. This was due to pressurized air coming out of the pressure release holes and barrel vibration during impact. Therefore, holders are fabricated using PC to stabilize photoresistors (Figure 4.1.5a) and lasers (Figure 4.1.5b) to maintain consistent alignment. As the impactor passes through the lasers, incident light intensity decreases. This results in a photoresistor resistance ($R_{photoresistor}$) increase. Each photoresistor has an independent op-amp which outputs a voltage change corresponding to this resistance change. The circuit diagram for the op-amp and

calculation of output voltage (V_{out}) can be seen in Figure 4.1.6. Details on how the velocity sensor's data is processed to yield a velocity will be discussed in Section 4.2.

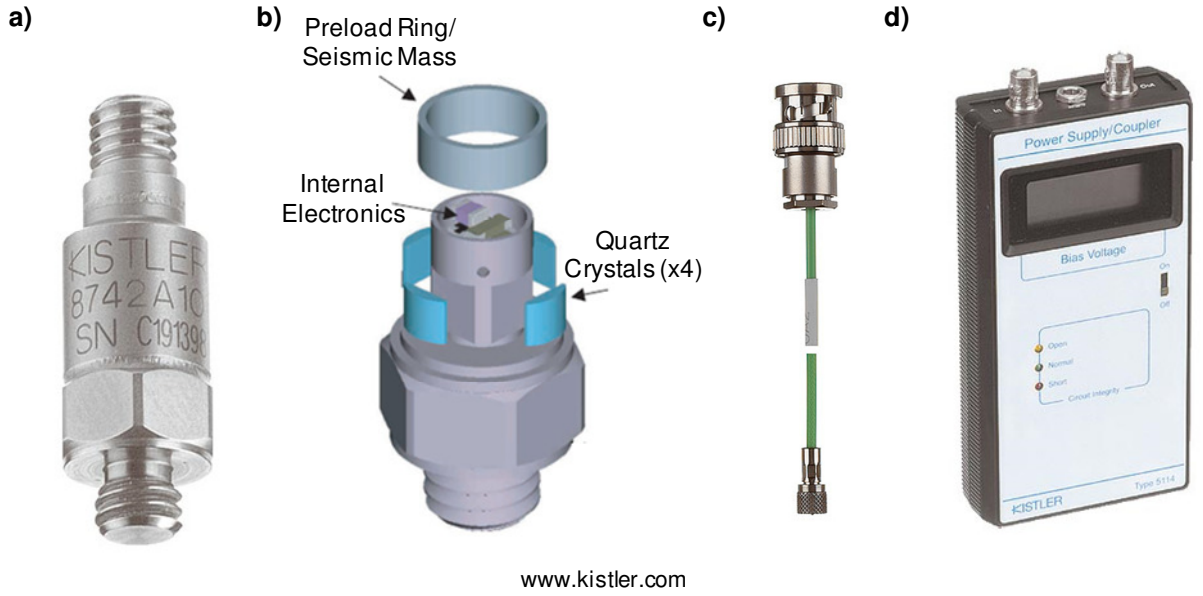

Figure 4.1.3 Kistler accelerometer a) picture, b) internal schematic, c) cable, and d) coupler

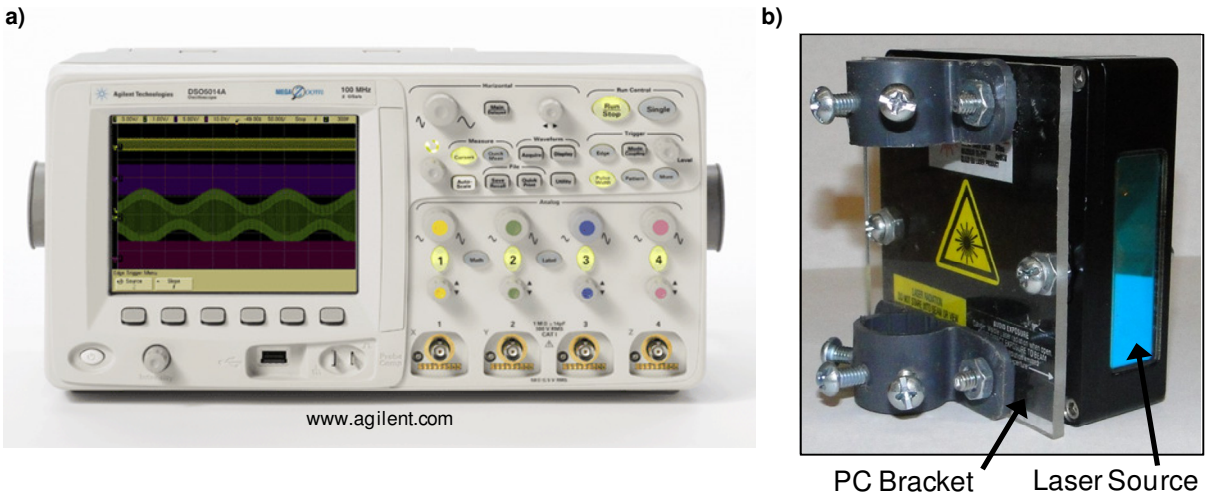

Figure 4.1.4 a) Agilent digital storage oscilloscope and b) MTI sensor and bracket

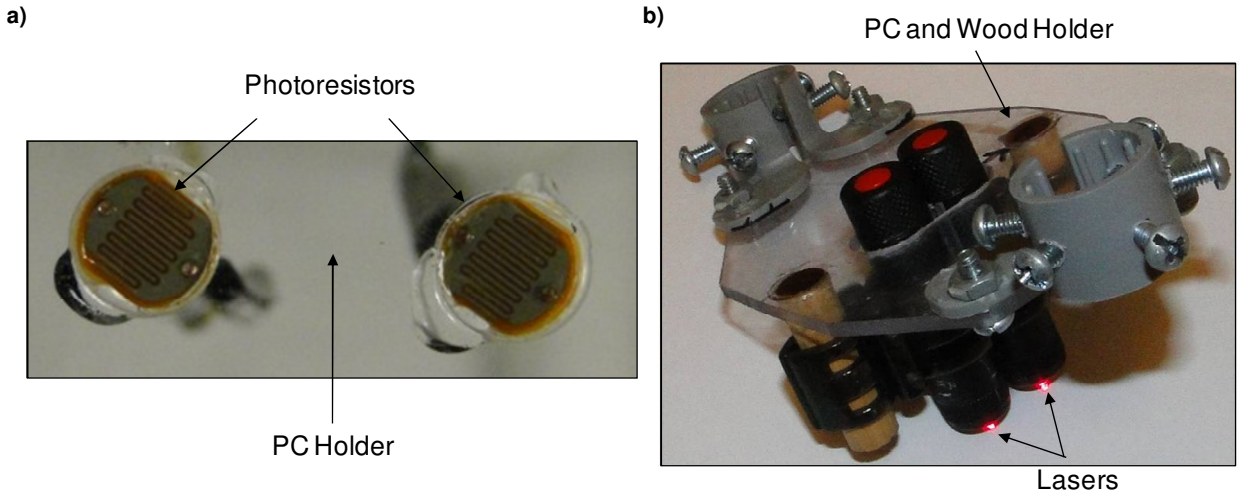

Figure 4.1.5 PC holders fabricated for a) photoresistors and b) lasers

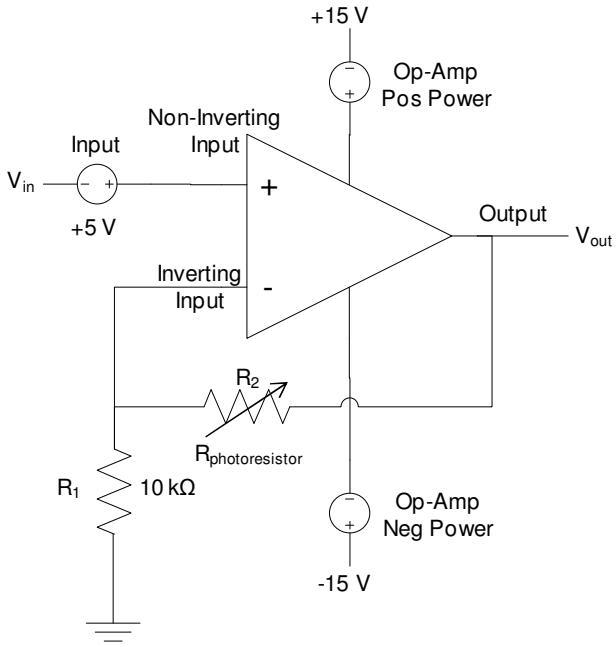

$$V_{out} = \frac{R_2 + R_1}{R_1} V_{in} = \frac{R_{photoresistor} + 10k\Omega}{10k\Omega} 5V$$

Figure 4.1.6 Non-inverting op-amp circuit diagram and resulting voltage gain calculation

4.2 Experimental Setup Operation

With three different sensors involved with the experimental setup (shock accelerometer, laser displacement, and impact velocity), synchronization of data acquisition is crucial. Figure 4.2.1 shows a representative schematic illustrating how a National Instruments LabVIEW Virtual Instrument (VI) is designed for data acquisition and operation of the instrumented gas gun. A National Instruments data acquisition (DAQ) module (USB-6211) is used to read inputs and send outputs. When initiated, the VI triggers both the solenoid pressure release valve and the DSO with a digital high (positive TTL signal) of 5 volts. This is considered the "reference zero time" for all of the sensors. When the valve is open, the impactor is propelled down the barrel until contact with the multi-laminate specimen occurs. Prior to contact, the velocity sensors' lasers are successively blocked by the impactor causing a voltage spike in the op-amp circuit (as described in section 4.1.2). While impact occurs, the accelerometer outputs impact site contact force to the DSO and displacement sensors measure off-center deflection. After completion of the test, an algorithm in the VI calculates impact velocity, and a time column for displacement data and a header are created for the saved file. An experimental procedural flow chart is shown in Figure 4.2.2, with more details regarding the LabVIEW VI code in section 4.2.1.

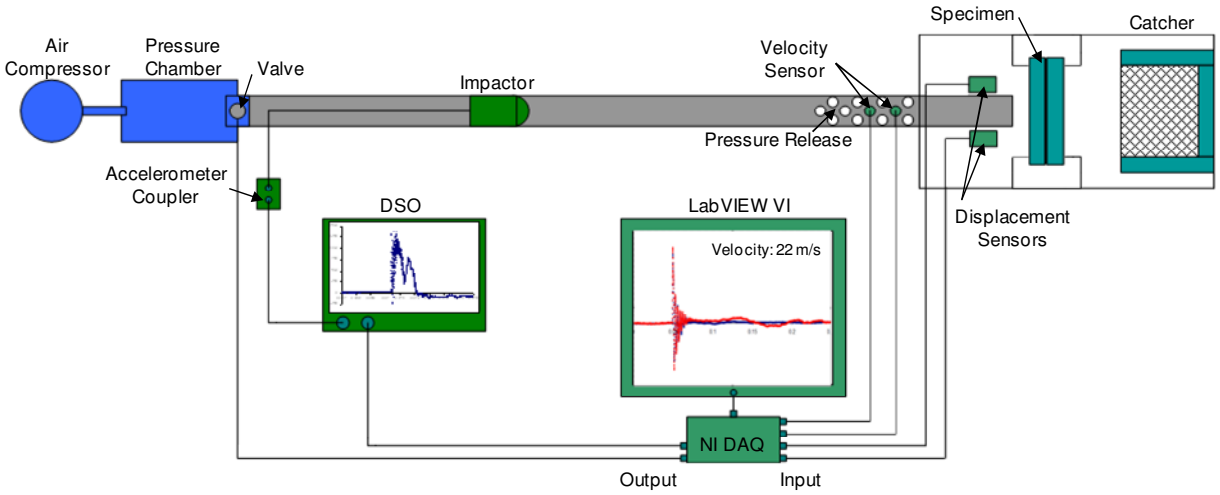

Figure 4.2.1 Experimental setup representative schematic of component

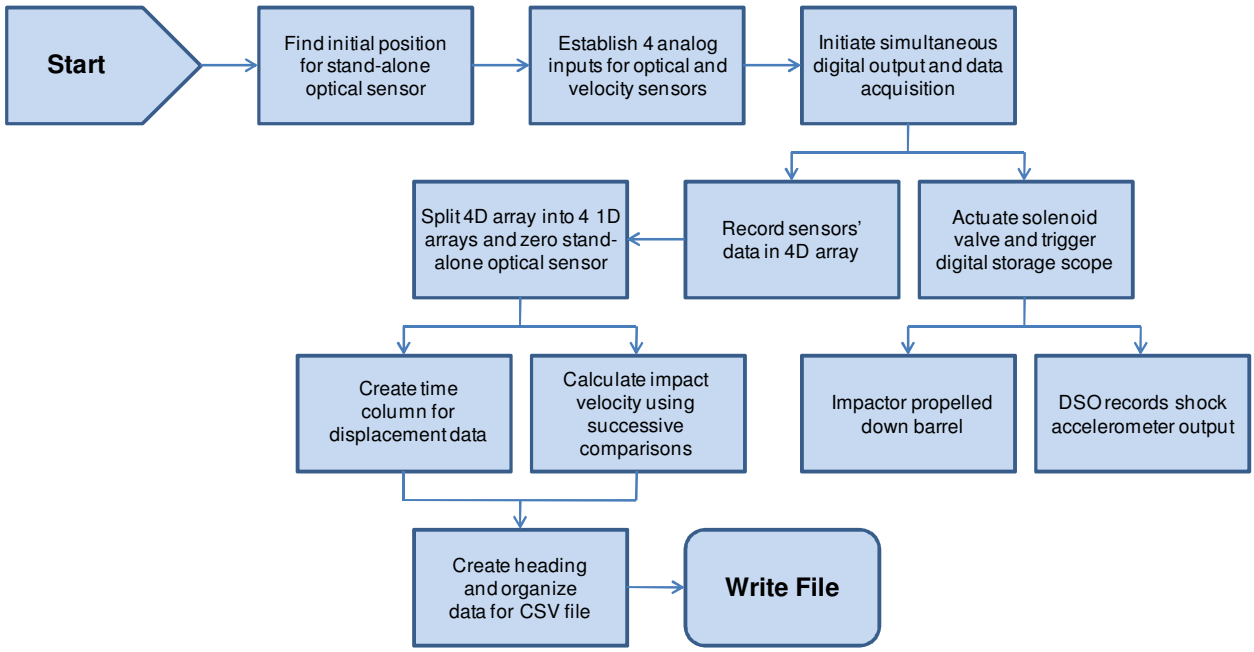

Figure 4.2.2 Flow chart describing the sequence of events for impact testing

4.2.1 LabVIEW Virtual Instrument (VI)

The LabVIEW VI is developed using a sequential case structure from left to right (thick gray boxes). This means that actions in a given section won't take place until all actions are complete in the previous section. As shown in Figure 4.2.3a, the first step to initiate the VI is the "fire" button. One of the two sensors has to be "zeroed" internally in the VI (MTI 2) because it doesn't have a controller, which allows for manual external zeroing (MTI 1). After this button is activated on the front panel, the average of 1000 points for the stand alone optical sensor is calculated, as shown in Figure 4.2.3b (channel ai5). This value is then stored until the remainder of the section is complete. Following this, four analog voltage inputs (ai) are established (Figure 4.2.3c): two for the optical displacement sensors (ai4 and ai5) and two for the velocity sensors' op-amp outputs (ai6 and ai7). The most important part of this step is the inclusion of the "start digital edge" block. This lets the VI know to **not** start recording data from the inputs until a rising edge signal is detected from a digital output channel (PFI4). Once this is completed, the VI continues to the next section.

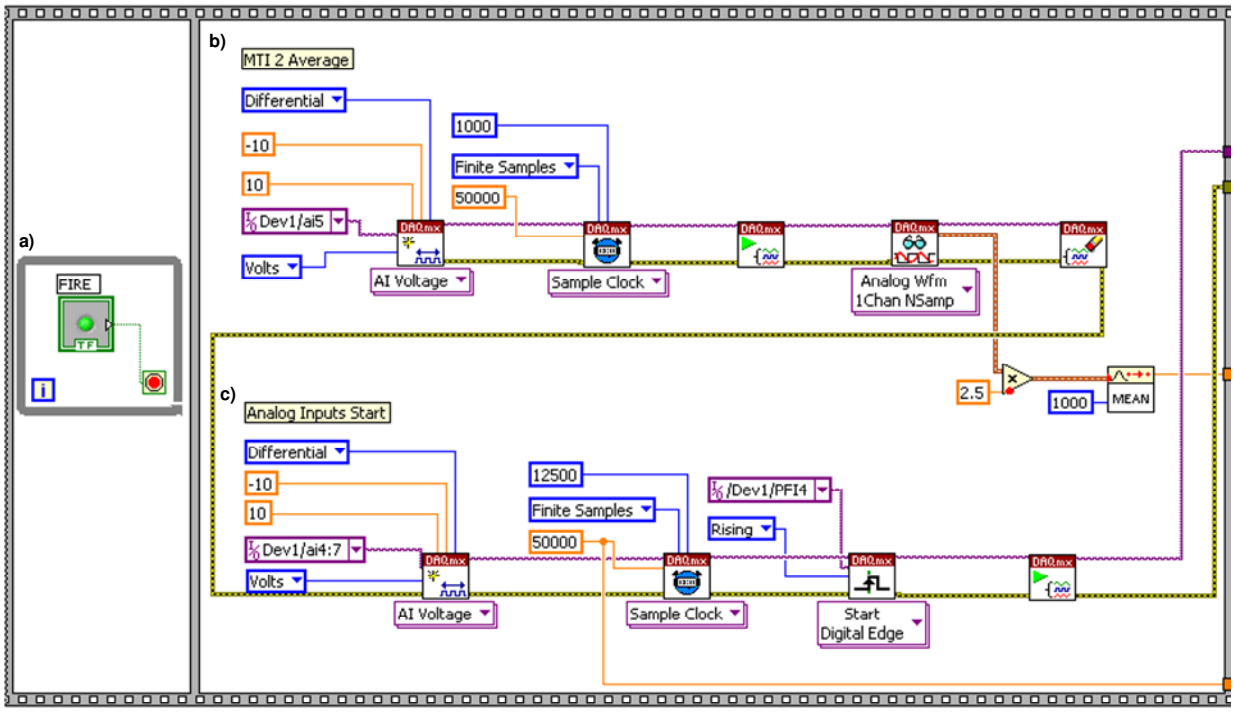

Figure 4.2.3 Block diagram of: a) VI initiation, b) average of stand-alone optical sensor, and c) definition of four analog inputs (laser displacement sensors and velocity sensor op-amps)

In this section of the VI (Figure 4.2.4), the digital output is initiated as a digital high output through channel PFI4 (Figure 4.2.4a). A digital "true" (positive 5 volts), is sent for an "output time" specified by the user on the front panel. After this time (in milliseconds) has passed, the digital "true" becomes a digital "false," or zero volts. As discussed above, the VI is waiting for this positive edge from digital channel PFI4 to start reading data from the four analog inputs (Figure 4.2.4b). At this point, the VI reads the four input channels (4-D array) and splits the signal into four 1-D arrays (Figure 4.2.4c). Voltages from the optical sensors are multiplied by 2.5 to convert the signals' units to millimeters. Finally, the stand alone displacement sensor is zeroed with the average value calculated from the previous section (Figure 4.2.4d). Note that the "green" sensor is the photoresistor that the impactor passes first, followed by the "yellow" sensor.

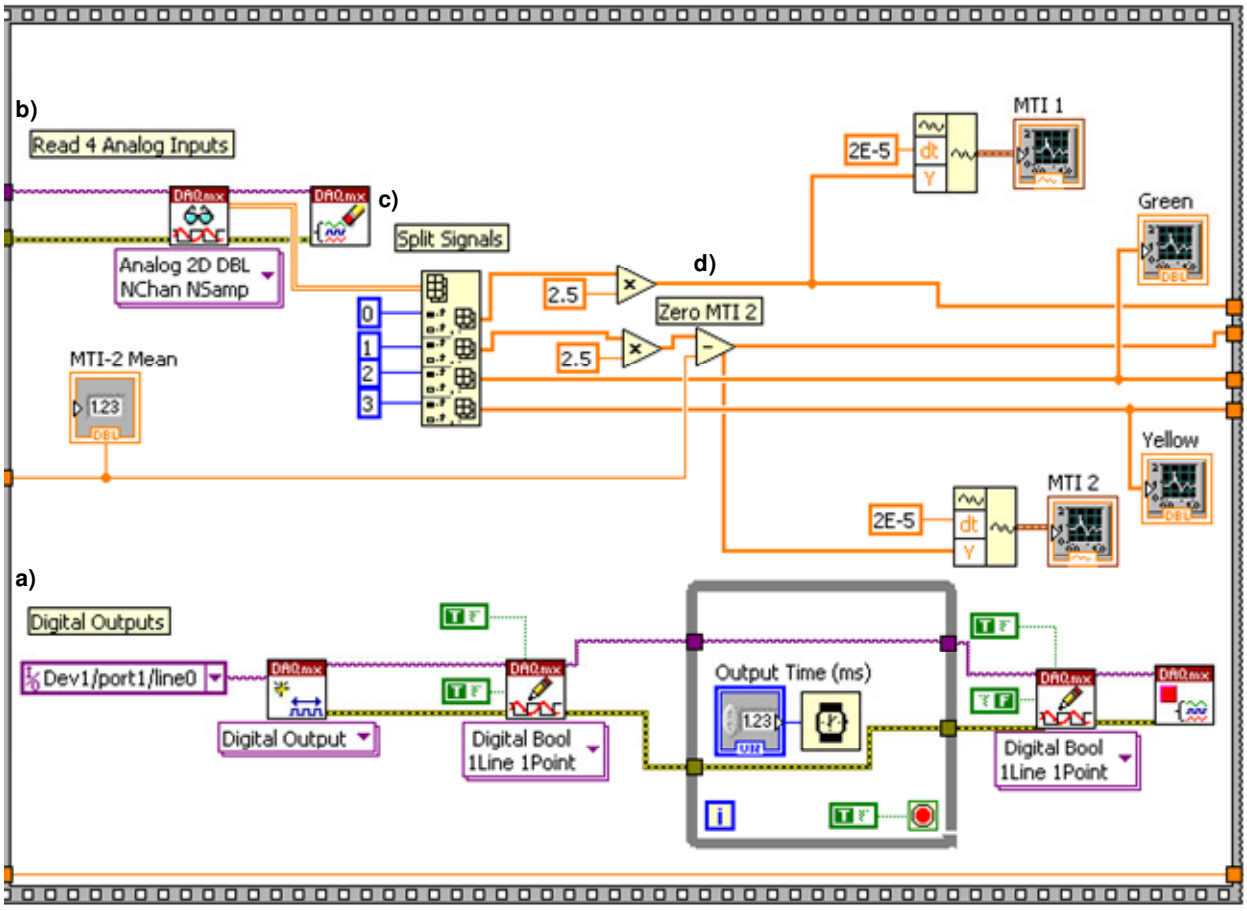

Figure 4.2.4 Second LabVIEW VI section where the a) digital output is initiated for a user-specified amount of time, b) analog inputs are read and c) split, and d) MTI 2 is zeroed

The following section can be considered the post-processing and writing of data (Figure 4.2.5). At this point, the impact event is complete and several operations occur before the data is written. As shown in Figure 4.2.5a, a "for loop" creates a time column for the two displacement sensors. It is written based on the length of the data vectors (12500 points) and the sampling rate (50000 Hz) with the total time recorded being 0.25 seconds. This vector is then combined with the two columns of displacement data to be written into the text file. As previously mentioned, it is important to know which photoresistor is tripped first when calculating the impact velocity. That is because the velocity is calculated using the time it takes to travel the known distance between the two photoresistors. The value of the voltage output of the op-amp is trivial, but the VI is designed to search for the change in the voltages. As shown in Figure 4.2.5b, the output is cycled through a "while loop" until a given condition is met. The loop compares the value of the initial voltage, which corresponds to the highest incident light intensity from the laser, and

compares each successive point to this first number. When the loop detects that a data point is more than 25 mV greater than that first point, the loop is terminated. The value of the voltage when this happens isn't important, but the number of the data point is. Once loop ending conditions are met for both sensors, the difference between data point numbers is calculated. This is then divided by sampling rate (to give a time between tripping of sensors) and then divided into the known distance between the lasers to give the impact velocity (Figure 4.2.5c). The final step of the VI is to write the data to a text file. A "write file" button on the front panel is pressed to initiate the file saving process. Once this begins, a header is created using scripts with inputs from the user, computer clock and the VI (Figure 4.2.5d). The header includes the time and date the test was completed, the panel number (user input), impact velocity (calculated in the VI), the time vector (created in the VI), and two displacement vector arrays.

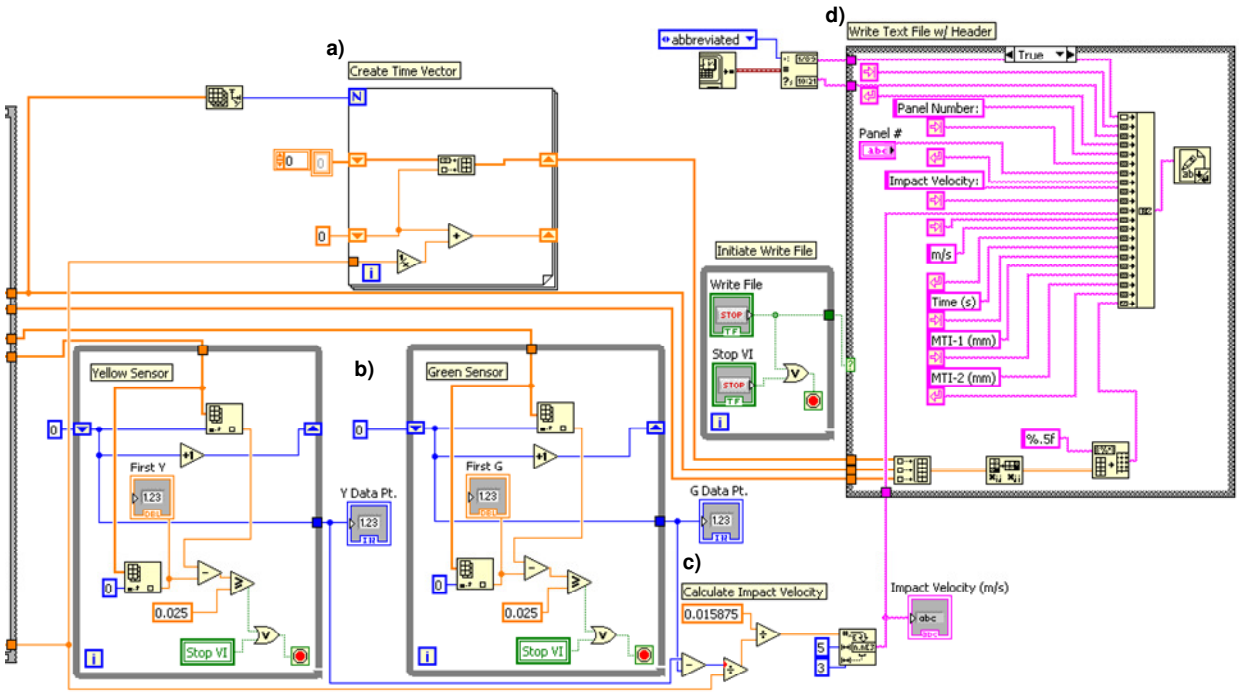

Figure 4.2.5 Post-processing of data including the: a) creation of time vector for displacement arrays, b) search for voltage change in op-amp outputs, c) velocity calculation and d) writing of the text file with a custom header

4.2.2 Solenoid Valve Actuation

Before the digital high is output by the LabVIEW VI (Figure 4.2.4a), the user specifies the output time in milliseconds. For triggering of the DSO and reading analog data in the VI, the length of the output voltage signal is inconsequential. This is because they are both waiting for a positive edge (sudden change from 0 to 5 V). This output voltage time is important when involved with the opening duration of the direct acting solenoid valve releasing air from the pressure chamber (Figure 4.2.6a). At lower pressures (10–30 psi), a lower valve opening time is allowable, but with pressures higher than 30 psi a longer amount of time is necessary to break the pressure seal. Minimal valve opening time is desirable since the possibility of double impacts is reduced. Note that this valve has a maximum allowable value of 100 psi, but pressures used for testing are typically less than 60 psi. A valve circuit is used which is powered by a 120 VAC source, but through a transformer provides the 12 VDC and 1.5 amps required for the valve (Figure 4.2.6b). The digital out from the LabVIEW VI triggers "transistor 1," which then trips the larger "transistor 2" allowing the valve to be actuated. A diode is included to dissipate an inductive voltage spike resulting from the sudden electrical trigger.

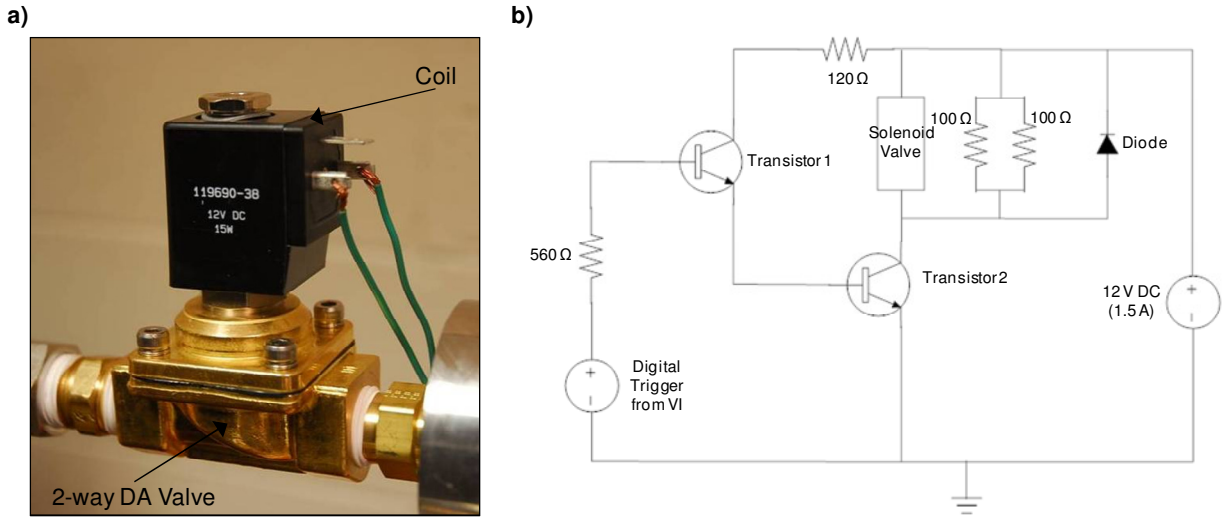

Figure 4.2.6 a) Direct acting solenoid valve with magnetic coil and b) coil actuation circuit

Chapter 5

Results of Impact Testing

This chapter outlines the impact test results for nine different configurations of the multi-layered polymers. The multi-laminate samples consist of a 1.5875 mm (1/16 in) PMMA front panel, an interlayer/adhesive (0.5–0.635 mm), and a 1.5875 mm (1/16 in) PC back layer. A two-layered PMMA and PC (without an interlayer) sample, as well as two other unbonded configurations with TPU interlayers, are also tested. A summary of the testing configurations, bonding conditions, interlayer color, and average impact speed is given in Table 5.1. Interlayer color is noted since transparent multi-laminates could have specific applications for impact resistant windows or armor. As discussed in Chapter 4, samples are impacted with a hemi-spherical steel impactor with mass of 28.5 grams at impact speeds of 12 and 22 m/s. This corresponds to concurrent modeling calculated strain rates on the order of $100\ s^{-1}$. Three multi-laminates are tested for each configuration and impact speed. Representative force and displacement traces are given for each interlayer and velocity. Energy absorption mechanisms and fracture observed is compared for various interlayers, impact speeds, and bonding conditions.

5.1 Impact Force and Displacement Results

5.1.1 Force Trace Signal Conditioning

Impact force data is acquired from the instrumented shock accelerometer by the digital storage oscilloscope (DSO), after which signal conditioning is performed. The LabVIEW VI ensures that displacement and force data are temporally aligned by triggering the DSO and displacement data acquisition at a common reference time. Note that the DSO is set to "high resolution mode," which is essentially an electronic low-pass filter attenuating high frequency electrical noise inherent in the force signal. A "single shot" mode is also utilized in the DSO which allows data for each impact event to be manipulated and analyzed after each impact using scaling and zooming capabilities. Initially, the oscilloscope is scaled in order to obtain data throughout the

whole experiment, including travel of the impactor down the barrel before impact. For both impact velocities, horizontal scaling is 20 ms/division, so the oscilloscope will show data for 200 ms in total. Unlike time scaling, vertical scaling is different for each impact velocity. For 12 m/s, the vertical resolution is set to 100 mV/division, while for 22 m/s it is 200 mV/division. If the oscilloscope is not correctly scaled for the test, the data will be clipped and can't be recovered in post-processing. Therefore, great care is taken before each test to ensure force data will be captured in its entirety. Since the DSO is capable of storing 8 million data points but displays only a fraction of this (10000), the impact event can be brought into focus after impact. By increasing horizontal resolution (decreasing time per division), more data points are included on the display and can be saved.

Table 5.1 Summary of multi-laminate configurations and average impact speeds

Component Materials	Boundary Condition	Interlayer Color	Ave Impact Speed (m/s)
PMMA/PC	Un-Bonded	N/A	12.2
PMMA/PC	Un-Bonded	N/A	22.1
PMMA/DFA4700/PC	Un-Bonded	None	11.7
PMMA/DFA4700/PC	Un-Bonded	None	22.7
PMMA/IM800A/PC	Un-Bonded	None	12.2
PMMA/IM800A/PC	Un-Bonded	None	22.4
PMMA/DFA4700/PC	Bonded	None	12.3
PMMA/DFA4700/PC	Bonded	None	22.7
PMMA/IM800A/PC	Bonded	None	12.4
PMMA/IM800A/PC	Bonded	None	22.3
PMMA/VHB4905/PC	Bonded	None	11.8
PMMA/VHB4905/PC	Bonded	None	21.4
PMMA/VHB5925/PC	Bonded	Black	11.9
PMMA/VHB5925/PC	Bonded	Black	22.1
PMMA/VHB4936/PC	Bonded	Gray	12.3
PMMA/VHB4936/PC	Bonded	Gray	21.9
PMMA/VHB4930/PC	Bonded	White	12.7
PMMA/VHB4930/PC	Bonded	White	21.9

The raw data from the shock accelerometer contains high frequency noise which arises from unfurling of the accelerometer trail wire along its trajectory. This acceleration and wire activity

during travel down the barrel, and throughout the impact, causes noise. Therefore, post-process filtering of the data is imperative for quantitative analysis. As shown in Figure 5.1.1, a moving average MATLAB "smoothing" function is able to eliminate "outlier" data while maintaining the general shape of the underlying traces. All force traces are smoothed by averaging every 50 points consecutively, and this value is chosen to adequately smooth data without amplitude loss. Representative raw data is shown in Figure 5.1.1a with smoothed data in Figure 5.1.1b. Since the traces can be smoothed without distortion of shape, the noise is not viewed as a significant issue and can be assumed to be negligible. While most of the scatter seen results from the wire, it is important to realize that fracture may cause sudden minor decreases/increases in the force signal, which may be perceived as noise and unintentionally smoothed away. Note that immediately following impact, the force signal reaches a negative value (Figure 5.1.1). Impactor movement away from the multi-laminate, and friction between the barrel and impactor sheath, causes a change in direction of internal seismic mass (Figure 4.1.3b) acceleration. While the sensor remains in net compression during loading and reloading of the impactor (negative voltage output), the forces on the impactor during rebound cause net tension of the sensor and a resulting positive voltage output. All force signals shown are inverted by the digital oscilloscope to improve clarity. For an impact velocity of 12 m/s, this negative output lasts for less time (~5 ms) with a smaller amplitude when compared to an incident impactor speed of 22 m/s (~10 ms). This supports the idea that a friction force is a damping effect whose magnitude can be assumed proportional to velocity, which can be seen qualitatively in Figures 5.1.6, 5.1.7, and 5.1.8.

5.1.2 Double Impact and Local Displacement

It is observed that two force peaks occur for a presumable single impact event (Figure 5.1.1). Each trace has two peaks with a local minimum between them, and at first glance, this would lead one to assume a double impact is responsible. However, the force does not reach zero and signal is not lost during the impact. This implies that the impactor does not lose contact with the sample and therefore, does not impact the sample twice. Furthermore, for this type of impact event (duration/magnitude), a double impact would be detected by the displacement sensors. To demonstrate, consider a 12.7 mm (0.5 in) thick PC specimen, impacted to create an intentional double impact. Figure 5.1.2 shows the force and deflection versus time relationships on a single

plot. It is clear that two impacts occur on the target approximately 25 ms apart. Note that the force attains a value of zero before the second impact occurs, indicating loss of contact between the impactor and the sample. This plot also shows that the laser displacement sensors are able to detect the two individual impact events seen as two separate panel oscillations.

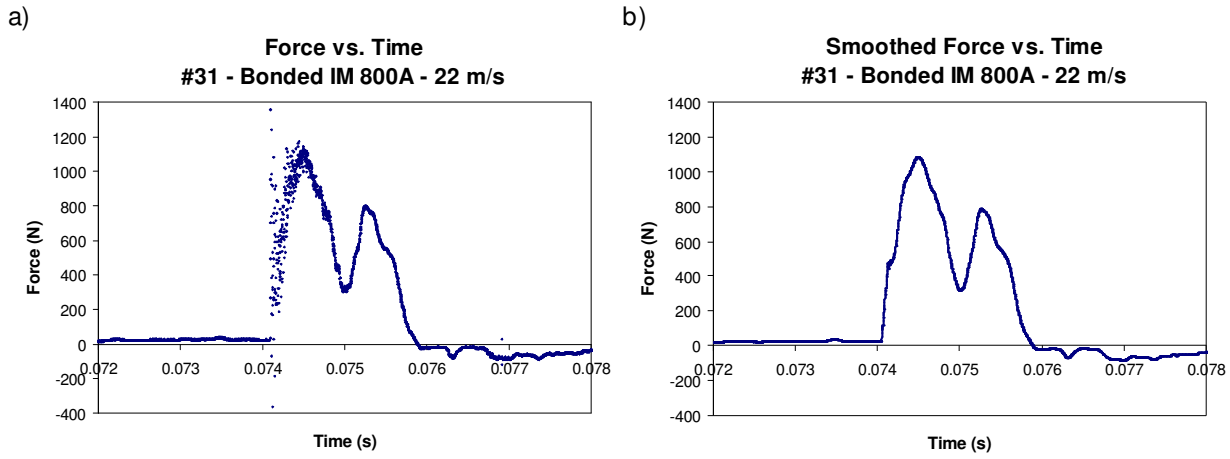

Figure 5.1.1 Force signals for 22 m/s impact on bonded IM 800A multi-laminate: a) raw force data and b) smoothed force data

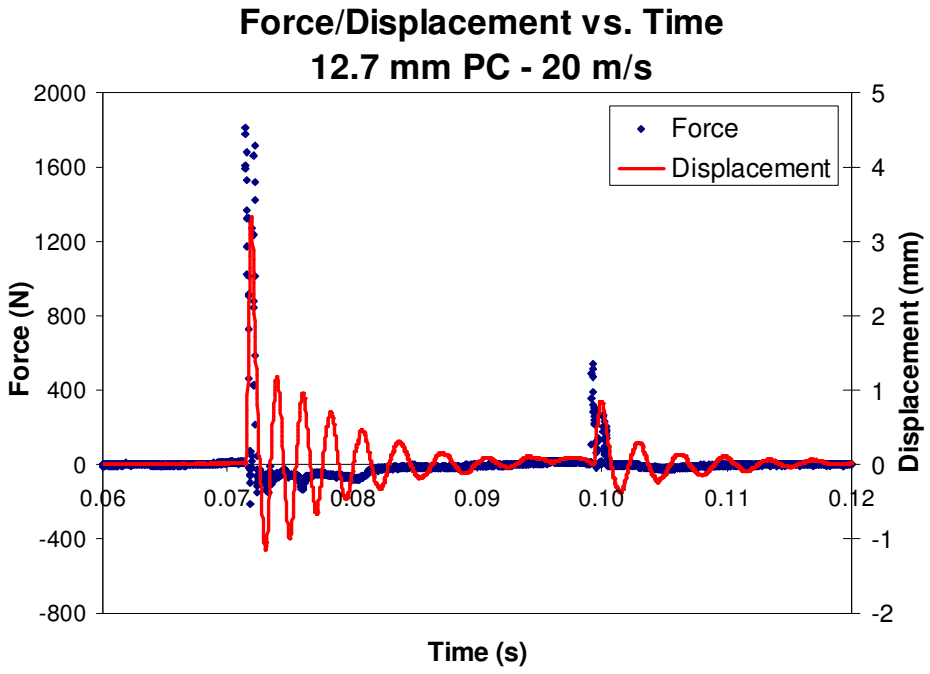

Figure 5.1.2 Force and displacement traces for a 20 m/s double impact on 12.7 mm thick PC

Although it has been shown that a double impact is not occurring for this suite of structural tests, an understanding of the true source of the second force peak is necessary. The second peak occurs because of rebound caused by large elastic deflections of the multi-laminate. This is confirmed by high speed videos taken at 20,000 fps with a Photron SA5 video camera, with results discussed in Section 5.1.3.

When impact occurs, the global panel displacement at the impact site is moving away from the optical sensors (positive), but as shown in Figure 5.1.3a, the optical sensors record slight displacement towards them (negative). This happens because of a local displacement in the opposite direction of the global deflection at the center of the panel. Figure 5.1.3b depicts a deformation profile for the impact site of the sample. If center deflection were recorded, values would immediately become positive as the impact begins. The schematic shown is purposefully exaggerated and is not intended to be representative of actual displacements or proper scaling.

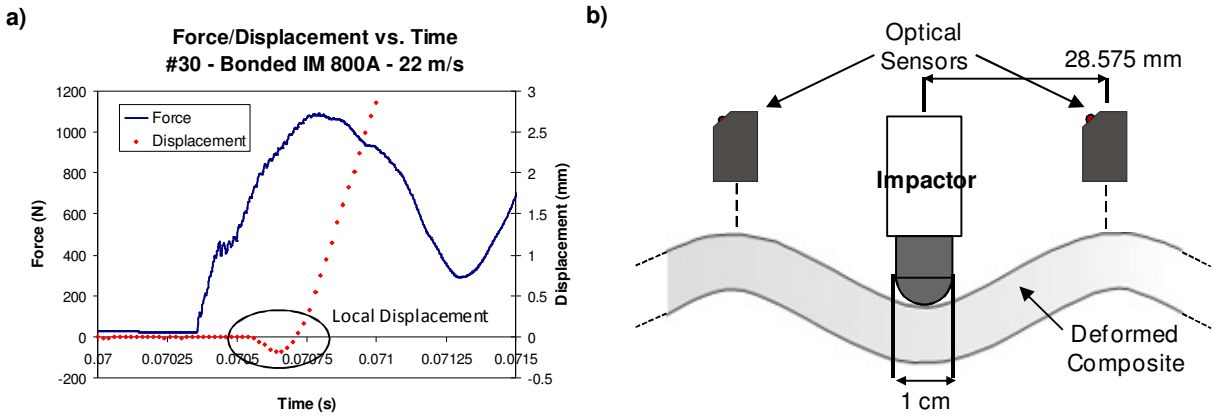

Figure 5.1.3 Local displacement shown with a) representative data and b) impact site schematic

5.1.3 Force and Displacement vs. Time

By overlaying force and displacement traces on the same time axis, the sequence of impactor deceleration and panel displacement can be better understood. Contact force is measured at the center of the target while displacement is measured off-center (28.575 mm/1.125 in), so that there is a delay observed between initiation of contact force and initial deflection (Figure 5.1.3a). If displacement was measured at the impact site, the displacement curve would be shifted to the

left so that both traces were initiated at the same time (for the loading rates considered). This time delay is measured for several representative samples for each interlayer and this value was shown to be consistently between 0.2 and 0.25 ms. This is representative of the time required for the impact disturbance to propagate radially outward from the impact site. Although magnitudes reported would be fractionally less than actual impact site displacement, concurrent analysis of force and displacement signals for determining the sequence of events can assume the displacement trace is shifted (Figure 5.1.4).

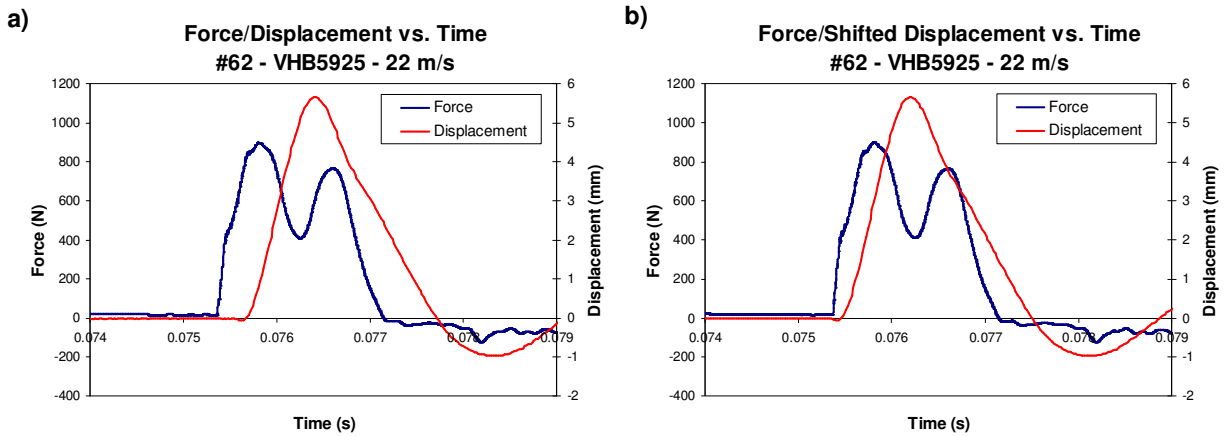

Figure 5.1.4 Force and displacement as a function of time a) as recorded without a displacement trace shift and b) with a displacement trace shift

At initiation of impact, both contact force and deflection begin to increase. The first force peak occurs during deflection and is observed before maximum displacement is reached. As the panel reaches its maximum displacement, a decrease of contact force on the impactor occurs, until a local minimum is achieved at maximum deflection. Note that this contact force never reaches zero, therefore only a single impact is occurring (as demonstrated in Section 5.1.2). The first contact force peak is approximately midway between initial and maximum displacement, and force decreases to a local minimum as the maximum displacement is approached. At the time of the local minimum, the multi-layered polymer has stored some elastic energy from the impact, and reloads the impactor as it deflects back towards its initial position. At this point, the energy stored is greater than the current instantaneous kinetic energy of the impactor and so the kinetic energy of the panel dominates the contact force signal. This reloading of the impactor (rebound)

causes an increase in the net contact force resulting in a second force peak. As shown in Figures 5.1.6, 5.1.7, and 5.1.8 the impactor reaches a value of zero (loses contact) between 0.15 and 0.5 ms before the multi-laminate returns to the initial position, and the panel continues to oscillate after impact. As mentioned earlier, measures were taken to ensure the temporal alignment of all data acquired so that any delay observed is not electrical, and would be easily identified and explained mechanically. If the target material had a reduced span to thickness ratio, there would be only one sharp, high magnitude force peak with minimal specimen deflection and a short impactor contact time (pulsewidth). For the tested specimen geometry, the multi-layered polymer is allowed to substantially deflect elastically, allowing for longer impact duration, lower impactor contact force magnitudes, and the development of a second force peak during rebound. The significance and value of this second force peak and how it relates to impact performance will be discussed further, and compared for different configurations, in Chapter 6.

A high speed video is taken at 20,000 fps on a bonded PMMA/VHB4930/PC sample at 22 m/s (Figure 5.1.5). Observations of individual frames helped justify the above analysis. After initiation of contact (Figure 5.1.5a), indentation of the PMMA layer occurs and cracks propagate from the center (Figure 5.1.5b). This particular sample displays delamination (Figure 5.1.5c) as it deflects towards maximum displacement (Figure 5.1.5d). The value of 0.7 ms to reach maximum displacement is very close to the measured value for the other bonded VHB 4930 samples impacted at 22 m/s (0.689 ms). This will be discussed further in Section 6.1.2. As the impactor is reloaded during rebound, new cracks are formed and previous cracks are lengthened (Figure 5.1.5e) while the multi-laminate returns to its initial position (Figure 5.1.5f).

Representative force and displacement traces for each configuration and impact speed are shown in the three figures below on the same time scales (Figure 5.1.6, Figure 5.1.7, and Figure 5.1.8). Each plot shows data for 5 ms to allow for comparison between all interlayers, configurations, and impact velocities. Figure 5.1.6 features data for the three different unbonded configurations consisting of no interlayer and unbonded TPUs (DF A4700 and IM 800A) impacted at both impact speeds. These traces have significantly more noise in the signal than bonded samples, so the smoothed force traces are not as consistent and indicative of the raw signal. With more fracture in the front PMMA outerlayer, especially for the 22 m/s impact, cracks sometimes

propagate through the laser displacement sensors' reflective tape and consequently disrupt measurements. As can be seen in most of the displacement traces in Figure 5.1.6, there are data points that are definite outliers due to the displacement sensor outputting 12.5 mm (5 V) if nothing is detected, or incorrect displacement values from uneven reflection surfaces. Most of these inconsequential points are clipped by the scales on the plots shown. Figure 5.1.7 shows the force and displacement results for the TPU interlayers incorporated into bonded multi-laminates (DF A4700 and IM 800A), with Figure 5.1.8 for the 3M VHB polyacrylates (VHB 4905, VHB 5925, VHB 4936, and VHB 4930). Chapter 6 contains further analysis, discussion, and comparison of quantitative metrics measured from the force and displacement traces.

As discussed previously, all force traces contain two main peaks representing loading and unloading of the multi-laminate samples. In the case of the bonded multi-laminates, VHB 4936 and VHB 4930 force traces have a slightly different shape. These samples display a second local minimum force during the loading peak for both impact speeds (Figure 5.1.8e–h). It is discussed in Section 2.1 that a commonality in microstructure of these two materials is the inclusion of rigid microspheres. Through communication with 3M, it is realized that translation of these microspheres in the acrylic matrix is possible. It is hypothesized that during impact loading, the localized force at the impact site temporarily displaces the microspheres resulting in a decrease in amplitude. If this theory is correct, the response rate and translation distance remain unknown, and given the rate dependent visoscity of the acrylic matrix (Section 2.2), it is unclear if microsphere movement would occur at impact rates of strain. Nevertheless, the magnitude of force decrease reduces significantly with increasing impact velocity. This indicates that the responsible phenomenon is dependent on loading rate and local effective strain rate, and is severely restricted with increasing rate. It is believed that this apparent modulus reduction is not due to fracture or crushing, but could be due to elastic compression of the microspheres at the impact site. Therefore, further investigation is necessary to truly determine what is causing the secondary force decrease for these two adhesives.

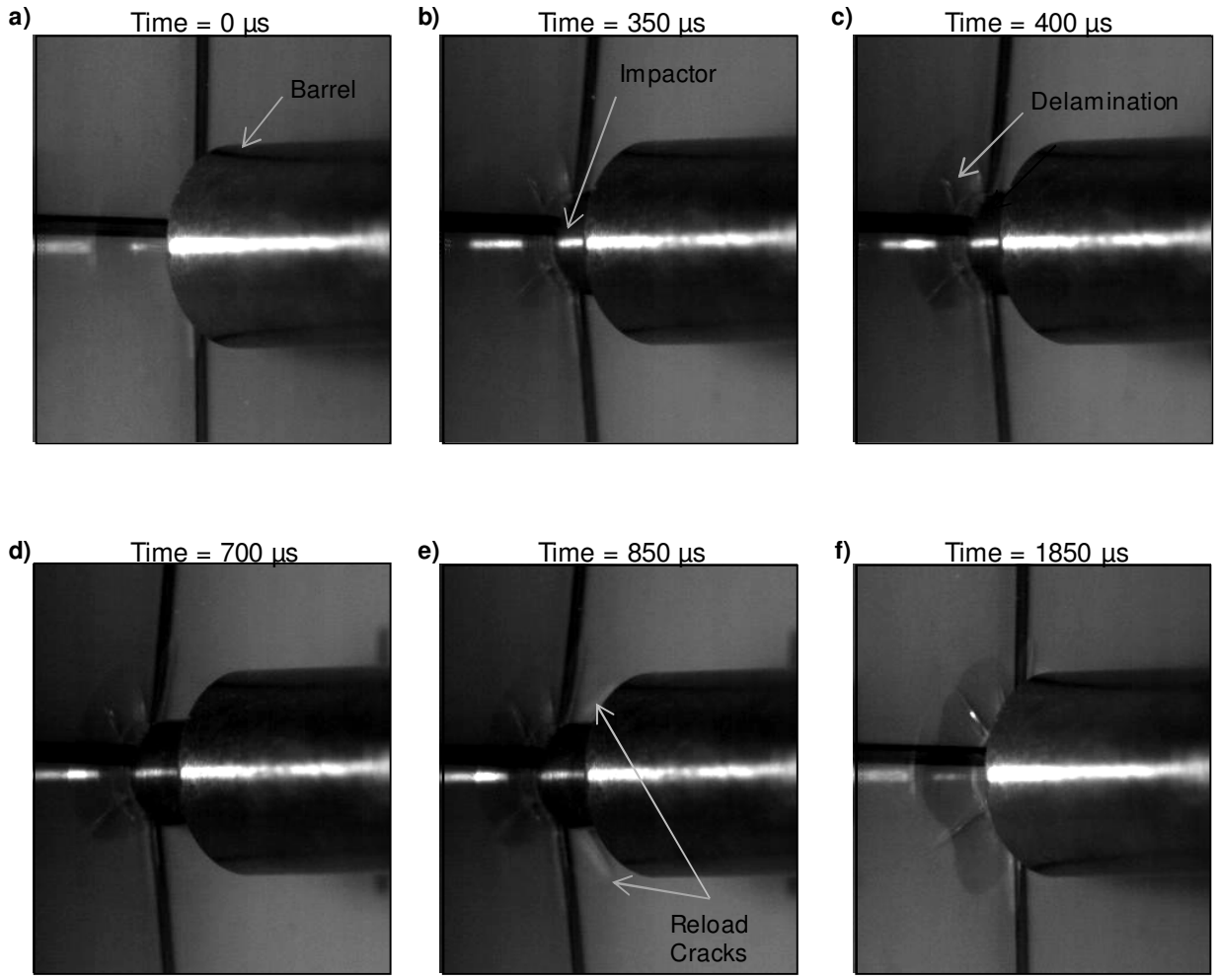

Figure 5.1.5 Freeze frames from 20,000 fps video of 22 m/s impact on bonded PMMA/VHB4930/PC sample with sequence of events being: a) initial contact, b) indentation and crack propagation, c) delamination, d) maximum deflection, e) reloading and further crack development, and f) return to initial position

a)

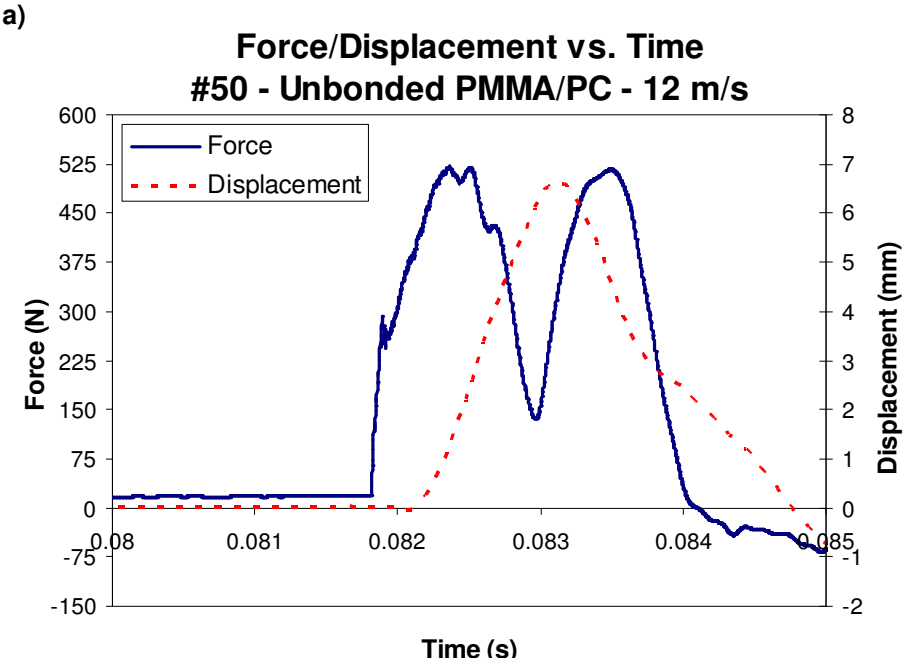
Force/Displacement vs. Time
#50 - Unbonded PMMA/PC - 12 m/s
Force
Displacement
Force (N)
Displacement (mm)
Time (s)
600
525
450
375
300
225
150
75
0
-75
-150
8
7
6
5
4
3
2
1
0
-1
-2
0.08
0.081
0.082
0.083
0.084
0.085

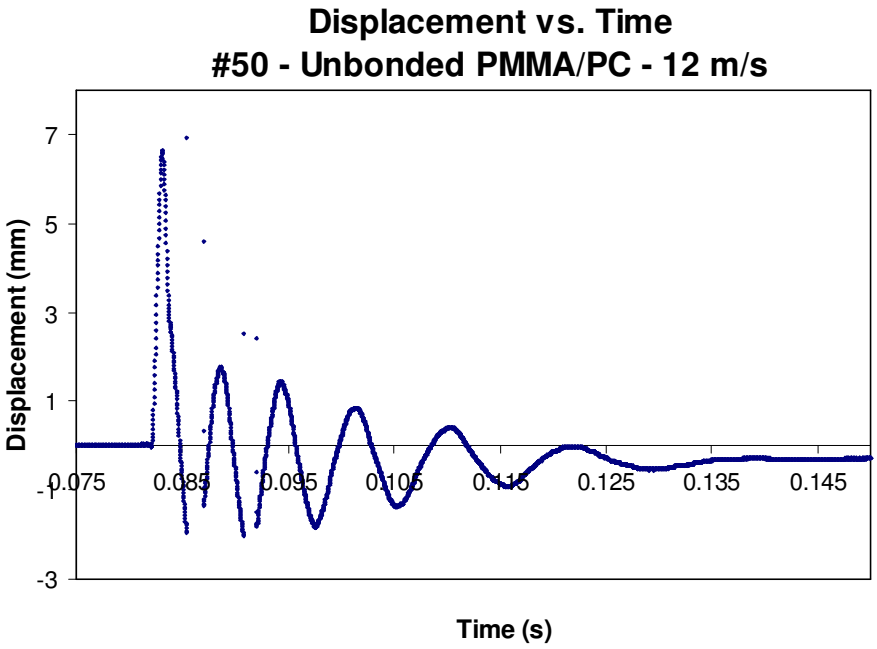
Displacement vs. Time
#50 - Unbonded PMMA/PC - 12 m/s
Displacement (mm)
Time (s)
7
5
3
1
-1
-3
0.075
0.085
0.095
0.105
0.115
0.125
0.135
0.145

b)

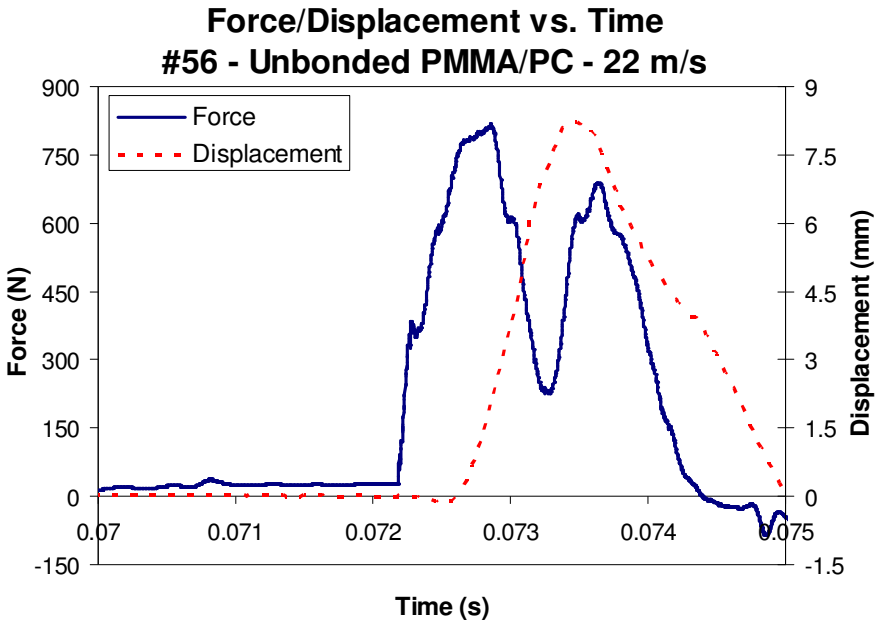
Force/Displacement vs. Time
#56 - Unbonded PMMA/PC - 22 m/s
Force
Displacement
900
750
600
450
300
150
0
-150
9
7.5
6
4.5
3
1.5
0
-1.5
0.07
0.071
0.072
0.073
0.074
0.075
Force (N)
Displacement (mm)
Time (s)

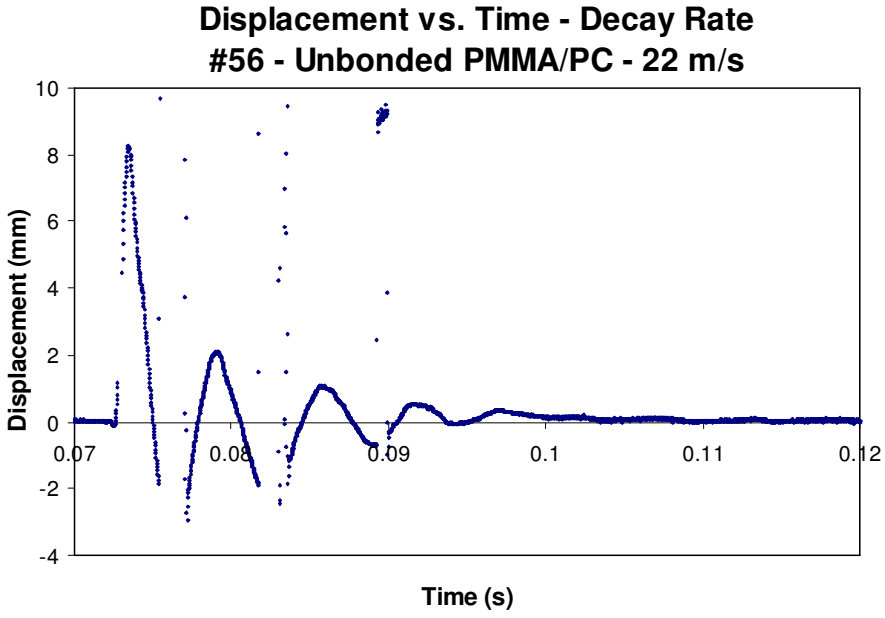
Displacement vs. Time - Decay Rate
#56 - Unbonded PMMA/PC - 22 m/s
10
8
6
4
2
0
-2
-4
0.07
0.08
0.09
0.1
0.11
0.12
Displacement (mm)
Time (s)

c)

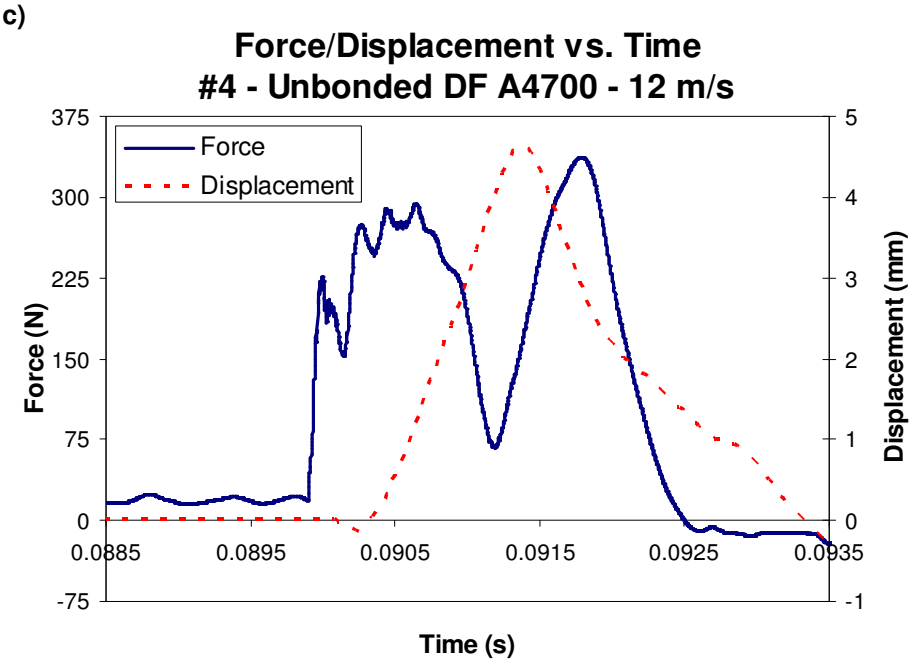
Force/Displacement vs. Time
#4 - Unbonded DF A4700 - 12 m/s
Force
Displacement
Force (N)
Displacement (mm)
Time (s)
375
300
225
150
75
0
-75
5
4
3
2
1
0
-1
0.0885
0.0895
0.0905
0.0915
0.0925
0.0935

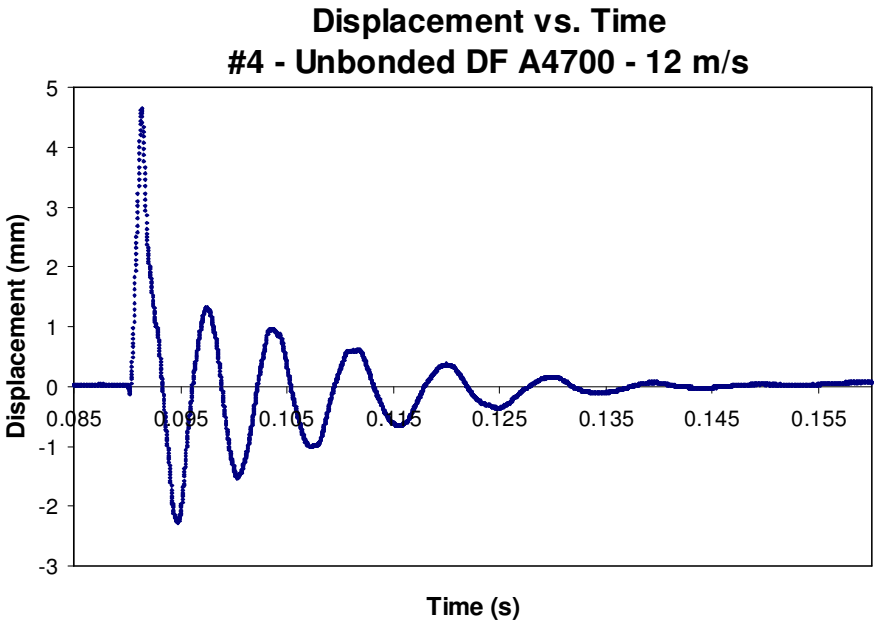
Displacement vs. Time
#4 - Unbonded DF A4700 - 12 m/s
Displacement (mm)
Time (s)
5
4
3
2
1
0
-1
-2
-3
0.085
0.095
0.105
0.115
0.125
0.135
0.145
0.155

d)

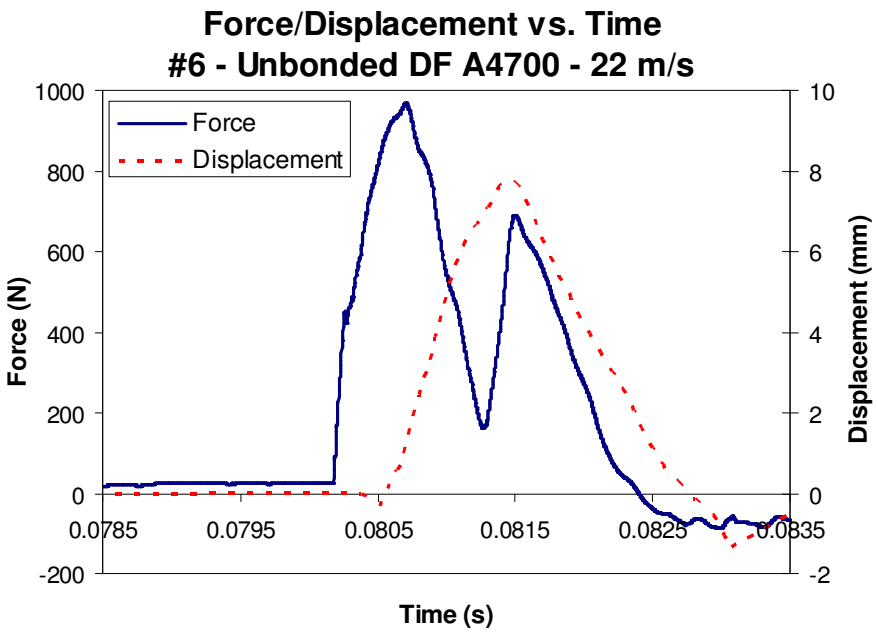
Force/Displacement vs. Time
#6 - Unbonded DF A4700 - 22 m/s
Force
Displacement
Force (N)
Displacement (mm)
Time (s)
1000
800
600
400
200
0
-200
10
8
6
4
2
0
-2
0.0785
0.0795
0.0805
0.0815
0.0825
0.0835

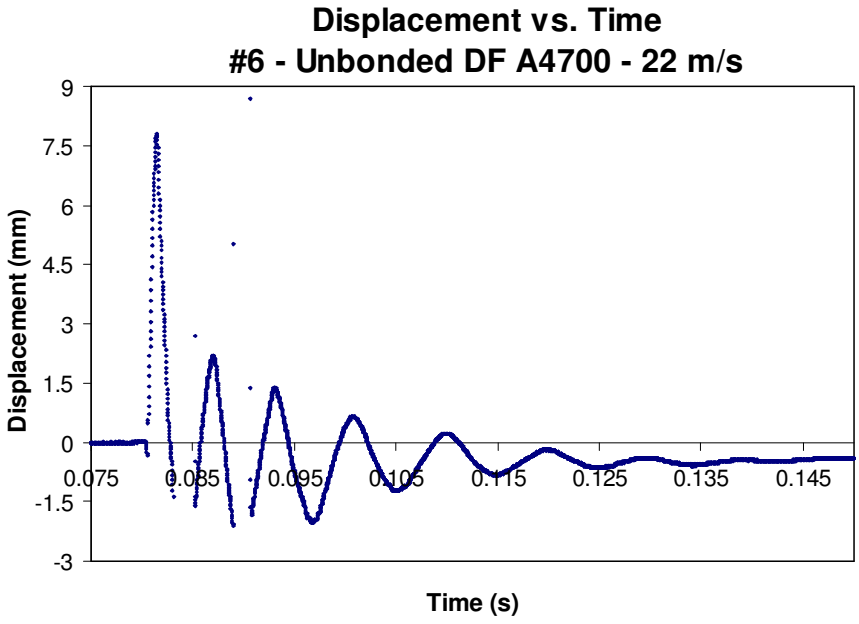
Displacement vs. Time
#6 - Unbonded DF A4700 - 22 m/s
Displacement (mm)
Time (s)
9
7.5
6
4.5
3
1.5
0
-1.5
-3
0.075
0.085
0.095
0.105
0.115
0.125
0.135
0.145

e)

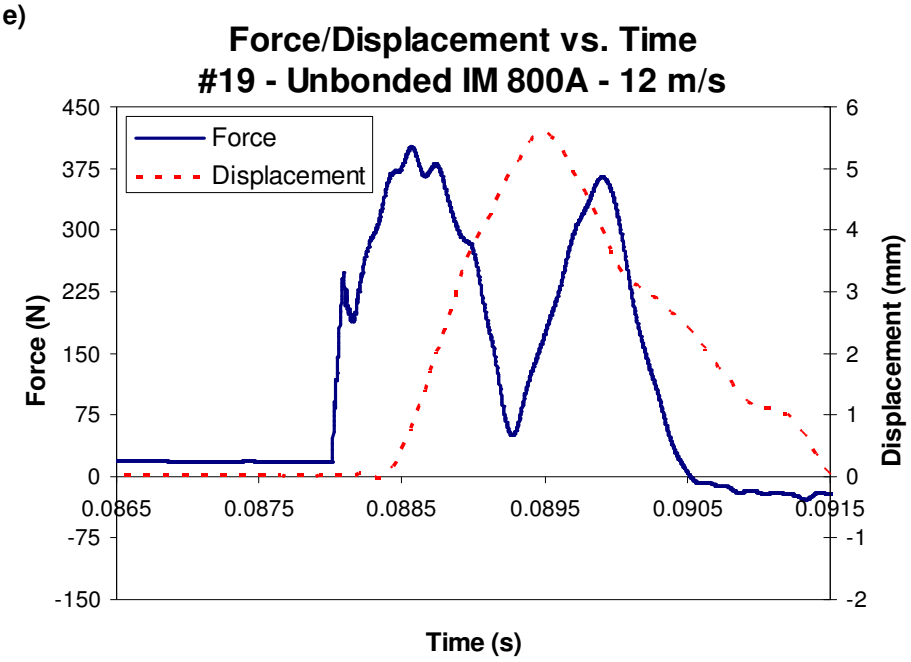
Force/Displacement vs. Time
#19 - Unbonded IM 800A - 12 m/s
Force
Displacement
Force (N)
Displacement (mm)
Time (s)
450
375
300
225
150
75
0
-75
-150
6
5
4
3
2
1
0
-1
-2
0.0865
0.0875
0.0885
0.0895
0.0905
0.0915

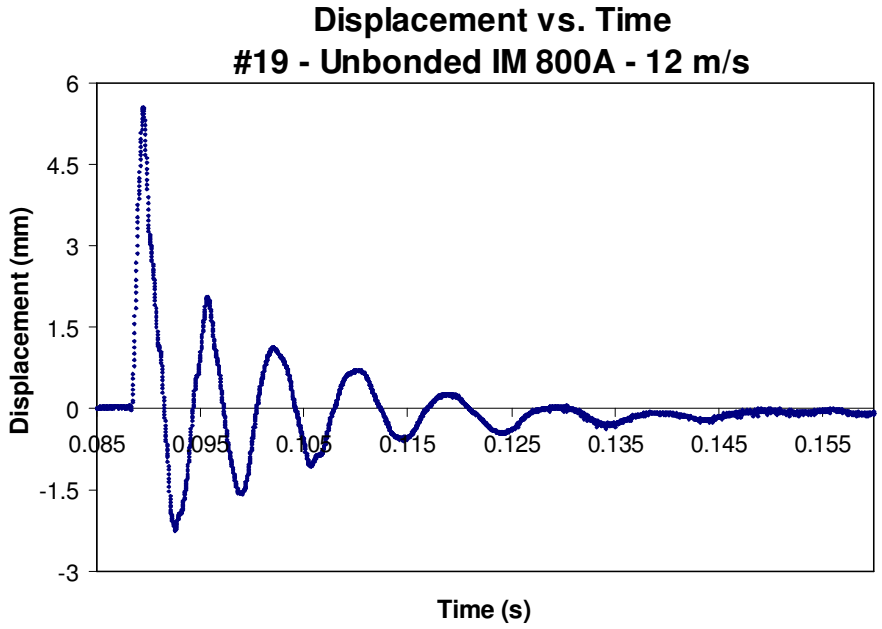
Displacement vs. Time
#19 - Unbonded IM 800A - 12 m/s
Displacement (mm)
Time (s)
6
4.5
3
1.5
0
-1.5
-3
0.085
0.095
0.105
0.115
0.125
0.135
0.145
0.155

f)

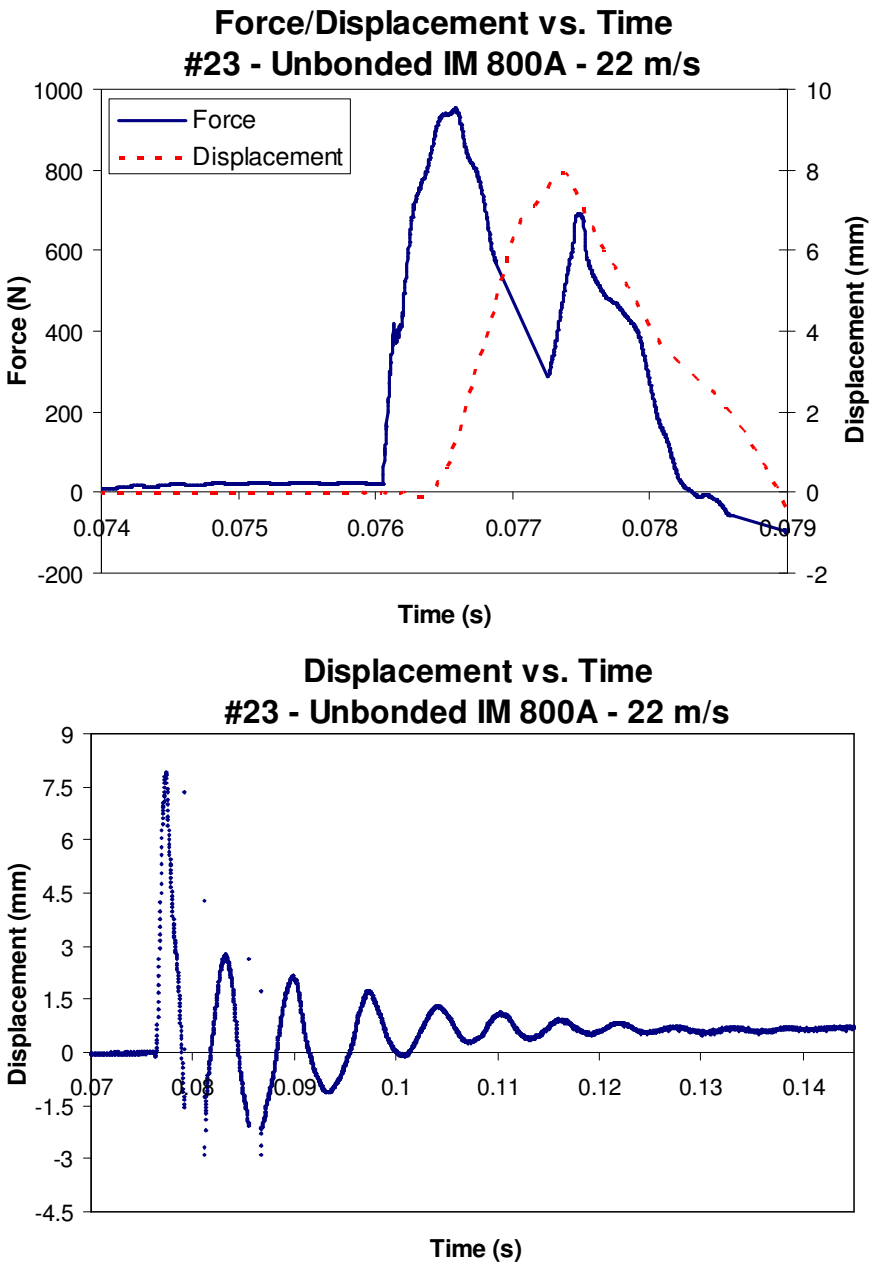

Figure 5.1.6 Impact force and displacement data for unbonded multi-laminates: a) 12 m/s no interlayer, b) 22 m/s no interlayer, c) 12 m/s DF A4700, d) 22 m/s DF A47000, e) 12 m/s IM 800A and f) 22 m/s IM 800A

a)

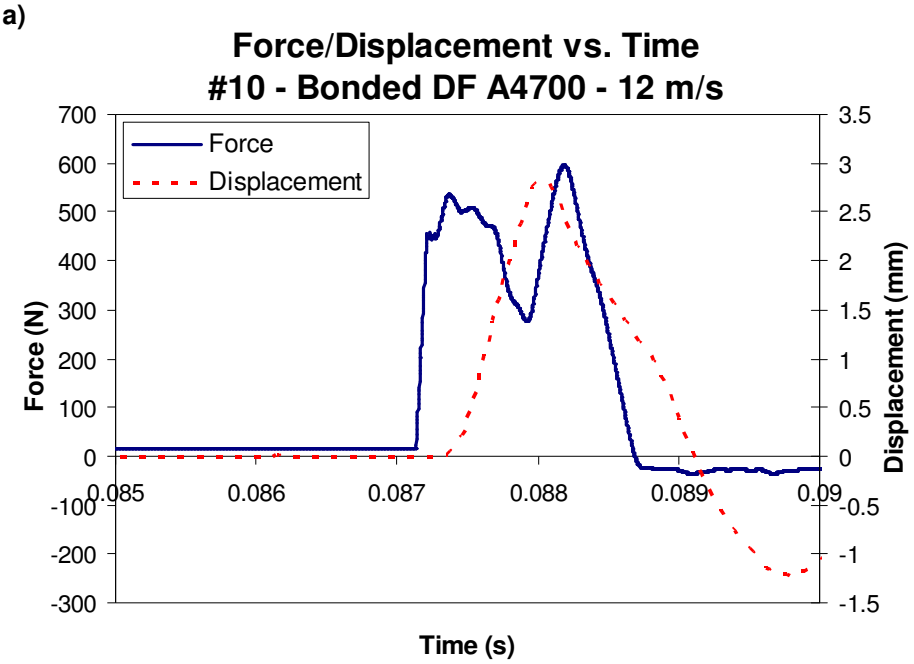
Force/Displacement vs. Time
#10 - Bonded DF A4700 - 12 m/s
Force
Displacement
Force (N)
Displacement (mm)
Time (s)
700
600
500
400
300
200
100
0
-100
-200
-300
3.5
3
2.5
2
1.5
1
0.5
0
-0.5
-1
-1.5
0.085
0.086
0.087
0.088
0.089
0.09

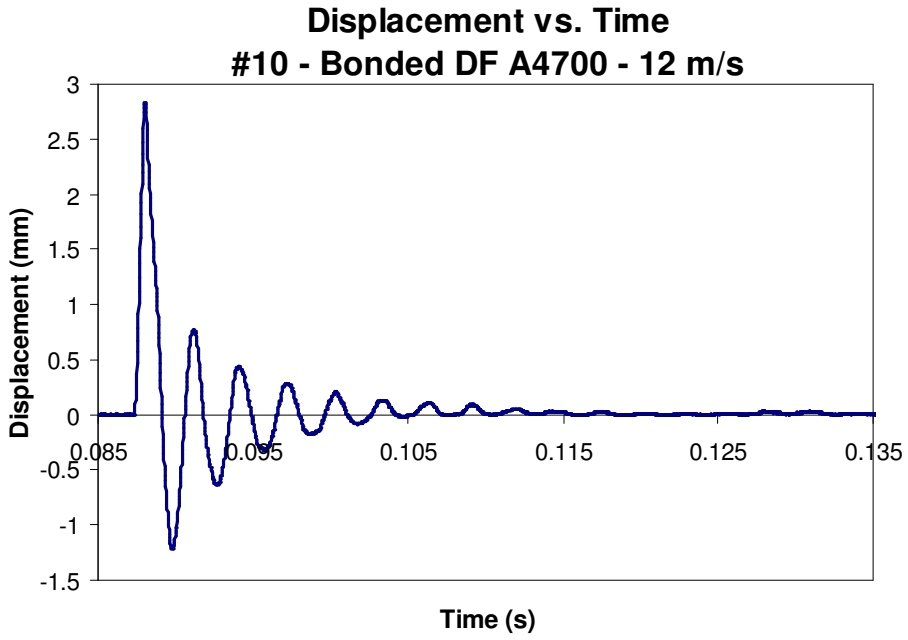
Displacement vs. Time
#10 - Bonded DF A4700 - 12 m/s
Displacement (mm)
Time (s)
3
2.5
2
1.5
1
0.5
0
-0.5
-1
-1.5
0.085
0.095
0.105
0.115
0.125
0.135

b)

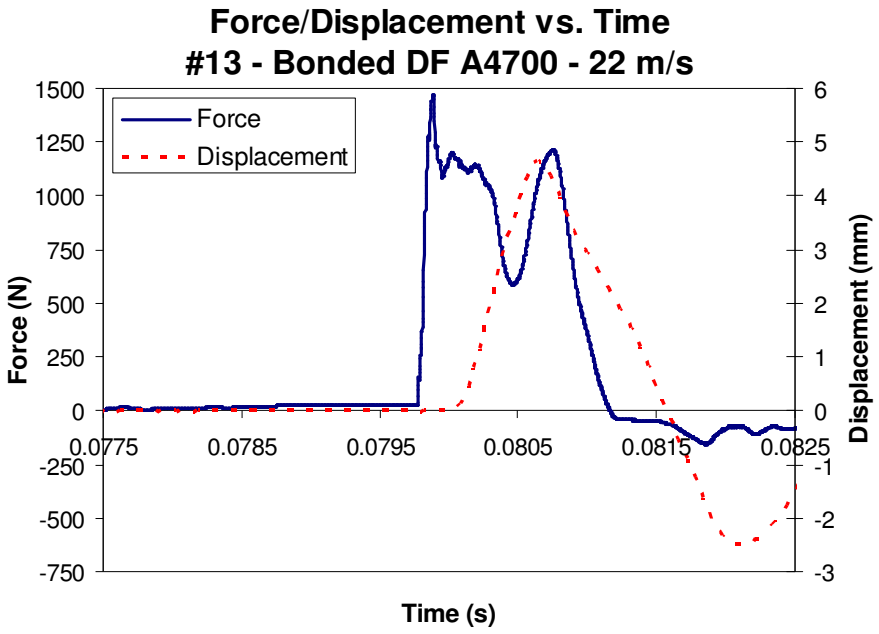
Force/Displacement vs. Time
#13 - Bonded DF A4700 - 22 m/s
Force
Displacement
Force (N)
Displacement (mm)
Time (s)
1500
1250
1000
750
500
250
0
-250
-500
-750
6
5
4
3
2
1
0
-1
-2
-3
0.0775
0.0785
0.0795
0.0805
0.0815
0.0825

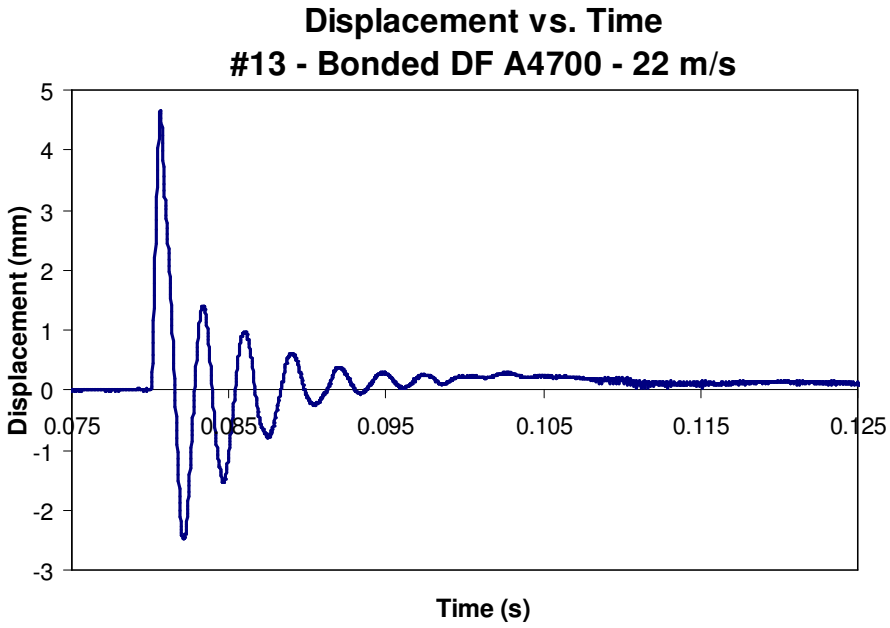
Displacement vs. Time
#13 - Bonded DF A4700 - 22 m/s
Displacement (mm)
Time (s)
5
4
3
2
1
0
-1
-2
-3
0.075
0.085
0.095
0.105
0.115
0.125

c)

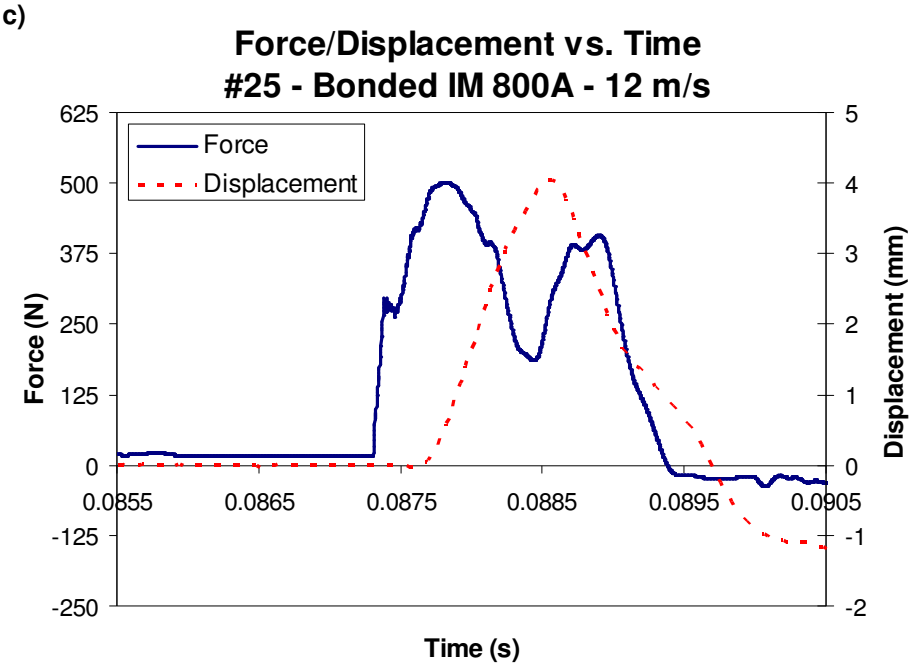
Force/Displacement vs. Time
#25 - Bonded IM 800A - 12 m/s
Force
Displacement
Force (N)
Displacement (mm)
Time (s)
625
500
375
250
125
0
-125
-250
5
4
3
2
1
0
-1
-2
0.0855
0.0865
0.0875
0.0885
0.0895
0.0905

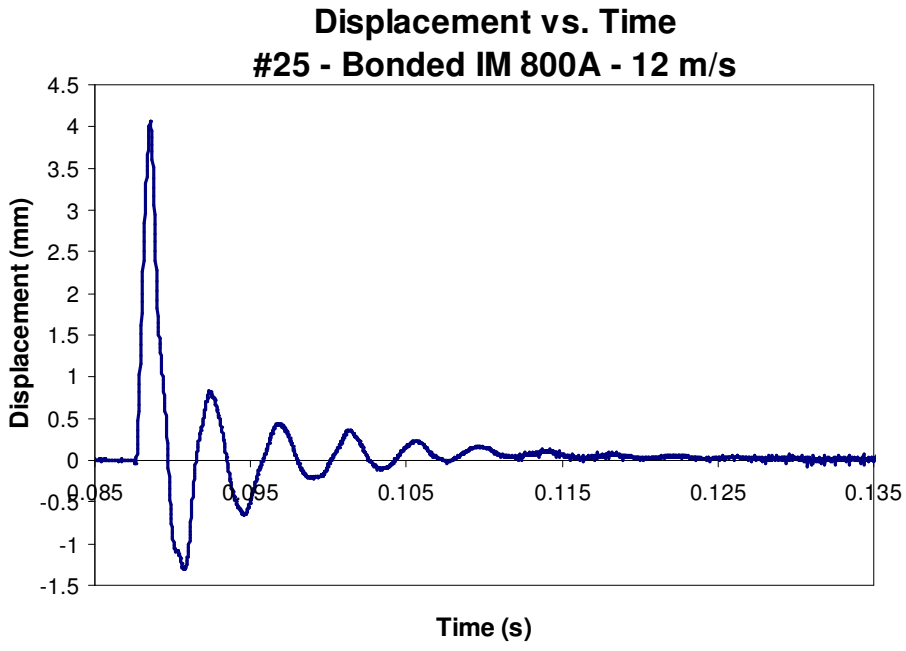
Displacement vs. Time
#25 - Bonded IM 800A - 12 m/s
Displacement (mm)
Time (s)
4.5
4
3.5
3
2.5
2
1.5
1
0.5
0
-0.5
-1
-1.5
0.085
0.095
0.105
0.115
0.125
0.135

d)

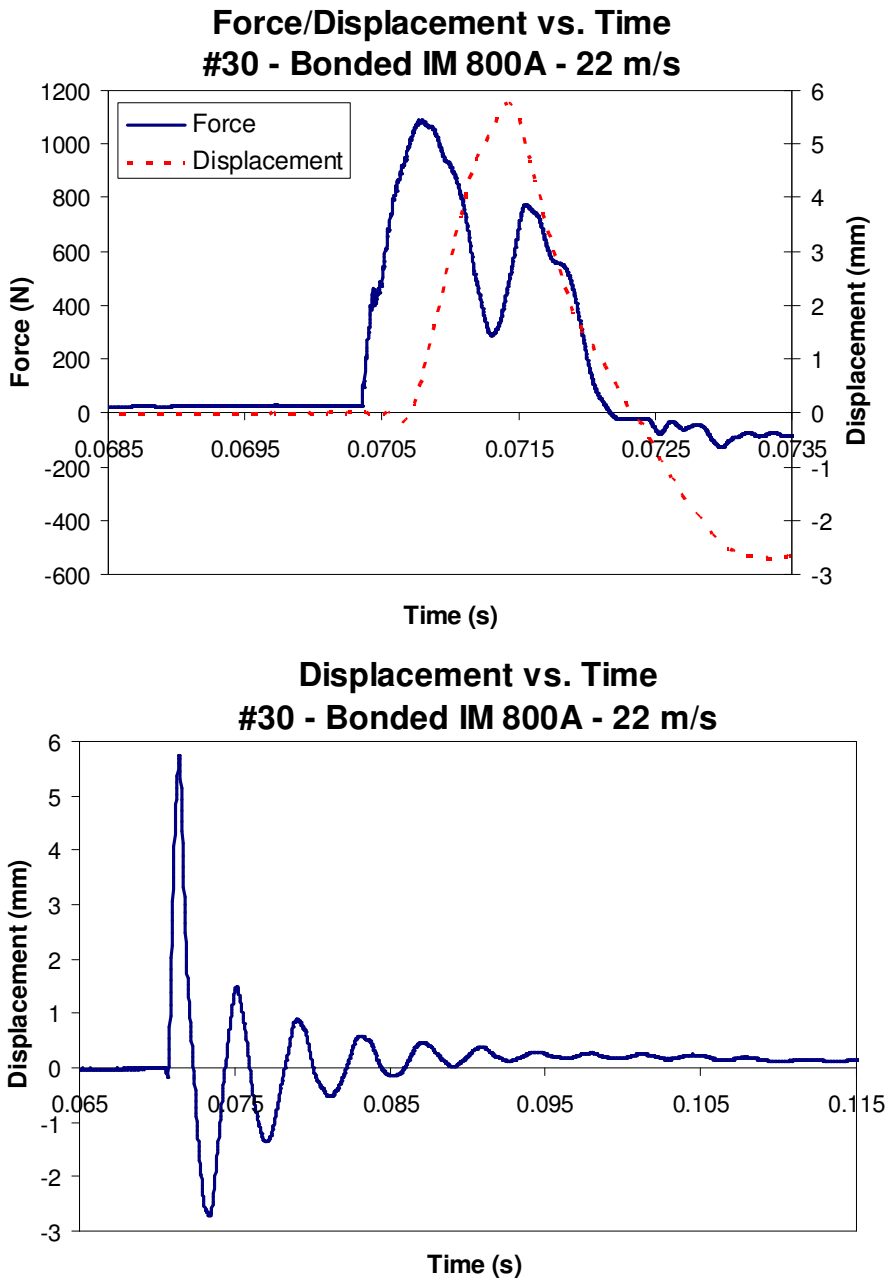

Figure 5.1.7 Impact force and displacement data for bonded TPU multi-laminates: a) 12 m/s DF A4700, b) 22 m/s DF A4700, c) 12 m/s IM 800A, and d) 22 m/s IM 800A

a)

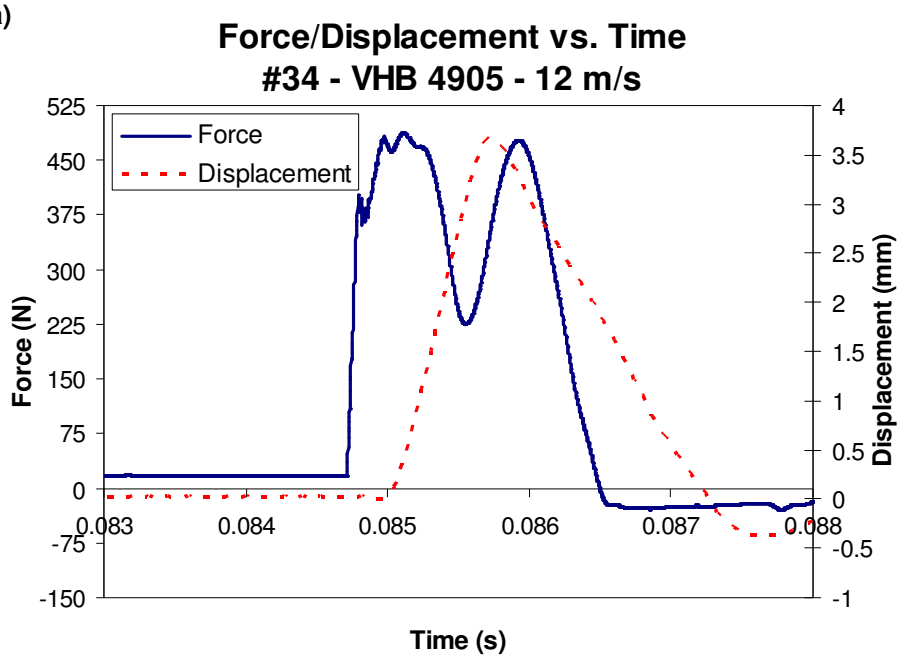
Force/Displacement vs. Time
#34 - VHB 4905 - 12 m/s
Force
Displacement
Force (N)
Displacement (mm)
Time (s)
525
450
375
300
225
150
75
0
-75
-150
4
3.5
3
2.5
2
1.5
1
0.5
0
-0.5
-1
0.083
0.084
0.085
0.086
0.087
0.088

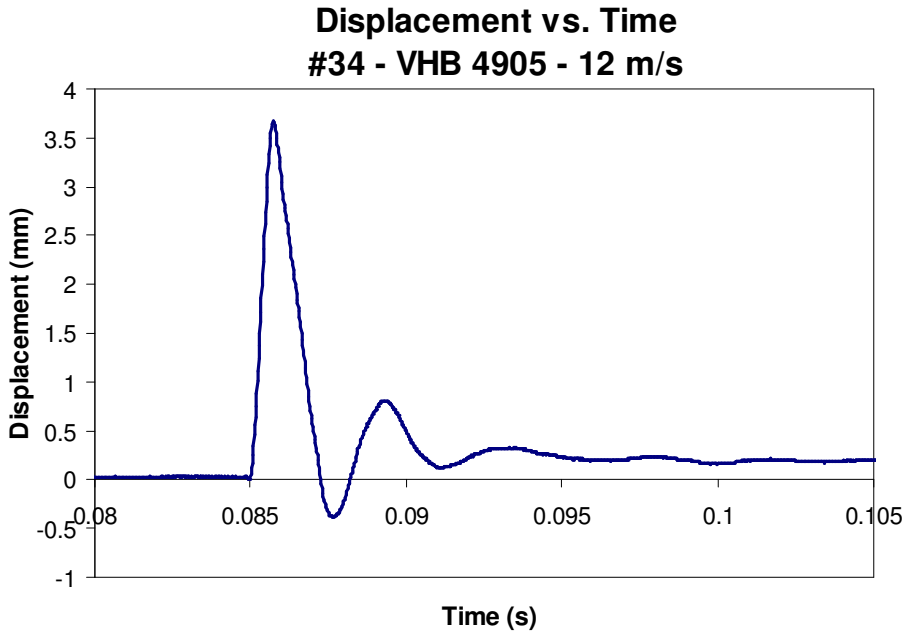
Displacement vs. Time
#34 - VHB 4905 - 12 m/s
Displacement (mm)
Time (s)
4
3.5
3
2.5
2
1.5
1
0.5
0
-0.5
-1
0.08
0.085
0.09
0.095
0.1
0.105

b)

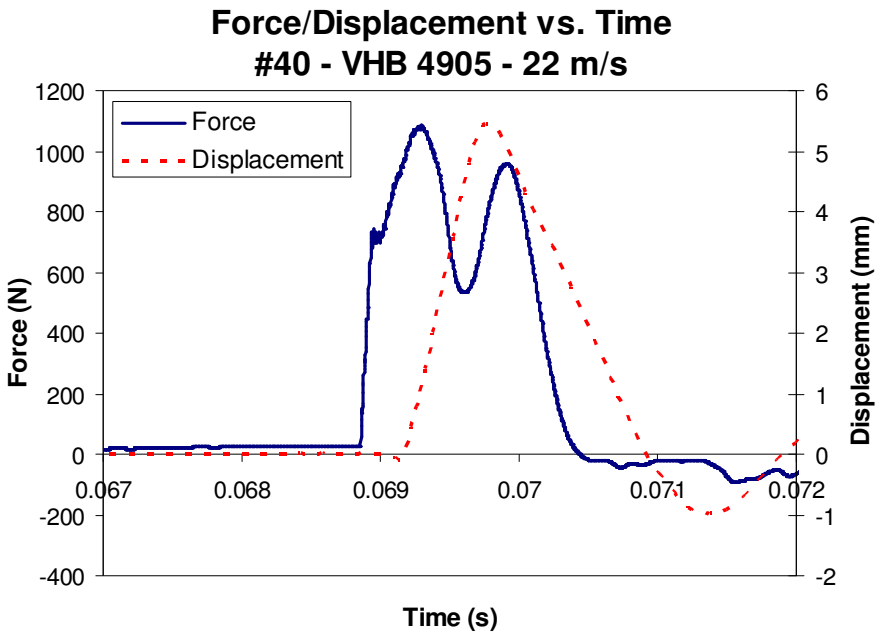
Force/Displacement vs. Time
#40 - VHB 4905 - 22 m/s
Force
Displacement
Force (N)
Displacement (mm)
Time (s)
1200
1000
800
600
400
200
0
-200
-400
6
5
4
3
2
1
0
-1
-2
0.067
0.068
0.069
0.07
0.071
0.072

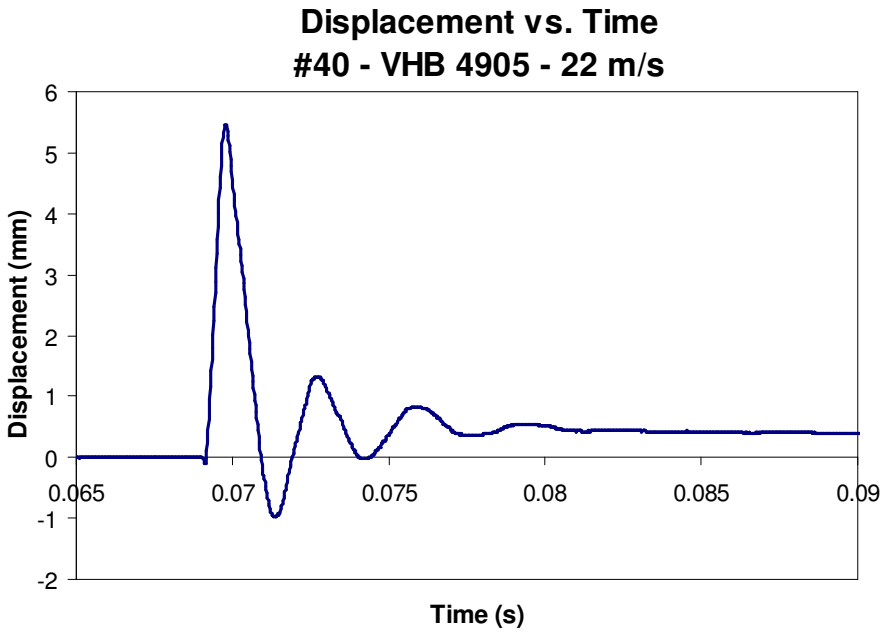
Displacement vs. Time
#40 - VHB 4905 - 22 m/s
Displacement (mm)
Time (s)
6
5
4
3
2
1
0
-1
-2
0.065
0.07
0.075
0.08
0.085
0.09

c)

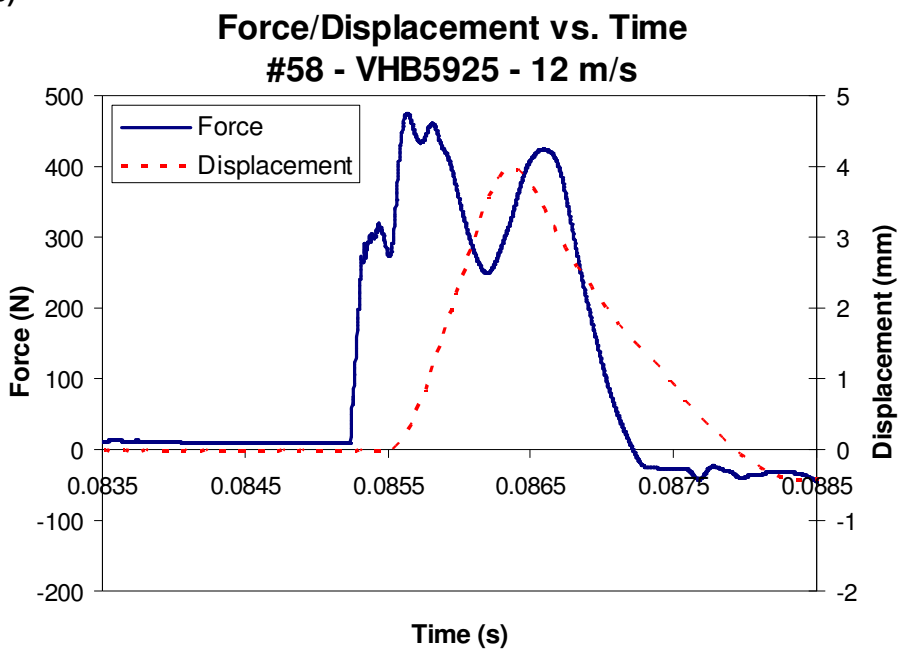
Force/Displacement vs. Time
#58 - VHB5925 - 12 m/s
Force
Displacement
Force (N)
Displacement (mm)
Time (s)
500
400
300
200
100
0
-100
-200
5
4
3
2
1
0
-1
-2
0.0835
0.0845
0.0855
0.0865
0.0875
0.0885

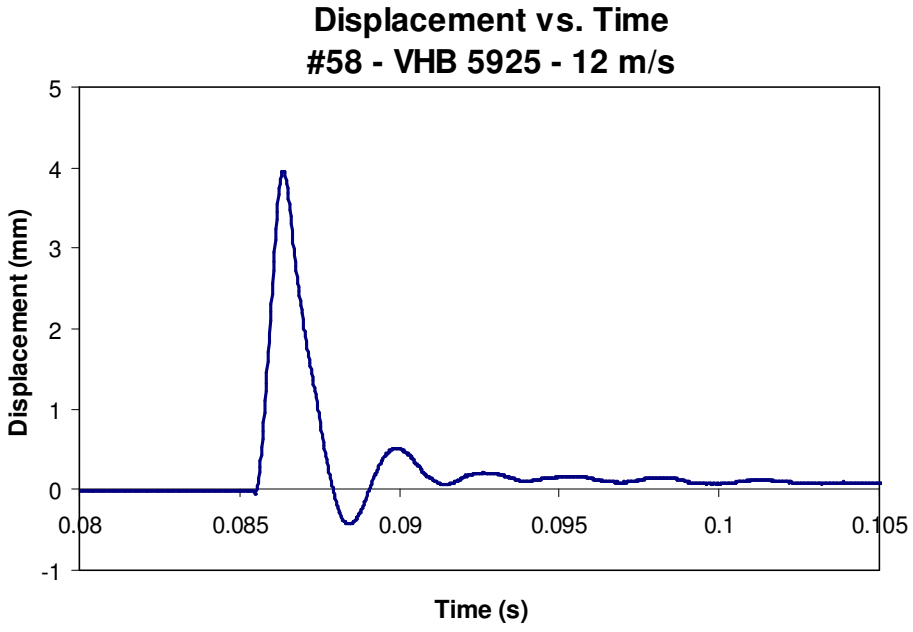
Displacement vs. Time
#58 - VHB 5925 - 12 m/s
Displacement (mm)
Time (s)
5
4
3
2
1
0
-1
0.08
0.085
0.09
0.095
0.1
0.105

d)

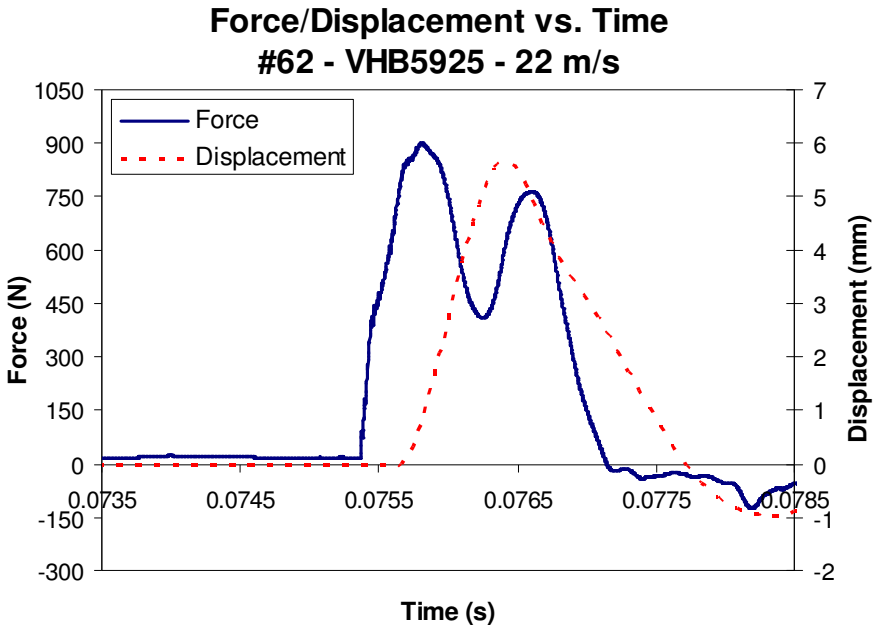
Force/Displacement vs. Time
#62 - VHB5925 - 22 m/s
Force
Displacement
Force (N)
Displacement (mm)
Time (s)
1050
900
750
600
450
300
150
0
-150
-300
7
6
5
4
3
2
1
0
-1
-2
0.0735
0.0745
0.0755
0.0765
0.0775
0.0785

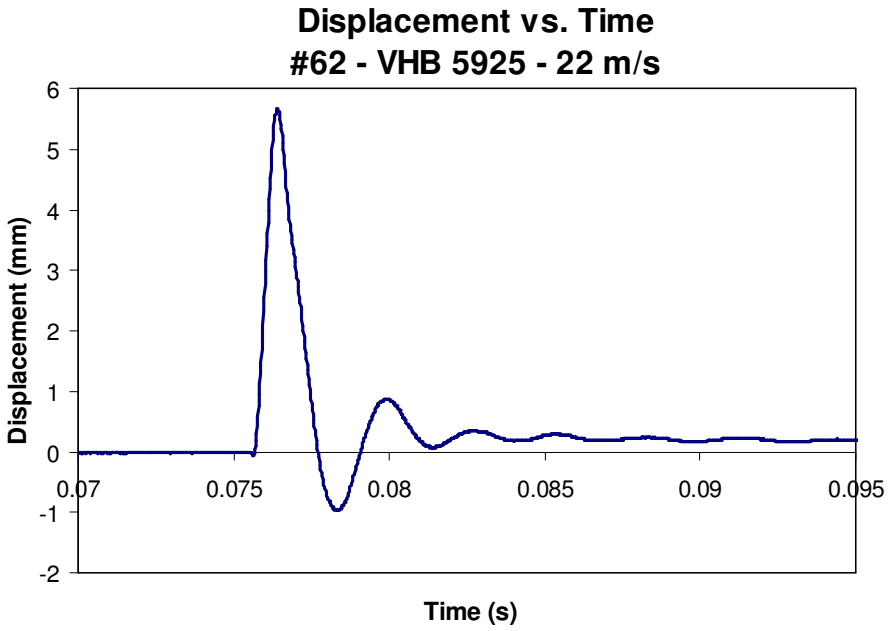
Displacement vs. Time
#62 - VHB 5925 - 22 m/s
Displacement (mm)
Time (s)
6
5
4
3
2
1
0
-1
-2
0.07
0.075
0.08
0.085
0.09
0.095

e)

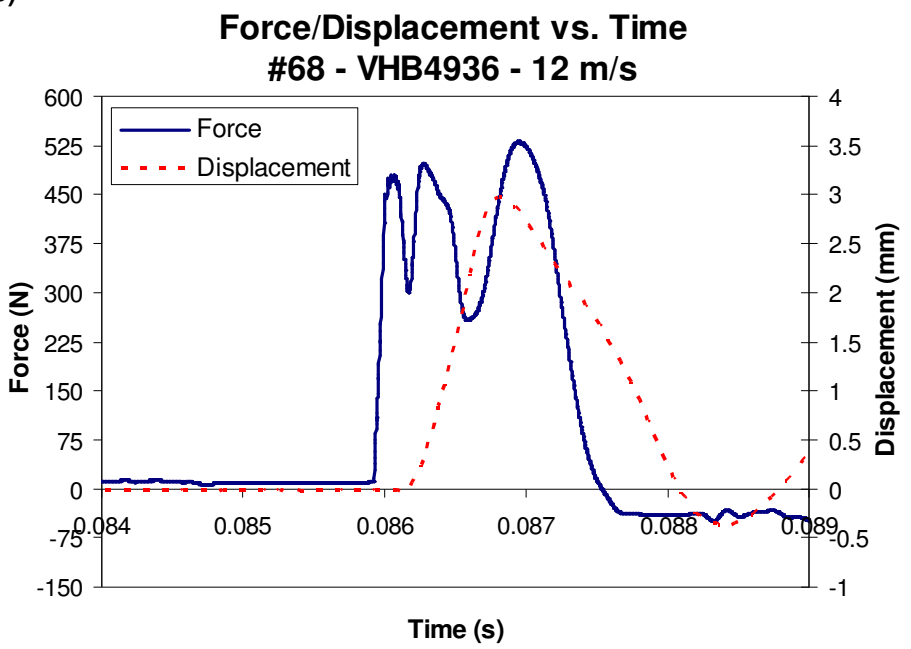
Force/Displacement vs. Time
#68 - VHB4936 - 12 m/s
Force
Displacement
Force (N)
Displacement (mm)
Time (s)
600
525
450
375
300
225
150
75
0
-75
-150
4
3.5
3
2.5
2
1.5
1
0.5
0
-0.5
-1
0.084
0.085
0.086
0.087
0.088
0.089

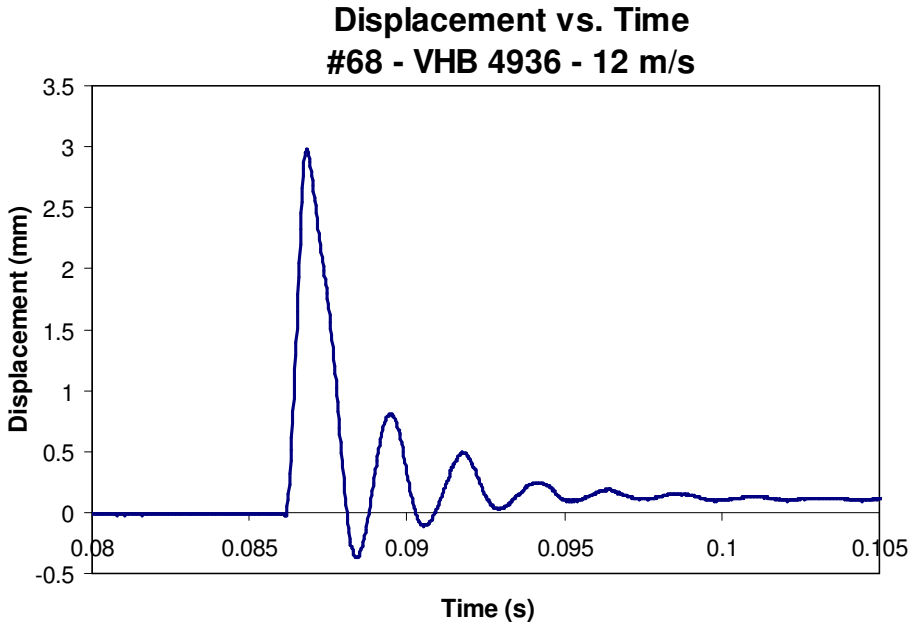
Displacement vs. Time
#68 - VHB 4936 - 12 m/s
Displacement (mm)
Time (s)
3.5
3
2.5
2
1.5
1
0.5
0
-0.5
0.08
0.085
0.09
0.095
0.1
0.105

f)

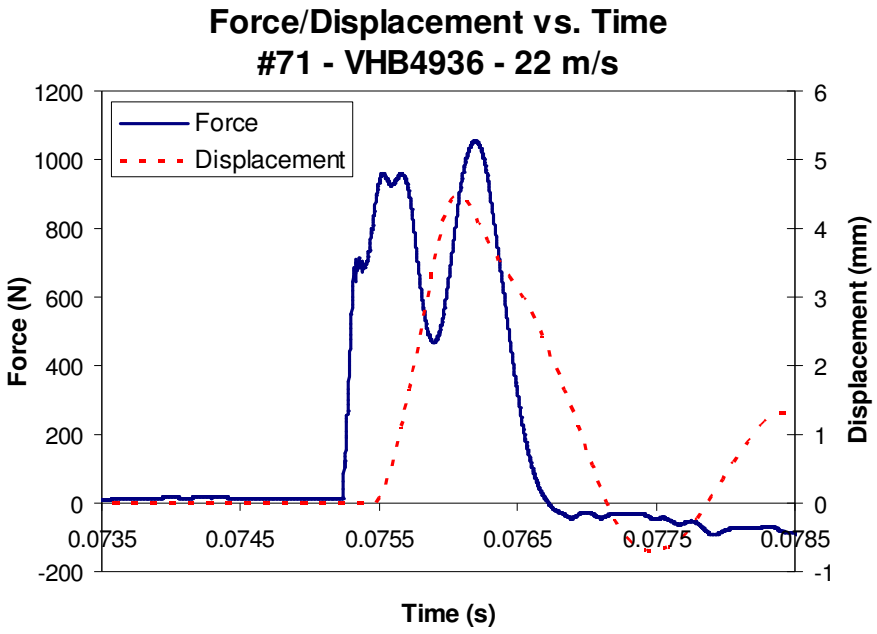
Force/Displacement vs. Time
#71 - VHB4936 - 22 m/s
Force
Displacement
Force (N)
Displacement (mm)
Time (s)
1200
1000
800
600
400
200
0
-200
6
5
4
3
2
1
0
-1
0.0735
0.0745
0.0755
0.0765
0.0775
0.0785

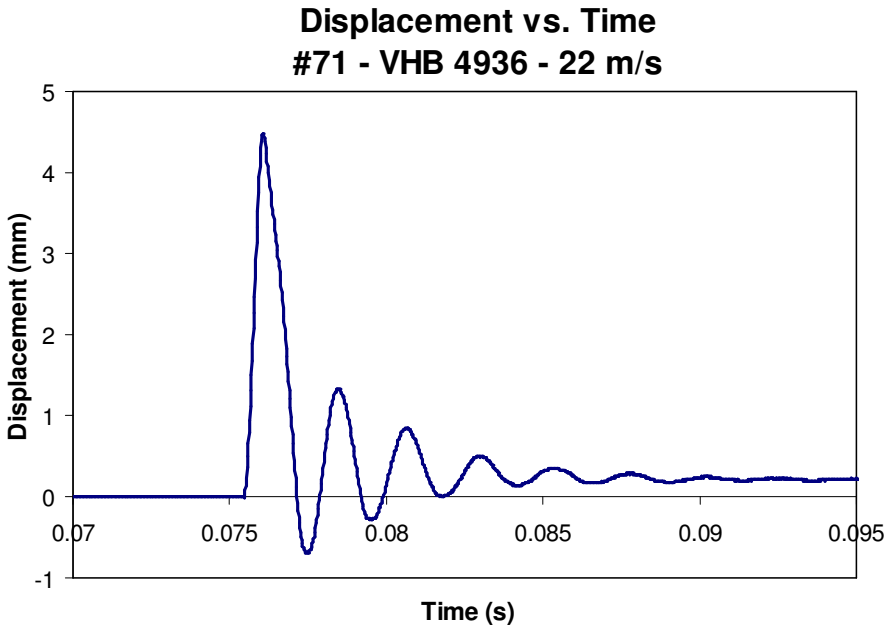
Displacement vs. Time
#71 - VHB 4936 - 22 m/s
Displacement (mm)
Time (s)
5
4
3
2
1
0
-1
0.07
0.075
0.08
0.085
0.09
0.095

g)

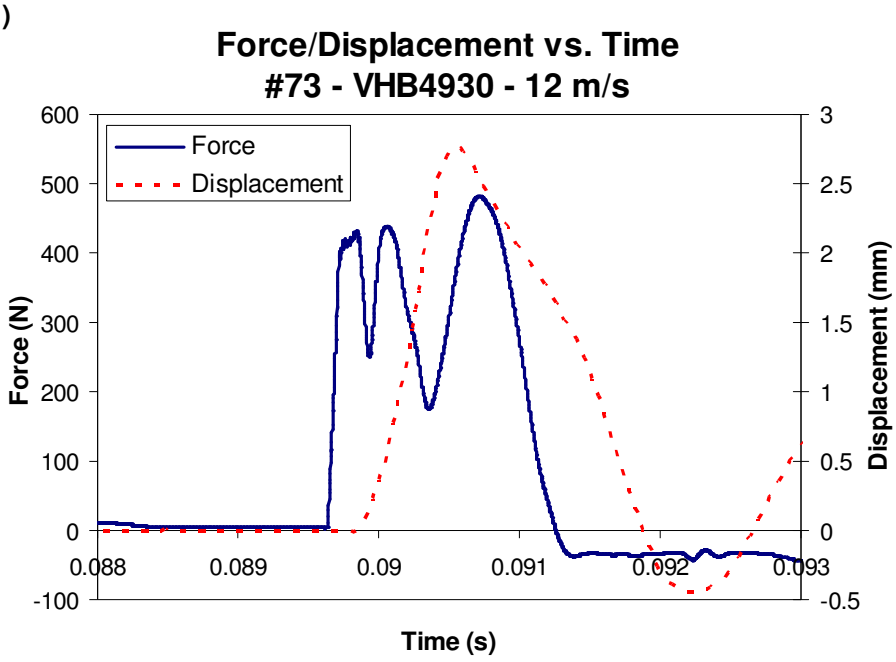
Force/Displacement vs. Time
#73 - VHB4930 - 12 m/s
Force
Displacement
Force (N)
Displacement (mm)
Time (s)
600
500
400
300
200
100
0
-100
3
2.5
2
1.5
1
0.5
0
-0.5
0.088
0.089
0.09
0.091
0.092
0.093

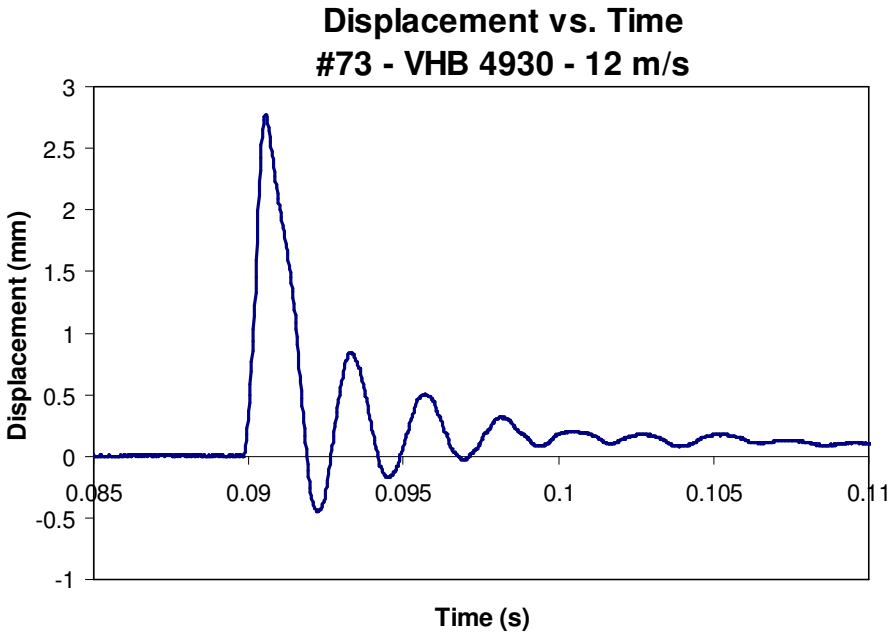
Displacement vs. Time
#73 - VHB 4930 - 12 m/s
Displacement (mm)
Time (s)
3
2.5
2
1.5
1
0.5
0
-0.5
-1
0.085
0.09
0.095
0.1
0.105
0.11

h)

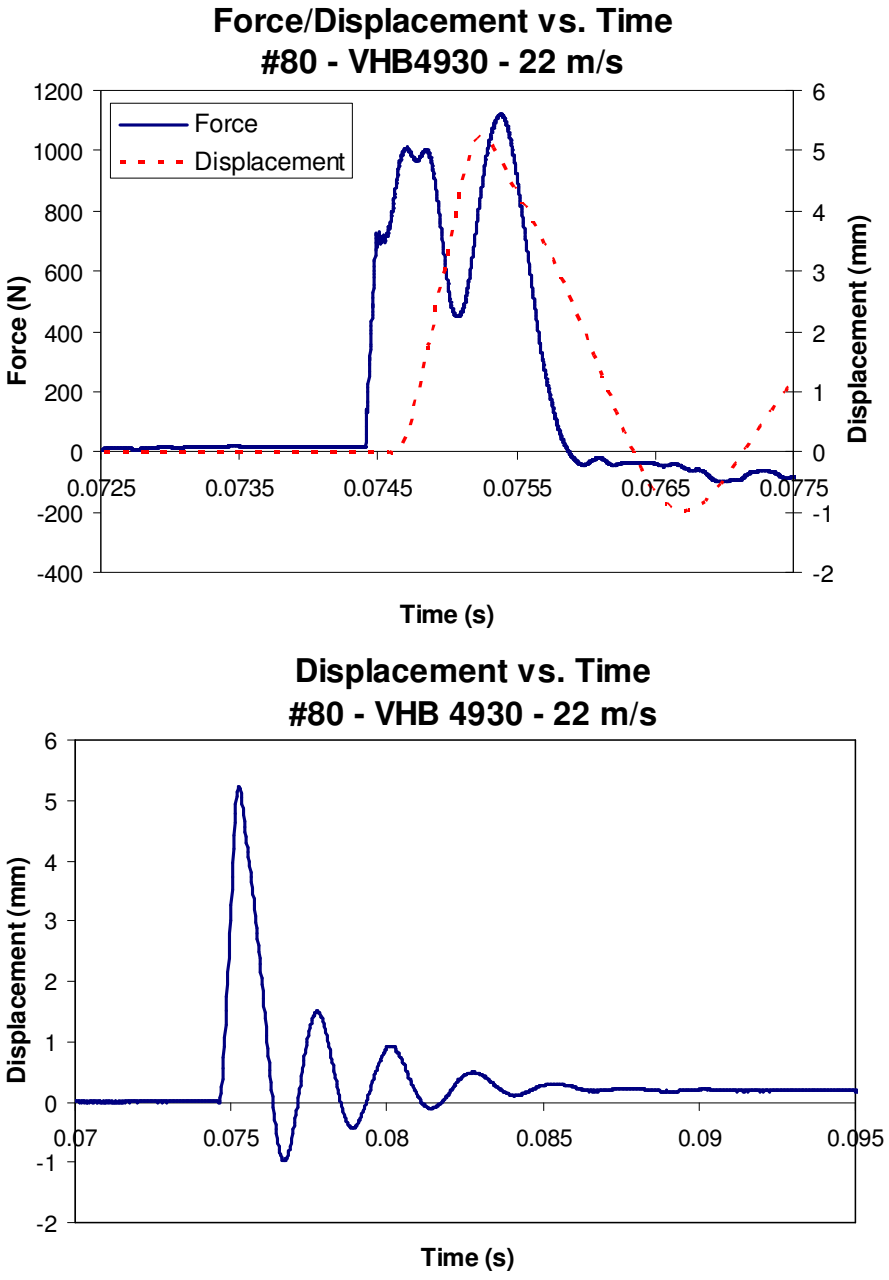

Figure 5.1.8 Impact force and displacement data for VHB polyacrylate multi-laminates: a) 12 m/s VHB 4905, b) 22m/s VHB 4905, c) 12 m/s VHB 5925, d) 22 m/s VHB 5925, e) 12 m/s VHB 4936, f) 22 m/s VHB 4936, g) 12 m/s VHB 4930, and h) 22 m/s VHB 4930

5.2 Energy Absorption/Dissipation Mechanisms

The impact energy incident on the multi-laminates is approximately 2 J for an impact velocity of 12 m/s and 7 J for an impact velocity of 22 m/s and impactor mass of 28.5 g. This energy can be dissipated/converted as a combination of: elastic energy (vibrational), plastic energy, and fracture energy. For the transformation of the incident mechanical energy we neglect effects of heat and sound produced by the impact, whereby these effects account for only a small fraction of the total energy of the process. Mechanisms to absorb the impact energy are dependent on system material properties, adhesion characteristics and boundary conditions, as well as other parameters such as impactor head shape (hemi-spherical, conical, flat-headed, etc.) and impactor eccentricity, and angle during loading. These factors are inherent in the experimental setup geometry, specimen configuration, and impact velocity. In this research, the effect of normal impact of a hemi-spherical impactor on the multi-laminate is the primary focus.

Two parameters that are constant for all testing conditions are the relative area and mass ratios. The ratio of panel area exposed (161.29 cm^2) to cross-sectional impactor area (0.81 cm^2) is 200 and the total multi-laminate mass (~95 g) with respect to impactor mass (28.5 g) is approximately 3.3. A ratio that slightly varies for testing conditions is the relationship between the span of the specimen to the through thickness. The span of the multi-layered polymers, after being clamped, is 12.7 cm, while the thickness ranges from 3.175–3.81 mm for the various specimen configurations. Note that all interlayers are 0.635 mm thick except for VHB 4905 which is 0.5 mm. Therefore, the span to thickness ratio ranges from 33.3–40. In summary of this study, a relatively small diameter, lightweight impactor is incident on a large, thin multi-layered sample. As shown in Figures 5.1.5, 5.1.6, and 5.1.7, the combination of these parameters causes large elastic deflection to be a main component of the impact response, with maximum off-center displacements ranging from 3–6 mm for 12 m/s impacts and 4.5–8 mm for 22 m/s impacts. Changing any of the parameters stated above affects which energy absorption methods are realized and are dominant/secondary. For example, if the mass of the impactor or impact velocity was greatly increased, complete perforation with little deflection may occur. Based on the specific specimen geometry, bonding conditions, and experimental setup capabilities, combinations of elastic energy, plastic energy, and fracture mechanisms will occur

corresponding to a measure of impact performance. The following sections will analyze how each variable considered during testing affected the observed fracture and energy absorption mechanisms. Damage mechanisms that were characteristic of the configurations studied include: local fracture at the impact site, delamination, global brittle fracture (petaling), local plastic flow, and barely visible impact damage (BVID).

5.2.1 Effect of Presence of Unbonded Interlayer

This section compares the fracture differences observed for a two-layered PMMA/PC multi-laminate without an interlayer to unbonded PMMA/TPU/PC samples discussed in Section 5.2.2. Without an interlayer, global fracture of PMMA occurs and the "petals" formed in the two-layered samples are not intact and completely dislodge from the PMMA during impact (Figure 5.2.1). Slight plugging and BVID, more pronounced than samples with an unbonded interlayer, is observed in the PC back panel for the PMMA/PC samples. Similar energy absorption mechanisms are observed for the unbonded PMMA/TPU/PC samples with the two-layered specimens showing more global fracture and complete catastrophic failure. Samples impacted at 12 m/s show similar fracture patterns, but to a lesser extent than the 22 m/s impacted PMMA/PC.

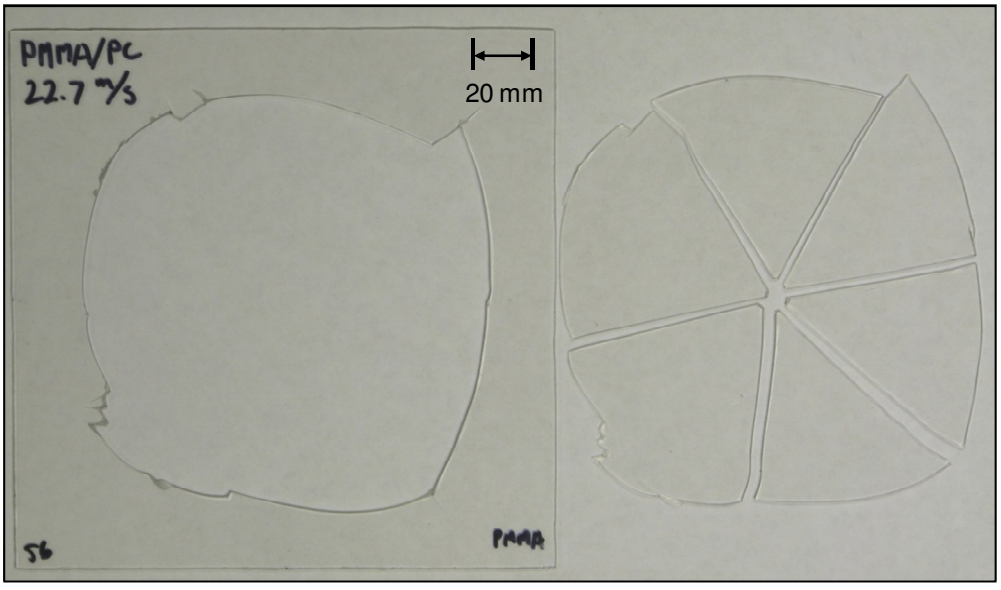

Figure 5.2.1 Fracture of two-layered PMMA/PC sample for impact velocity of 22 m/s

5.2.2 Effect of Interlayer Bonding

In this section, the effect on interlayer adhesion to the tough outerlayers is characterized in terms of bulk damage sustained to the overall panels. To probe these effects, configurations consisting of three-layer samples prior to adhesive curing are subjected to impact and the response is compared to fully joined (adhered) multi-laminates (Section 5.2.3). Since the polyacrylates are tacky at room temperature, unbonded samples could not be prepared. Figure 5.2.2 shows that, unlike bonded multi-laminates, unbonded interlayers sustain global fracture for 12 m/s and 22 m/s impacts, with less damage for the lower impact velocity (Figure 5.2.2a). All of the lower speed impacted samples have very similar fracture patterns showing various stages of the beginning of the large, circular crack but without many fully formed "petals" seen in PMMA/PC (Figure 5.2.1). For 22 m/s impact, a large circular crack occurs with both intact and dislodged "petals" originating from the impact site. The unbonded PMMA/IM800A/PC sample pictured has more completely defined petals (Figure 5.2.2c) when compared to the unbonded PMMA/DFA4700/PC multi-layered polymer (Figure 5.2.2b). Note that increased fracture in the absence of a soft interlayer coincides with results found by Tasdemirci and Hall when comparing two- and three-layered unbonded layered samples [67]. The clean, sharp cracks initiating at the impact site are the edges of the "petals" characteristic of brittle fracture. A series of micrographs are obtained to better classify the local plastic flow seen in some areas along the global circular crack inner edge. Taking a section along the large circular fracture surface, Figure 5.2.3a–c shows the fracture surface (magnified 50 times) observed on a plane oblique to the sample and transverse plane (through the thickness) of the PMMA panel. See Figure 5.2.4 for a schematic illustrating this plane of fracture through the PMMA front layer. These observations are similar to the fracture surfaces observed in PMMA by Fleck, Stronge, and Liu when conducting shear response testing using a split Hopkinson torsion bar [26]. The orientation of the rivulets pictured is aligned radially from the impact site, and is observed for both intact and dislodged sections. On the opposite side of these fracture surfaces, embedded in the PMMA, a "feathered" pattern (magnified 100 times) is observed (Figures 5.2.3d, e). All of the micrographs indicate that PMMA behaves in a brittle manner at the impact site, indicated by the smooth cracks travelling from the center and observed local plastic flow bands. Note that this fracture pattern is specific to this boundary condition and loading rate. Unbonded three-layered samples show very similar

PMMA fracture patterns and no visible damage to the interlayer for either impact speed. Very slight damage to the PC back layer is observed at the higher impact velocity (BVID). For these samples, it can only be observed if the PC is held up to light and angled correctly or can be felt by grazing the surface.

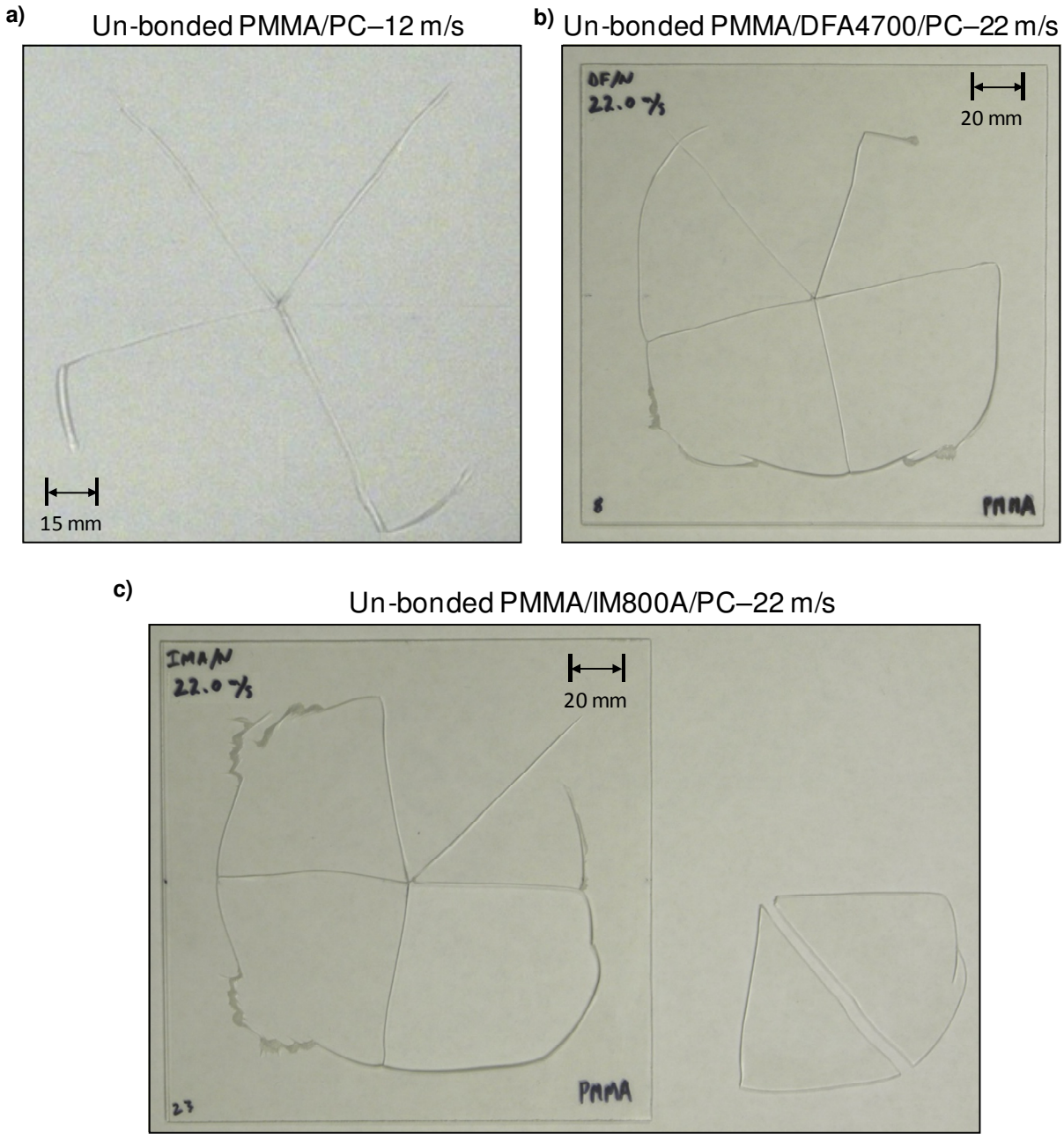

Figure 5.2.2 Fracture results for impact on unbonded: a) PMMA/PC with no interlayer–12 m/s, b) PMMA/DFA4700/PC–22 m/s, and c) PMMA/IM800A/PC–22 m/s

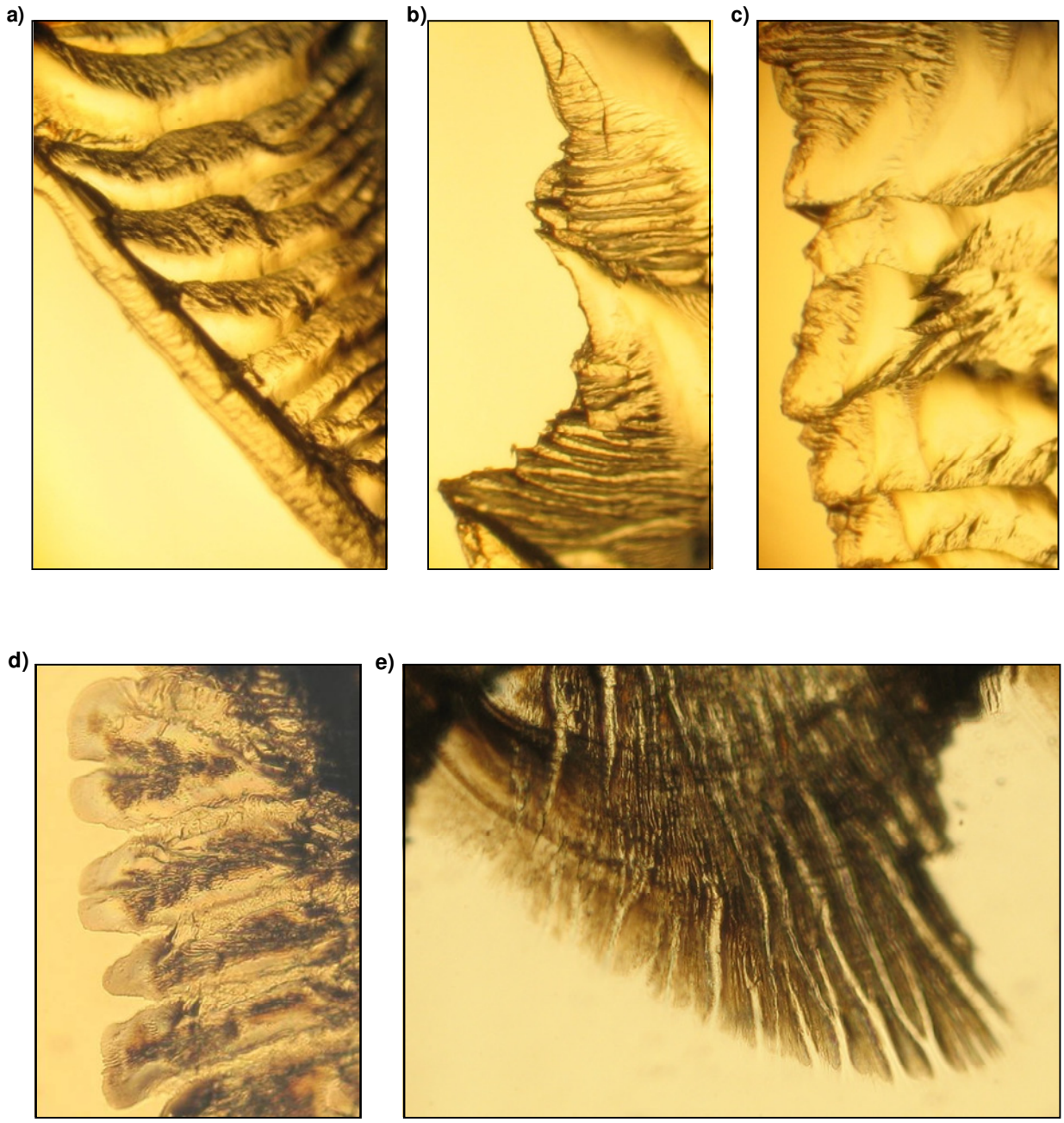

Figure 5.2.3 a–c) 50X zoom of PMMA "rivulet," local plastic deformation and d, e) 100X zoom of PMMA "feather" cracks

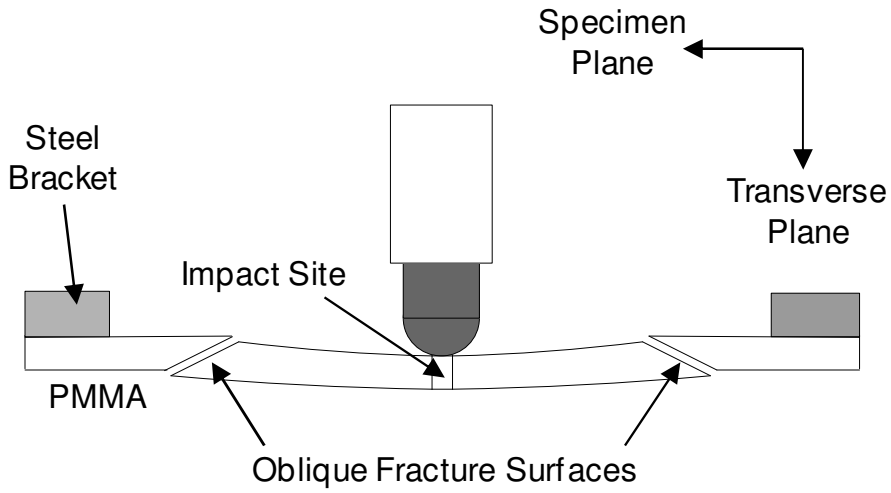

Figure 5.2.4 Schematic illustrating oblique fracture surface

5.2.3 Effect of Interlayer in Bonded Multi-Laminate

For impact velocities of 12 and 22 m/s, damage was considerably different for the six bonded multi-laminate configurations studied. Figures 5.2.5a–g shows the damage and fracture observed after impact with a representative summary of crack formation in Table 5.2. Note that this pattern is similar to that reported by Song and Hsieh for higher speed impacts (100 and 400 m/s) on monolithic PMMA with a central impact site and numerous, relatively equally spaced, radial cracks [8]. At those large impact speeds on the brittle PMMA, complete perforation occurred. Note the cracks observed in this research are solely in the PMMA front layer (intralayer) with no damage visibly detected in the interlayers or the PC back layer. Therefore, the soft interlayers and PC in the bonded multi-laminates deform entirely elastically during impact, except for very slight BVID in the back side of the PC outerlayer. For both impact speeds, the two interlayers that show the largest fracture area (crack lengths) are IM 800A and VHB 5925, with the least being DF A4700 (Table 5.2). With the impactor having a hemi-spherical surface acting on a planar section, most of the bonded samples impacted at 22 m/s show a slight local indentation at the impact site (except VHB 5925), approximately 5 mm in diameter. At the lower impact velocity, only radial cracking is present and this indentation isn't observed. This circular impact site damage conically disperses through the PMMA forming a larger diameter circle at the PMMA/adhesive interface. This conical shape of cracking at a PMMA impact site was also

observed by Rai and Singh. They conducted impact testing on multi-layered PMMA and soft adhesive samples with a drop tower testing machine [89]. It is also viewed that for the higher impact velocity both crack length and number are larger than the multi-laminates impacted at 12 m/s. Note that only two of the multi-laminates displayed delamination for impacts at 22 m/s, as shown in Figure 5.2.1c (VHB 4905) and Figure 5.2.1f (VHB 4930). As discussed previously, the microstructure of these two polyacrylates is observed to be incompressible acrylic without collapsible air gaps, facilitating delamination (Section 2.1). A representative for the 12 m/s impacted samples is shown in Figure 5.2.1g (VHB 5925). It is proposed that at the lower velocity, the soft interlayer modulates the impact whereas at the higher velocity, the interlayer behaves as a much stiffer material due to rate dependence. Only one picture is shown because all six bonded multi-laminates had very similar damage patterns, with 5 or 6 radial cracks of varying lengths that are very thin and difficult to photograph. Note that the relatively equally spaced radial cracks observed in the PMMA front layer for all configurations and impact speeds is a result of the fixed boundary condition of the specimens.

Table 5.2 Fracture summary for representative bonded samples impacted at 12 and 22 m/s

Impact Velocity (m/s)	Interlayer	Impact Site Diameter (mm)	Crack Length Range (mm)	Number of Radial Cracks
12	**DFA4700**	N/A	4 – 7	5
	IM800A	N/A	14 – 17	5
	VHB4905	N/A	9 – 11	5
	VHB5925	N/A	17 – 25	5
	VHB4936	N/A	9 – 12	6
	VHB4930	N/A	10 – 13	6
22	**DFA4700**	5	11 – 12	7
	IM800A	5	22 – 28	6
	VHB4905	5	17 – 22	7
	VHB5925	2	31 – 36	6
	VHB4936	5	11 – 17	9
	VHB4930	5–10	9 - 25	9

a) Bonded PMMA/DFA4700/PC–22 m/s

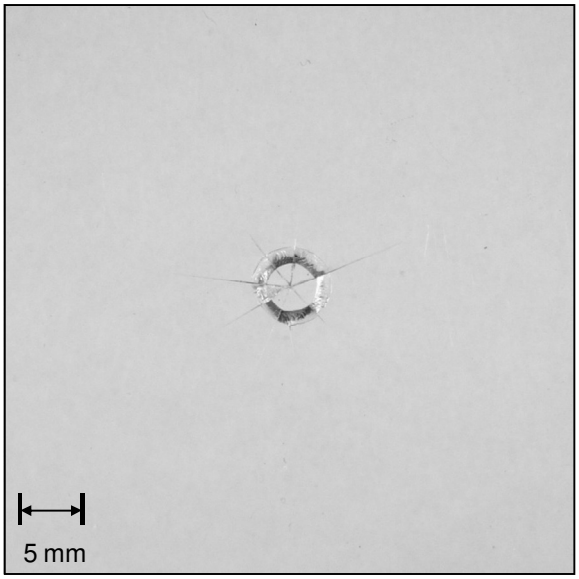

b) Bonded PMMA/IM800A/PC–22 m/s

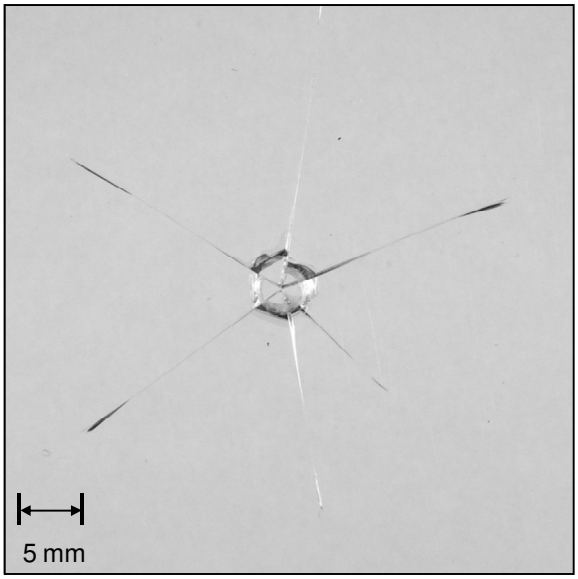

c) Bonded PMMA/VHB4905/PC–22 m/s

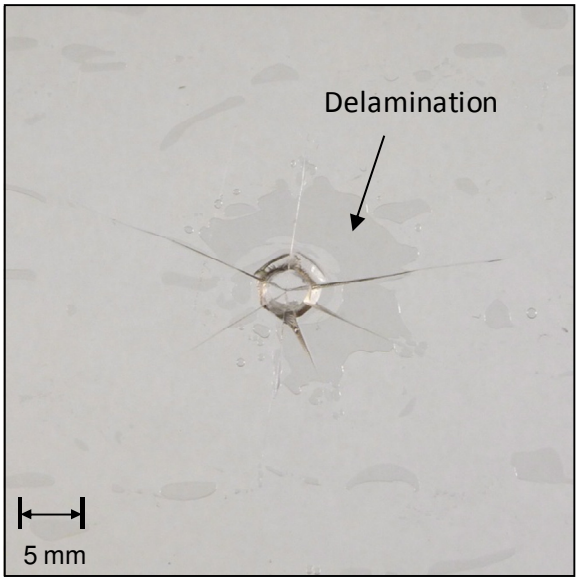

d) Bonded PMMA/VHB5925/PC–22 m/s

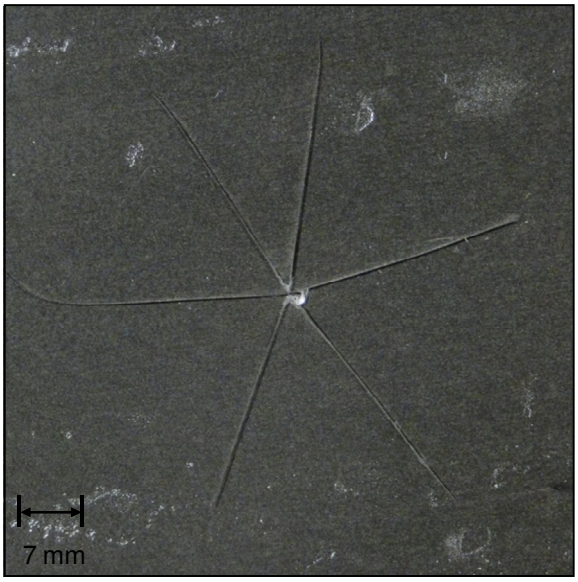

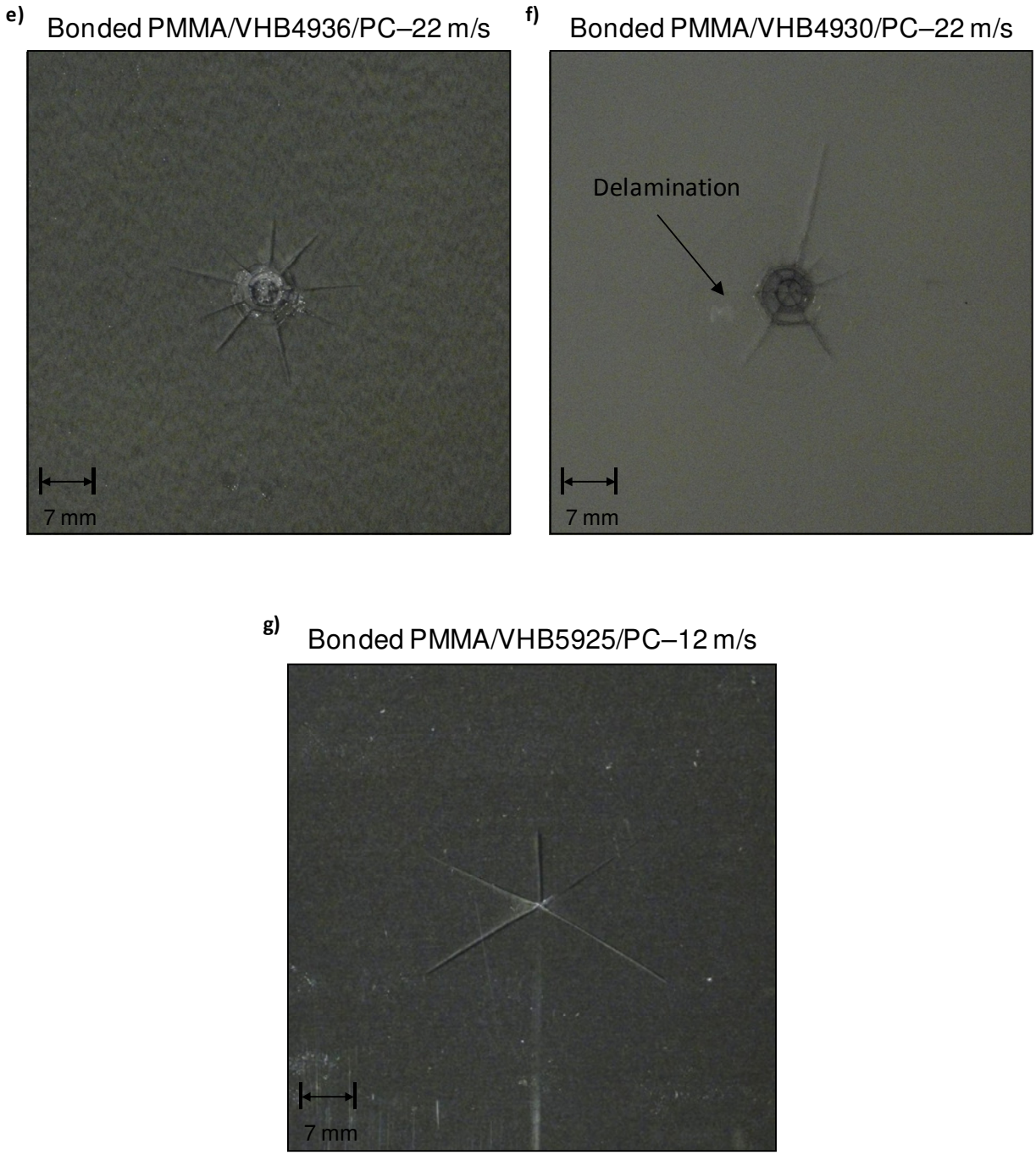

Figure 5.2.5 Fracture results for 22 m/s impact on bonded: a) PMMA/DFA4700/PC, b) PMMA/IM800A/PC, c) PMMA/VHB4905/PC (with delamination), d) PMMA/VHB5925/PC, e) PMMA/VHB4936/PC, and f) PMMA/VHB4930/PC (with delamination) and g) 12 m/s impact on bonded PMMA/VHB5925/PC

Chapter 6

Discussion of Impact Testing Results

The mechanical characterization of two TPUs and four polyacrylate elastomer interlayer materials was outlined in Chapter 2. The experimental results for the force and displacement traces recorded during impact for two impact speeds (12 and 22 m/s) on three-layer multi-laminates, as well as the post-impact fracture analysis were presented in Chapter 5. In this chapter, the evolution of the mechanical response of the interlayers is discussed. Specifically, how the rate-dependent properties and high damping behavior at lower rates is used to assess the impact performance at higher rates.

Ten quantitative metrics are obtained from both force and displacement traces recorded during impact (Chapter 5). Contact force metrics include: first and second force peaks, loading rate, local minimum force, loading pulsewidth, and loading impulse. Displacement metrics include: maximum displacement, transient response frequency, 2% settling time, and decay rate. Metric values reported are averages of three tests for each configuration and impact speed. Note that the error for metrics given is approximately ±5–10% (depending on the metric). As shown in Figure 6.1, configurations tested include unbonded two-layered PMMA/PC and three-layered PMMA/TPU/PC (two interlayers), and bonded three-layered PMMA/adhesive/PC (six adhesives). In total, 54 multi-laminates are impacted with a complete summary of all numerical metric results in Appendix C.1. The analysis below explains how the metrics correspond to the impact mechanics, such as deformation behavior, energy absorption, and fracture mechanisms. In actuality, one quantitative metric cannot give insight into, or completely characterize, impact performance. A combination of multiple metric analyses and qualitative observation techniques are used to gain insight into why an interlayer may have superior or inferior impact performance over another. Figure 6.2 shows the methods for measuring the ten recorded force and displacement metrics on representative traces. Metric results are given in Figures 6.1.1, 6.1.2, 6.1.3, 6.2.1, 6.2.2, and 6.2.3 with individual metric error percentages calculated by the maximum deviation of the three data points from their average. Post-impact fracture results are correlated

to metric trends. A summary of average crack lengths observed in bonded multi-laminates for impact speeds of 12 m/s and 22 m/s is given in Figure 6.3. For both impact speeds, the order of increasing average crack length by interlayer is: DF A4700, VHB 4936, VHB 4905/VHB 4930, IM 800A, and VHB 5925. Note that results and trends for the unbonded multi-laminates are not as consistent for both impact velocities as the bonded samples due to the smoothing of force and displacement traces with substantially more fracture-related outliers.

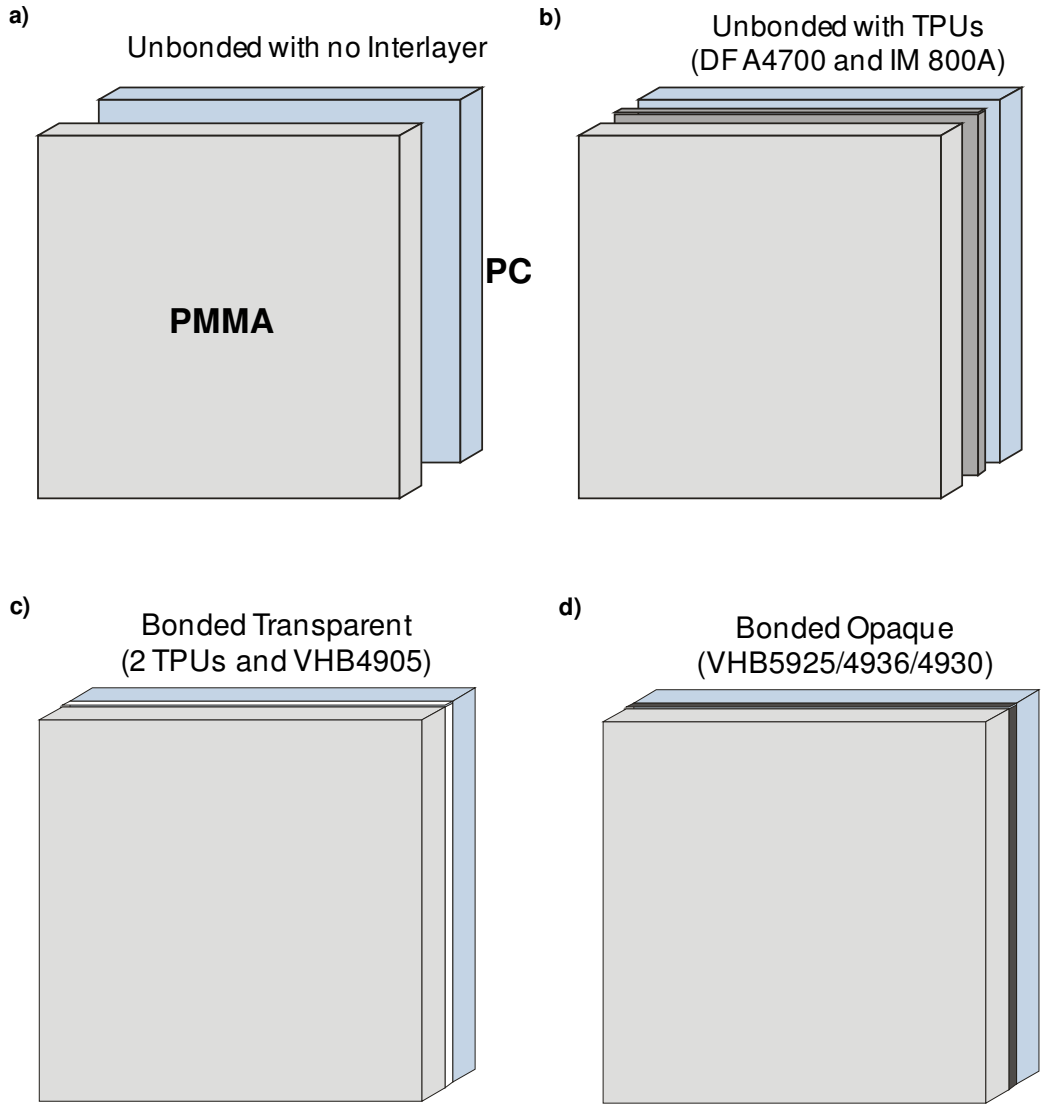

Figure 6.1 Multi-laminate configuration summary: a) two–layer unbonded (PMMA/PC), b) three–layer unbonded (PMMA/TPUs/PC), c) three–layer bonded (PMMA/transparent adhesive/PC), and d) three–layer bonded (PMMA/opaque adhesive/PC)

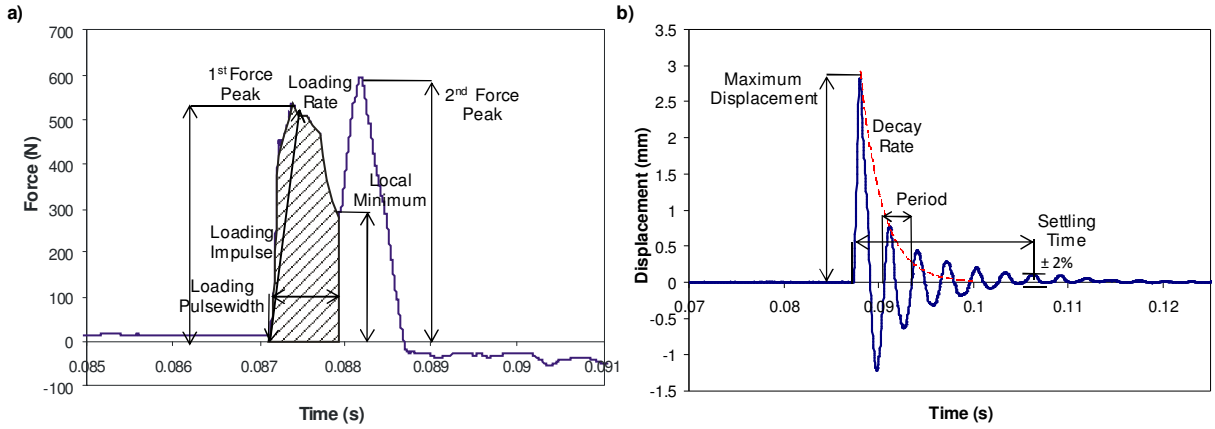

Figure 6.2 Quantitative metrics measured from a) force and b) displacement signals

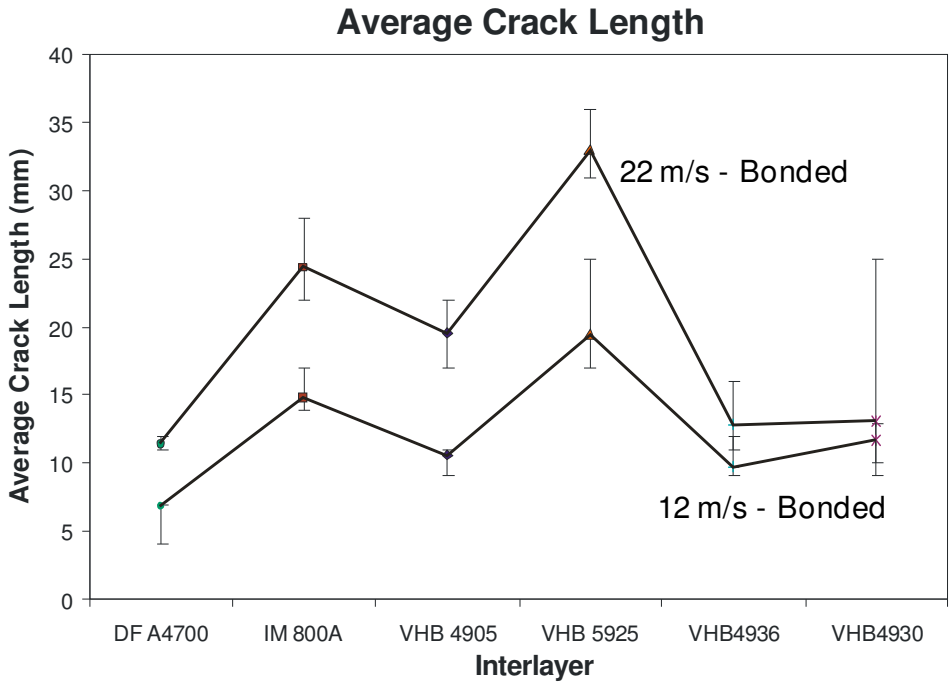

Figure 6.3 Summary of average crack length for representative bonded multi-laminates with error bars representing the range of crack lengths for the given sample

6.1 Quantitative Contact Force Metrics

6.1.1 First Force Peak and Loading Rate

Contact force at the impact site is recorded using a shock accelerometer embedded in a steel impactor. The first force peak is measured as the maximum value during the loading of the multi-laminate (Figure 6.1.1a). As expected, this metric is larger for the higher impact speed and bonded boundary condition. Bonding of the outerlayers results in increased interfacial shear strength and resistance to transverse deflection. The initial response of the sample is heavily influenced by the glassy polymer outerlayers PMMA and PC and is determined by the effective stiffness. This is further reflected in the measured loading rate (Figure 6.1.1b). Loading rate is representative of the magnitude and time to reach the first force peak. Loading rate follows the same trend as the first force peak. Loading rates are larger for samples impacted at 22 m/s than 12 m/s and unbonded samples have smaller loading rates than bonded for an impact velocity. The order of first force peaks and loading rate, in ascending order, is somewhat correlated to the interlayer quasi-static compressive compliance order (from most to least compliant) of: VHB 5925, VHB 4905, VHB 4936, VHB 4930, IM 800A and DF A4700 for both impact velocities (Section 2.3.1).

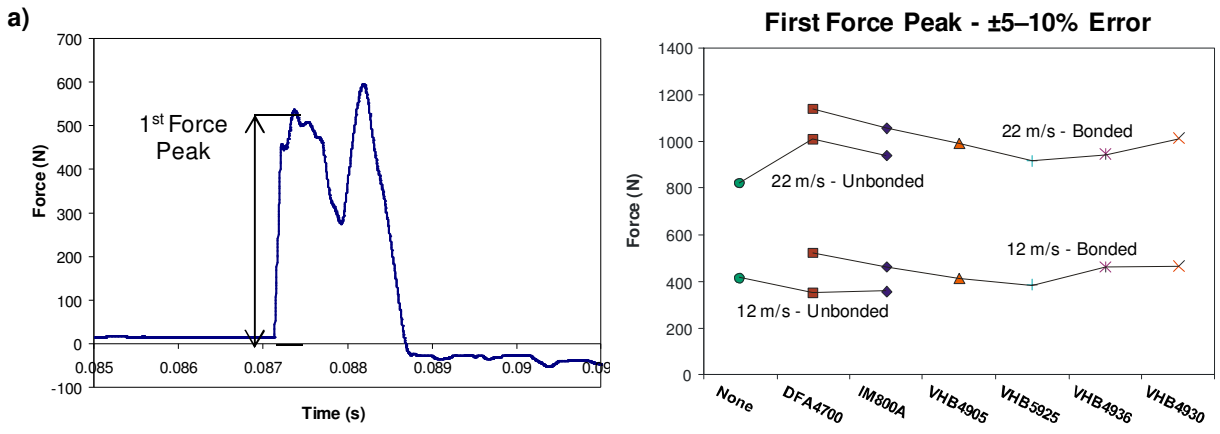

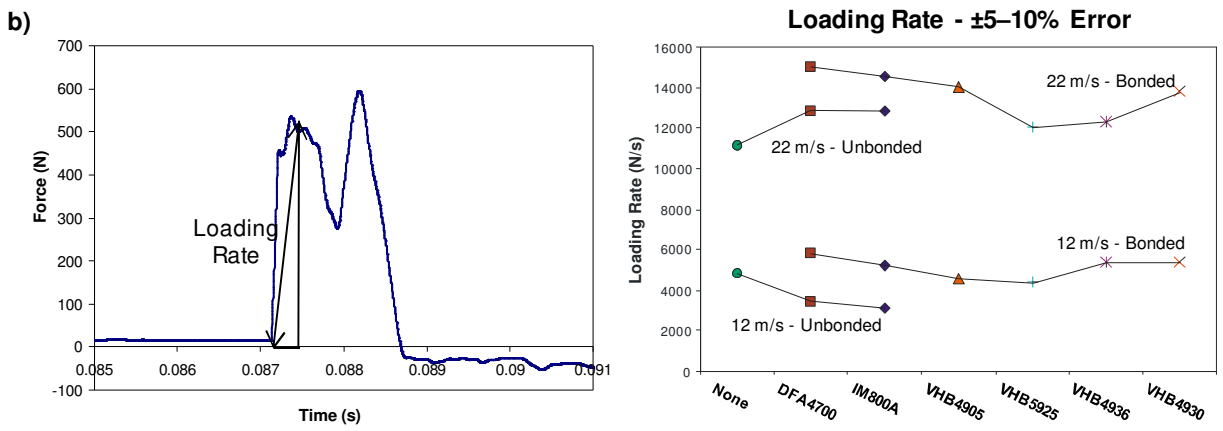

Figure 6.1.1 Metric results for a) first force peak and b) loading rate

6.1.2 Local Minimum Force, Second Force Peak, and Loading Pulsewidth

Local minimum force, second force peak and loading pulsewidth metric results all directly relate to the fracture (average crack lengths) and impact performance observed (Figure 6.3). It was discussed previously in Section 5.2.3 and shown in Table 5.2 that the bonded multi-laminates with IM 800A and VHB 5925 had the longest cracks for both impact velocities. Therefore, the trend observed is that the lowest local minimums and second force peaks, and the longest loading pulsewidths, correlate to the most damage (Figure 6.1.2). The second and local minimum force peaks characterize the amount of elastic energy the multi-laminate is capable of storing during loading to maximum deflection, and the transfer to kinetic energy of the sample reloading the impactor. A substantial second peak is indicative of the absorbed energy reloading the impactor, while a smaller second peak reflects more energy converted to fracture. This is confirmed by observed increase in fracture in the front PMMA outerlayer. For several bonded multi-laminates, the second is actually larger than the first force peak. This is observed for both impact speeds for three interlayers: DF A4700 (Figure 5.1.7a, b), VHB 4936 (Figure 5.1.8e, f), and VHB 4930 (Figure 5.1.8g, h).

The loading pulsewidth is measured from force initiation to the local minimum and is indicative of the time required to decelerate impactor motion and absorb impact energy. A longer pulsewidth is consistent with longer contact time between the impactor and the multi-laminate, as well as increased time for damage/fracture to initialize and for cracks to propagate. For both

impact velocities, it is clear that bonded multi-laminates with IM 800A and VHB 5925 had the longest times for loading (Figure 6.1.2c). For a given impact velocity, the multi-laminates able to decelerate the impactor the fastest have the least fracture. Note that loading pulsewidths are shorter for the higher impact speed, which is consistent for both bonded and unbonded boundary conditions. Confirming this, Garland and Rogers conducted low speed (less than 100 mm/s) instrumented pendulum impact testing on elastic, nonconforming samples and showed that impact duration decreased with increasing initial velocity [90]. Multi-laminates impacted at 22 m/s have loading rates 2.5–3 times greater than those impacted at 12 m/s for all configurations (Figure 6.1.1b). Large loading rates are indicative that the loading of the sample occurs significantly faster, with the impactor being in contact for less time.

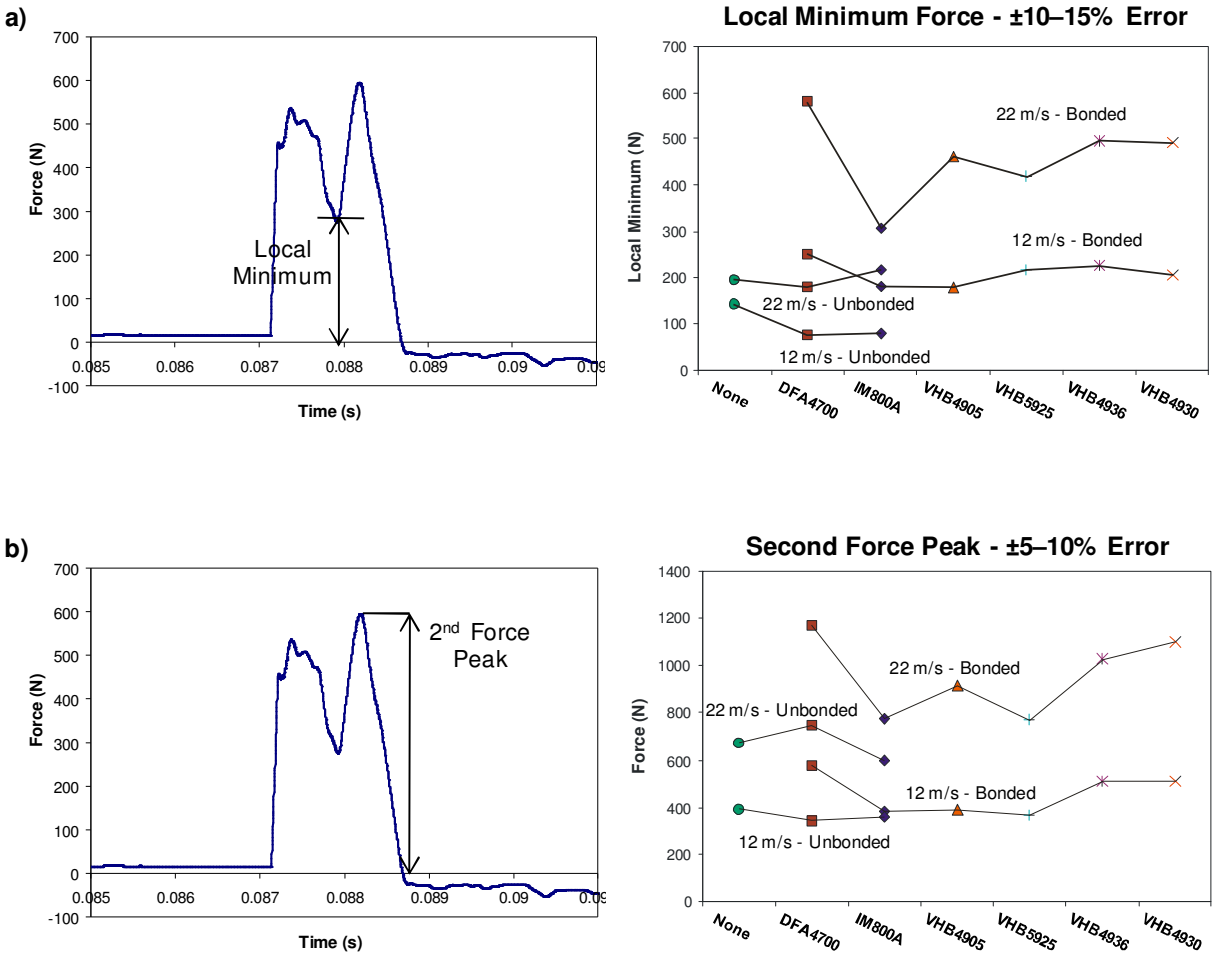

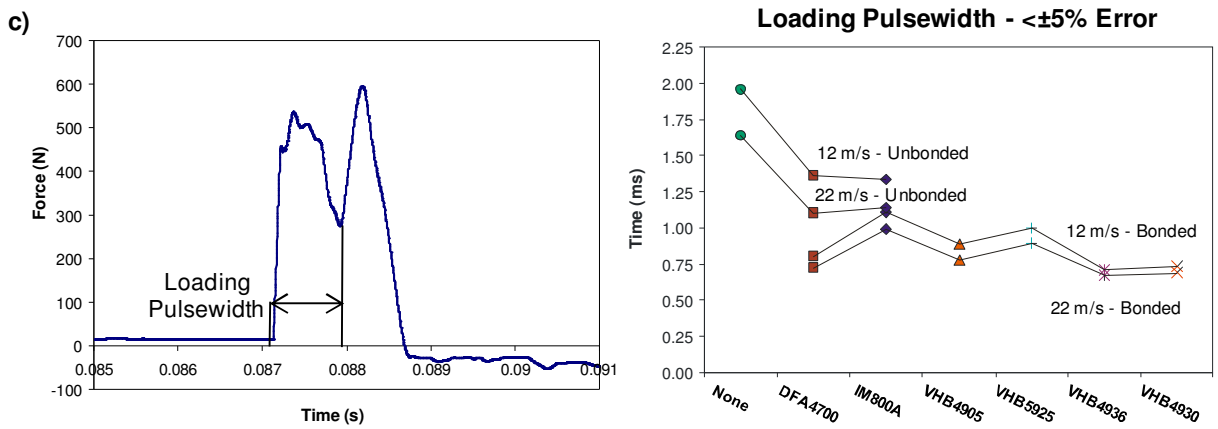

Figure 6.1.2 Metric results for a) local minimum force, b) second force peak, and c) loading pulsewidth

6.1.3 Loading Impulse

To truly characterize the impact load, impulses are calculated (areas under the force/time curve) and compared. Using the same Mathematica program for hysteresis loop area approximations (Appendix A.1), the area under the force curve is measured. With shorter contact times, but larger contact forces (or vice versa), impulse values may be similar for different interlayers. Although the interlayers resulting in the most damage don't have the two highest impulses, there is still a trend observed when separating the TPUs from the 3M polyacrylates. Although DF A4700 has a higher first force peak and loading rate than IM 800A for both impact speeds (Figure 6.1.1a), IM 800A has a larger impulse and so it follows, more fracture (Figure 6.1.3). Within the polyacrylate multi-laminates, VHB 5925 has the smallest first force peak and loading rate for both impact speeds (Figure 6.1.1a) but has the largest impulse and most PMMA fracture (Figure 6.1.3). Note that the impulse isn't measured for unbonded samples. This is due to increased noise in the raw data from fracture, such that accurate numerical approximations cannot be obtained.

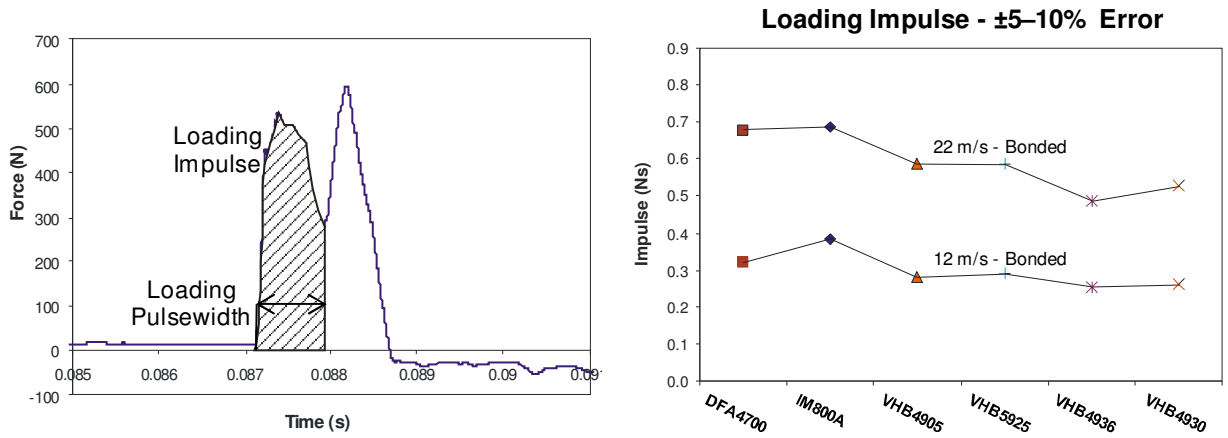

Figure 6.1.3 Loading impulse metric results

6.2 Quantitative Displacement Metrics

The experimental setup has two laser displacement sensors, symmetrically placed 28.575 mm (1.125 in) away from the impact site. Therefore, there are two sets of deflection data for each sample. As expected, they typically have very similar magnitudes (symmetric response), and either data set is used for metric measurements. In the case where severe PMMA cracking occurs (unbonded samples) and reflective tape is compromised, one or both optical sensors' data is disrupted. This data has many false readings and sometimes doesn't even detect the reflective surface. In this case, the signal with the least outliers, or a combination of both, is used for metric analysis.

6.2.1 Maximum Displacement

Maximum displacement is recorded as the first positive peak of the MTI sensor's data. As expected for all bonding conditions, it is observed that the multi-laminates deflect more at the higher impact velocity (Figure 6.2.1). This is true for this experimental setup's specific intermediate impact speeds, boundary conditions, and mass/area ratios discussed in Section 4.1.1. For example, if impact speed was greatly increased, there may not be any time for elastic deflection with complete sample perforation occurring. In this case, out-of-plane displacement would be minimal. In general for this impact testing, the greater the maximum out-of-plane

displacement of the multi-layered structure, the more likely that local/global deformation or fracture will occur. At these velocities (12 and 22 m/s), it has been shown that the more the panel deflects the worse the damage and impact performance. For the unbonded boundary condition, the two-layered PMMA/PC samples deflected more than the other unbonded three-layered multi-laminates for both impact speeds. As shown in Figure 5.2.1, the PMMA/PC samples had significantly more damage than the other unbonded samples (Figure 5.2.2). For both impact velocities, the IM 800A unbonded samples displace more than DF A4700, and show more fracture (Figure 5.2.2b, c). The trend observed for the bonded multi-laminates is the same as the loading pulsewidth, second force peak, and local minimum force in that the IM 800A and VHB 5925 samples are at extremes for both impact velocities. As shown in Table 5.2 and Figure 6.3, the bonded IM 800A and VHB 5925 multi-laminates have the longest cracks and fracture areas when compared to all the bonded multi-laminates.

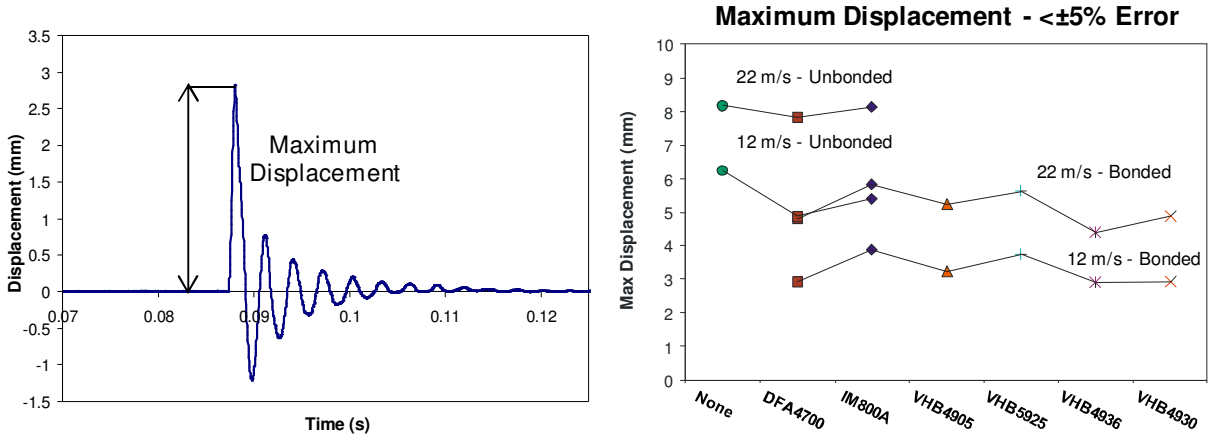

Figure 6.2.1 Maximum displacement metric results

6.2.2 Response Frequency

Three displacement metrics that are closely related to the sample's vibrational response following impact, and are indicative of the degree of damping of the specimens under high loading rates, are the: transient response frequency, 2% settling time, and decay rate. It is desirable to measure the transient response frequency because it is reflective of the effective stiffness and mass of the multi-layered structure. Since the specimen masses are all very similar,

the response frequency is mainly dependent on the "stiffness" of the multi-laminates. In general, the dissipation of impact energy as vibrational energy is considerable for systems with relatively low natural frequencies, as is the case here. Results in Figure 6.2.2 show that unbonded samples' response frequencies are very similar for all configurations and both impact velocities. These unbonded samples' frequencies (150–180 Hz) are substantially lower than the bonded samples (230–450 Hz). For the bonded multi-laminates, IM 800A has the lowest response frequency for both impact speeds with the least compliant VHB polyacrylates (VHB 4936 and VHB 4930) having the highest response frequencies. Since frequency is measured immediately after the impactor loses contact, response frequencies are indicative of the properties of the damaged panels and reflect the residual mechanical properties of the multi-laminate.

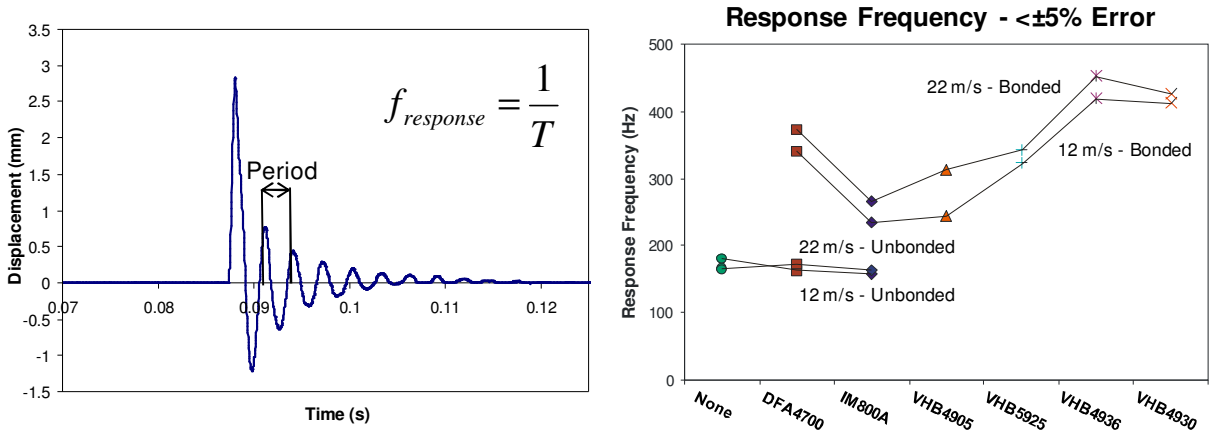

Figure 6.2.2 Response frequency metric results

6.2.3 Settling Time and Decay Rate

Another metric to be considered is the 2% settling time of the multi-layered polymers. This is measured as the time required for the displacement of the sample to be within ±2% of its final displacement. Occasionally this final value is not zero, especially in samples with more substantial fracture and cracking compromising the laser displacement sensors' reflective tape (Section 5.1.3). Unbonded samples have significantly longer settling times than bonded samples due to less effective damping, and possible self-excitation/vibration between layers. The interlayers with high response frequencies (Figure 6.2.2) have fast settling times. The four VHB

polyacrylates have such quick settling times (when compared to the TPUs) because of a high degree of damping (Figure 6.2.3a).

With further analysis of Figure 5.1.5 and Figure 5.1.6, it can be seen that the decrease in amplitude between the maximum displacement and next positive peak is relatively similar for all bonded multi-laminates for both impact speeds (70–88% decrease). This is inconsistent with response frequency and settling time metric analysis, which gives an indication of the vibrational response and damping of the sample. Therefore, the decay rate metric is introduced to characterize how quickly the multi-laminates dissipate energy during vibration. The decay rate is quantified by fitting a decaying exponential function to the first two positive peaks of the displacement traces for each interlayer and configuration, combining the time to decrease displacement and magnitude of this reduction. This method is shown on a representative displacement trace in Figure 6.2.3b. The equation of this function, of the form $X(t)=Ae^{-kt}$, allows comparison between multi-laminates using the decay rate constant (k). A large decay constant indicates faster attenuation of displacement amplitude, while a small decay constant signifies the opposite. When comparing Figures 6.2.2, 6.2.3a, and 6.2.3b, it follows that the samples with high response frequencies and fast settling times have large decay constants. Note that in general, the unbonded multi-laminates have lower decay constants than the bonded samples. For most of the configurations tested, the decay rate was measured to be larger for samples impacted at 22 m/s than 12 m/s. To clarify Figure 6.2.3b, the dashed line is for bonded 12 m/s with the solid line for bonded 22 m/s impacted samples. The two configurations where this is not the case are bonded PMMA/IM800A/PC and PMMA/VHB5925/PC, which are the samples with the most fracture for both impact speeds. The justification for this inconsistency can be linked to the tensile response of these two interlayers. As previously discussed in Section 2.2, and shown in Figure 2.2.1b and Figure 2.2.1d, IM 800A and VHB 5925 behave increasingly like pseudoelastic materials with increasing strain rate. These two materials show decreasing residual strains (more strain recovery) with increasing strain rate, which is different from the responses of the other four interlayers (Table 2.2). It is believed that this increased "elasticity" with strain rate results in the anomaly seen in the decay rate metric. If the adhesive behaves more elastically at the higher impact speed, then the attenuation of the multi-laminate's displacement amplitude would lessen. Referencing the rate dependent tensile results, IM 800A is substantially more

pseudoelastic than any of the other interlayers (Figure 2.2.1). VHB 5925 has a similar tensile response as the remaining interlayers with substantial relative increase in hysteresis loop area with strain rate (Table 2.3), but like IM 800A, decreasing residual strain with increasing strain rate. Between impact speeds of 12 and 22 m/s, there is a substantial difference between the decay rates of IM 800A, while the difference for VHB 5925 is relatively small. Note that the switching of metric amplitude order with impact velocity is not observed for the other related vibrational metrics: response frequency and 2% settling time. It is observed for 2% settling time and decay rate metrics that the two samples with the most fracture for both impact velocities (IM 800A and VHB 5925) are the maximum and minimum values measured.

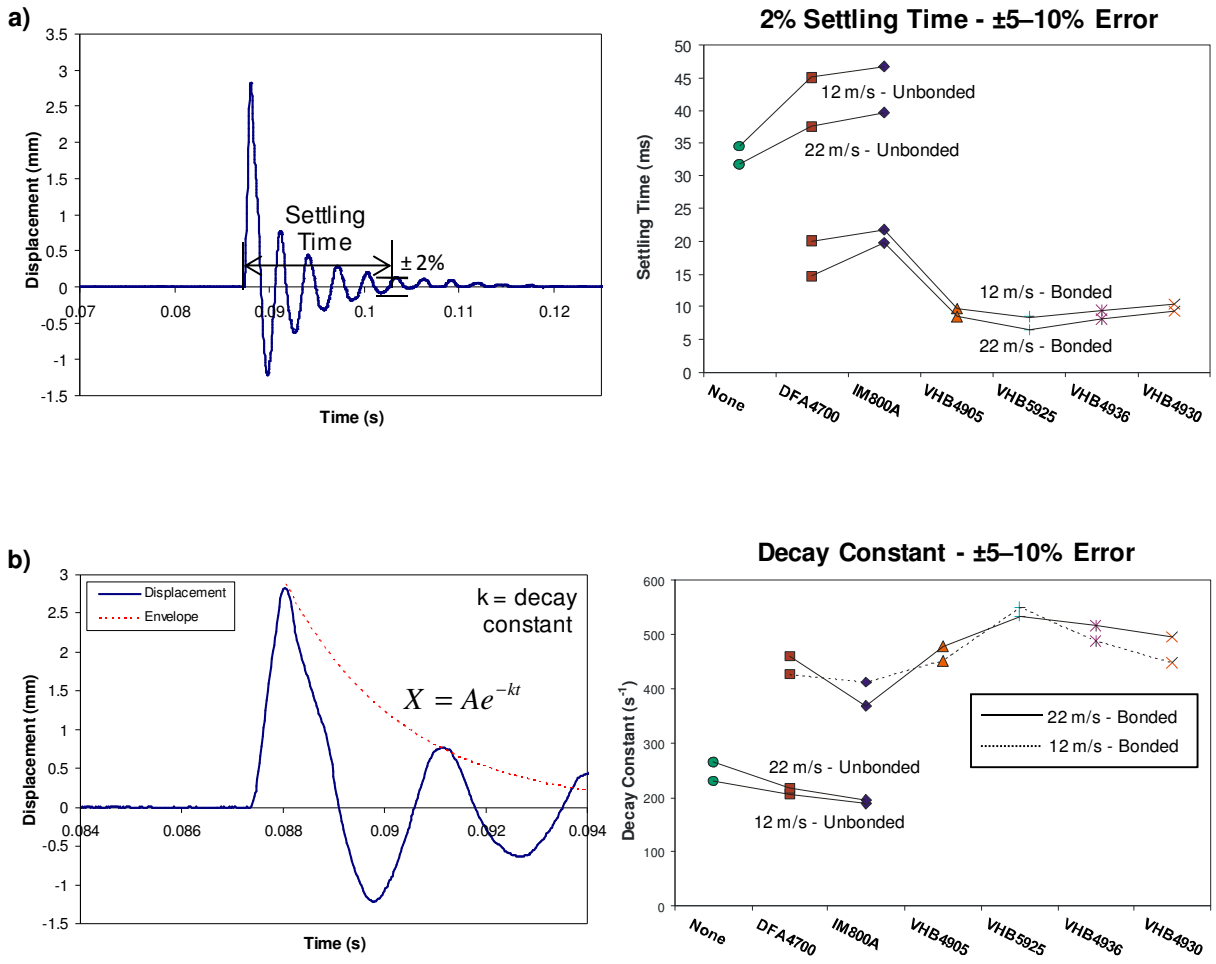

Figure 6.2.3 Metric results for a) 2% settling time and b) decay rate

6.3 Correlation of Fracture to Quasi-Static Response

Some trends were able to be correlated between mechanical interlayer characterization, force and displacement metrics, and observed fracture/damage. Overall, it is not possible to identify a single metric or property that correlates with impact performance for multi-layered structures. This makes it challenging to quantify and target properties that should be improved (via synthesis/material tailoring) for increasing fracture resistance and impact performance. It is clear that full field analysis is critical during impact testing to allow for accounting of energy conversion/dissipation and fracture mechanisms. It is easy for a single metric which contains a fraction of the analysis to lead analysts astray. For example, it appears that there is a trend between fracture and interlayer glass transition temperature (Figure 6.3.1a, b). Impact testing results for this specimen geometry, impact velocities, and impactor mass indicate that adhesives with lower T_g's yield a multi-laminate with longer average crack lengths. Despite this, data from additional interlayers and further impact testing is necessary to make this type of general conclusion. The following figures further illustrate the futility of using simple, material characteristics to predict damage trends. As shown in Figure 6.3.1c, d, the average crack length doesn't correlate to interlayer quasi-static tensile modulus for either impact velocity. With interlayer rate dependence, it is not surprising that no conclusion may be reached based on tensile compliance. This reinforces the idea that the analysis of impact events is very complicated and cannot be simplified to directly relate impact performance with quasi-static material properties. As discussed in Section 2.2.1, a metric utilized for comparison between interlayers' tensile testing results is the normalized hysteresis loop area. It was anticipated that materials that couldn't effectively scale energy dissipation mechanisms with strain rate would have poor impact performance. In other words, the materials with the smallest relative increase in loop area would have the largest fracture areas and cracks. As shown in Figure 6.3.1e, f, this was true in the case of IM 800A which had the smallest increase in loop area and the second largest average cracks. In the case of VHB 5925, the normalized loop area is in the same regime as VHB 4936, VHB 4930, and DF A4700; all of which have small average crack lengths. In fact, the relationship that linked the tensile rate response with impact performance is not loop area, but decreasing residual strain with increasing strain rate. Both IM 800A and VHB 5925 were different than the other four interlayers in this regard (Figure 2.2.1).

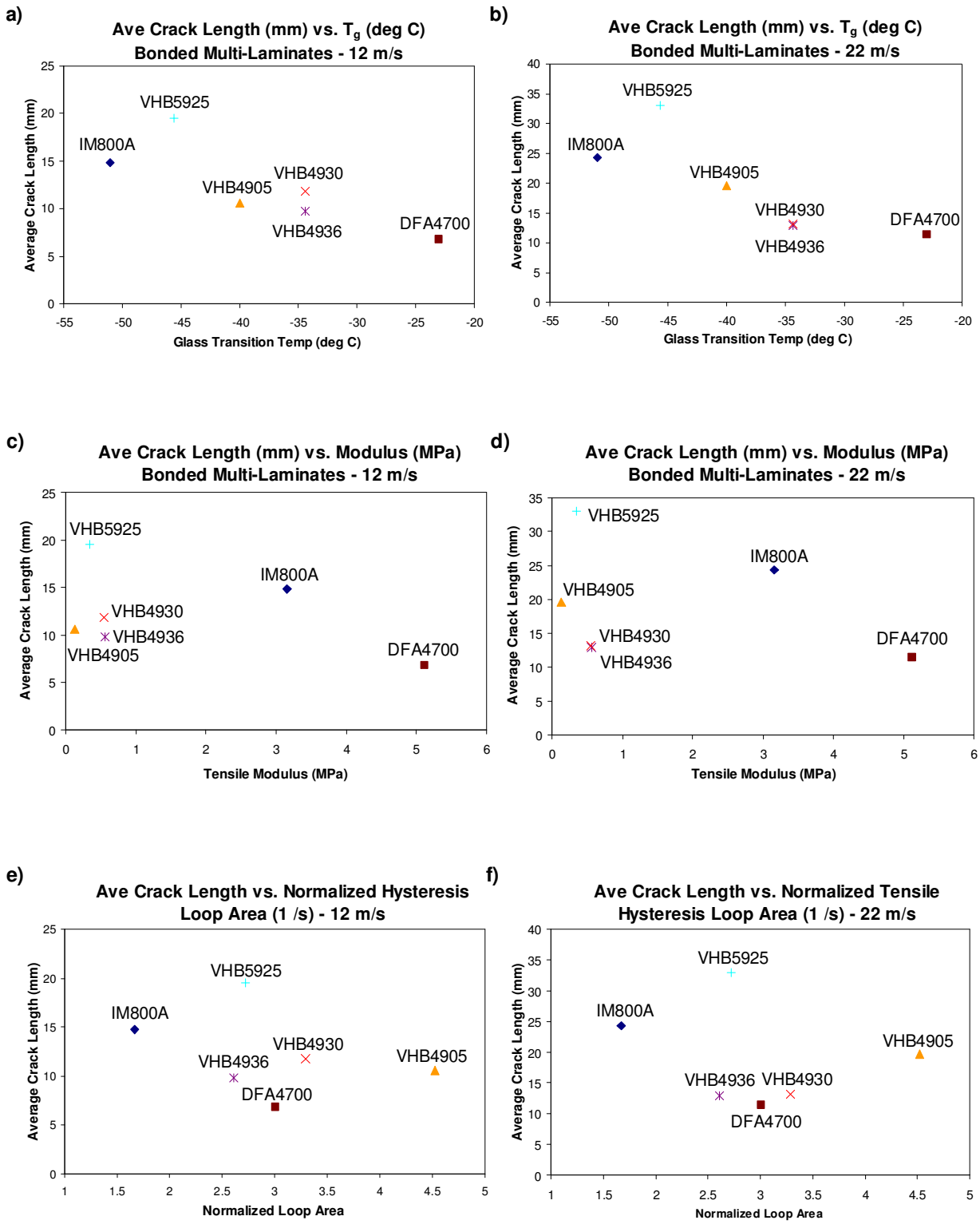

Figure 6.3.1 Average crack length of bonded multi-laminates as a function of glass transition temperature a) 12 m/s and b) 22 m/s, tensile modulus c) 12 m/s and d) 22 m/s, and normalized loop area e) 12 m/s and f) 22 m/s

In summary, causality cannot be implied due to links observed between individual metrics and fracture. Future mechanical characterization and impact tests are required to further probe these ideas and verify true correlations. Overall, several energy absorption and fracture mechanisms are characterized in this thesis. If stress thresholds are exceeded for these testing conditions and specimen geometry, fracture occurs. As discussed throughout this chapter, by measuring and analyzing metrics, a better understanding of the impact mechanics causing fracture is obtained. A combination of analyses of quantitative metrics and observed fracture mechanisms allows in-depth understanding of why some multi-laminates have more or less fracture than others. Intermediate impact velocity testing of PMMA and PC incorporated into multi-laminates with a soft, rate dependent TPU or polyacrylate interlayer has shown that impact performance is complicated by several parameters and is not as easily characterized or predictable as monolithic samples. This thesis presented the first systematic study of the role of the interlayer in modulating impact of tough thermoplastic multi-laminates. A summary of observations and research conclusions are presented in the following chapter.

Chapter 7

Summary

The normal impact response of multi-layered, rate dependent polymer structures is complex and not well understood. This research focuses on gaining insight into impact mechanics of polymer multi-laminates by relating material mechanical characterization, measured quantitative force and displacement metrics, and qualitative energy absorption mechanisms and observed fracture. Extensive research has been conducted on monolithic outerlayer components (PMMA and PC) at quasi-static strain rates (less than 1 s^{-1}), low velocities with drop towers/pendulums (impact velocities ranging 2–8 m/s), high velocities with gas guns (50–500 m/s), and very high strain rates using SHPBs (greater than 10^3 s^{-1}) (Section 1.4). Few have focused on intermediate rate testing of polymers, and even less on multi-layered polymers. Furthermore, the rate-sensitive behavior of rubbery elastomers is still an area of extensive research despite the first papers on the subject were written 70 years ago. This appears to be the first description of the rate-dependent response of polyacrylate elastomers, which are filled polymers differing from the usually studied carbon-black filled rubbers. To the author's knowledge, this is also the first attempt to characterize the impact mechanics of an all-polymer multi-layered system, using an instrumented experimental setup in an intermediate impact velocity regime.

Six polymer interlayers with varying microstructures and properties are mechanically characterized by examining rate dependence in tension, and analyzing quasi-static response in compression and shear adhesion (Chapter 2). The interlayers include two TPUs (DF A4700 and IM 800A) and four 3M polyacrylate elastomers (VHB 4905, VHB 5925, VHB 4936 and VHB 4930). An instrumented gas gun is used to impact fully clamped 161.29 cm^2 square samples (12.7 cm sides) impacted by a 28.5 gram steel impactor travelling at 12 m/s and 22 m/s (impact energies of approximately 2 and 7 J respectively). In total, nine configurations are impacted including: a two-layer PMMA/PC multi-laminate (control), three-layered unbonded samples (both TPUs), and six bonded three-layered multi-laminates (all interlayers). The experimental setup is modeled from several researchers who have previously used instrumented impactors in

conjunction with a gas gun for impact testing [64-65]. The novelty of the setup is that force and displacement during impact are recorded independently using a shock accelerometer inserted in the impactor and optical displacement sensors measuring multi-laminate out-of-plane deflection. Note that full field displacement measurements would be optimal over single point measurements, such as high speed digital image correlation (DIC) [27]. A LabVIEW virtual instrument is developed to coordinate operation of the experimental setup and ensure that data is aligned temporally (Section 4.2.1). Ten quantitative metrics are measured from the force and displacement traces for comparison between samples. Force metrics include: first force peak, loading rate, local minimum force, second force peak, loading pulsewidth, and impulse (Section 6.1). Displacement metrics include: maximum displacement, transient response frequency, 2% settling time, and decay rate (Section 6.2). Energy conversion/dissipation mechanisms and fractography is completed post-impact and used for comparison between impact velocities, boundary conditions, and interlayers (Section 5.2). Mechanical characterization of the interlayers is correlated to quantitative force/displacement metrics and damage/fracture to analyze the influence of the interlayer on impact performance.

7.1 Conclusions

The research conclusions reached are summarized below:

Material Characterization (Chapter 2)

- Supplier provided material properties and microstructure of interlayers correlate to mechanical material response in tension and compression
    - TPUs are much less compliant than VHBs in tension (significantly) and compression (somewhat)
    - Similarities are observed in tensile responses for polyacrylates with rigid microsphere inclusions (VHB 4936 and VHB 4930)
    - Similarities are observed in compressive responses for compressible polyacrylates (VHB 5925 and VHB 4936)
    - Incompressible VHB 4905 is more compliant in tension than VHB 5925, but the opposite is true for compression

- Tensile rate dependence is observed for all interlayers showing decreasing compliance with increasing strain rate
- All interlayers display non-linearity and hysteretic behavior showing increasing loop area with strain rate
- TPUs display cyclic softening in tension and the response is dependent on loading history
- All interlayers show increasing residual strain with strain rate in tension except for IM 800A and VHB 5925, which display decreasing residual strains with rate
- A Mooney-Rivlin model is able to fit experimental loading tensile data very well
- TPUs have superior shear strength over VHB polyacrylates, but completely delaminate at low shear strains
    - VHB 5925, VHB 4936, and VHB 4930 never delaminate and only show bond weakening at shear strains of approximately 8.0
    - Local, small delaminations throughout the VHB 4905 bondline cause severe bond weakening at shear strains similar to the TPUs of approximately 3.5

Experimental Setup and LabVIEW VI (Chapter 4)

- An instrumented gas gun with a shock accelerometer embedded impactor is able to consistently yield contact force traces during impact on low modulus materials
    - Although wireless technology was investigated, a consistent and repeatable method for loading a wired accelerometer is accomplished
- Accurate temporal alignment between multiple sensors is attainable by setting a common "zero time" utilizing a digital trigger
- A MATLAB smoothing function is capable of smoothing electrical noise from force data without altering shape or amplitude

Energy Absorption Mechanisms and Fractography (Chapter 5)

- Elastic deflection is a main energy absorption mode for the tested specimen geometry and impact speeds resulting in reloading of the impactor (two force peaks)
- Bonded specimens dissipate impact energy through: impact site local plastic deformation, elastic deflection, and small intralayer cracks propagating from the impact site (PMMA)

- Unbonded specimens dissipate impact energy through: large global fracture in the form of brittle cracks emanating from the impact site, petaling, local plastic deformation in sections separated from the center, and elastic deflection
- Bonding of interlayers increases interfacial shear strength, effectively enhancing stiffness resulting in:
    - Larger force peaks, loading rates, loading impulses, and response frequencies
    - Lower loading pulsewidths, settling times, and maximum displacements
- IM 800A and VHB 5925 bonded multi-laminates have the worst impact performance with the longest radial cracks and largest damage/fracture areas
- Bonded multi-laminates with solid acrylic VHB 4905 and VHB 4930 interlayers were the only samples to delaminate for the impact speed of 22 m/s
    - No delaminations observed in any configurations for impact velocity of 12 m/s
    - Delamination is unrelated to just quasi-static shear adhesion strength results

Quantitative Metric Analysis (Chapter 6)

- Trends observed within a metric mostly scale for both impact velocities
- First force peak and loading rate are heavily influenced by the PMMA and PC outerlayers and effective stiffness of the multi-laminate
- Large loading pulsewidth and maximum displacement, and low second force peak, are three metrics that directly correlate to damage
    - For a given impact velocity, longer contact with the multi-laminate allows for more fracture and longer crack propagation
    - Substantial out-of-plane deflections result in fracture thresholds being surpassed, resulting in increased fracture
    - Reloading force is indicative of the structural integrity of the multi-laminate and its ability to dissipate impact energy in various ways besides fracture
- Samples with high transient response frequencies have large decay rates and quick 2% settling times
- Decay rate is larger for 22 m/s than 12 m/s impact for all interlayers tested except IM 800A and VHB 5925

    - Correlates to increased elasticity with strain rate observed in tensile response not observed with the other four interlayers
- An interlayer that doesn't effectively scale energy dissipation (small tensile hysteresis loop area increase) with strain rate could result in poor impact performance (IM 800A)
- A very low modulus adhesive in a multi-laminate with low adhesion strength doesn't necessarily imply increased fracture under impact (VHB 4905)
- Interlayers with similar material properties and quasi-static mechanical responses, but with slightly different microstructures, will have different energy absorption mechanisms and quantitative metric results (VHB 4936 and VHB 4930)

This research has shown that the impact mechanics of a multi-layered structure containing rate dependent components is a complicated problem. Quantitative metrics and fracture observations have shown that two interlayers, IM 800A and VHB 5925, with very different mechanical responses, properties, and microstructures could both yield poor impact performance. IM 800A, a tough thermoplastic polyurethane, is the second least compliant interlayer in both tension and compression with the second strongest shear adhesion strength (behind DF A4700). VHB 5925 is the second most compliant interlayer in tension, the softest in compression, and has the second weakest shear adhesion strength. Despite these differences, similarities were observed that carried through this analysis to correlate impact performance with material characterization results and force/displacement metrics. These similarities include: decreasing residual strains with increasing tensile strain rate, low second force (reload) and local minimum peaks, large loading pulsewidth, impulse, and maximum displacement, and extreme settling times and decay rates (Chapter 6). Observation and analysis of what is desirable of force and displacement metrics (high/low) for optimal impact performance has resulted in a better understanding of impact mechanics of multi-layered systems. By no means is causality implied, in that a single metric or characteristic cannot be directly related to fracture or predict impact performance. Instead, this research has highlighted trends and correlations observed in an attempt to analyze complementary aspects of a very complex impact response of a multi-layered system. In summary, an experimental setup instrumented to measure contact force and displacement has been shown to provide insight into the impact mechanics and energy dissipation mechanisms of rate dependent multi-layered samples consisting of PMMA and PC with a soft interlayer.

7.2 Future Work

In order to gain further insight into multi-laminate impact mechanics and truly state causality in the metric and fracture trends observed, the range of impact velocities tested and strain rates for mechanical testing of the interlayers must be expanded. In general, continuation of this study should focus on expanding the scope of impact analysis and material characterization.

Specific suggestions for future research directions include:

Material Characterization

- Loading in tension, compression, and shear adhesion for a wider range of strain rates to further analyze rate dependence
    - Further investigate the optimal method for examining adhesion strength at intermediate strain rates comparable to the impact speeds tested (100 s^{-1}), as well as higher strain rates using a SHPB
- Cyclic tensile testing for the four VHB polyacrylates, and cyclic compression testing for all interlayers, to examine the effect of loading history on material response and observe how energy dissipation mechanisms evolve with strain rate
- Characterize the adhesion strength of each interlayer with respect to PMMA and PC individually to increase accuracy of modeled delaminations during impact

Experimental Setup

- Full-field displacement of the multi-laminate using high-speed cameras and digital image correlation (DIC) allowing for complete deflection characterization
- Improve the velocity sensor to increase robustness, accuracy, and reliability
- Further investigate feasibility of a wireless impactor capable of recording contact force and possibly utilize a force transducer instead of a shock accelerometer

References

1. Patel, P.J., et al., *Transparent Ceramics for Armor and EM Window Applications.* Proceedings of SPIE, 2000. **4102**: p. 1-14.
2. Patel, P.J., et al., *Transparent Armor.* The AMPTIAC Newsletter, 2000. **4**(3): p. 1-13.
3. Sands, J.M., et al., *Protecting the Future Force: Transparent Materials Safeguard the Army's Vision*. Vol. 8 No. 4 ed. Vol. The AMPTIAC Quarterly. 2004.
4. Illinger, J.L., *Effect of Interlayer on Impact Resistance of Acrylic/Polycarbonate Laminates.* 1972: p. 1-15.
5. Illinger, J.L. and R.W. Lewis, *Effect of Adhesive Structure on Impact Resistance and Optical Properties of Acrylic/Polycarbonate Laminates.* Polymer Preprints, 1975. **16**(1): p. 545-550.
6. Hsieh, A.J., et al., *The Effects of PMMA on Ballistic Impact Performance of Hybrid Hard/Ductile All-Plastic-and Glass-Plastic-Based Composites.* 2004.
7. Hsieh, A.J. and J.W. Song, *Measurements of Ballistic Impact Response of Novel Coextruded PC/PMMA Multilayered-Composites.* Journal of Reinforced Plastics and Composites, 2001. **20**(3): p. 239-254.
8. Song, J.W. and A.J. Hsieh, *Ballistic Impact Resistance of Monolithic, Hybrid and Nano Composites of PC and PMMA.* Proceedings of the American Society for Composites, 17th Technical Conference, 2002.
9. Toqueboeuf, W., B. Mortaigne, and C. Cottenot, *Dynamic Behaviour of Polycarbonate/Polyurethane Multi-Layer for Transparent Armor.* Journal De Physique IV, 1997. **7**.
10. Cros, P.E., et al. *Experimental and numerical analysis of the impact behaviour of polycarbonate and polyurethane multilayer*. 2000. France: EDP Sciences.
11. Qi, H.J. and M.C. Boyce, *Stress-Strain Behavior of Thermoplastic Polyurethanes.* Mechanics of Materials, 2005. **37**(8): p. 817-839.
12. Sarva, S.S., et al., *Stress-strain behavior of a polyurea and a polyurethane from low to high strain rates.* Polymer, 2007. **48**(8): p. 2208-2213.
13. Yi, J., et al., *Large deformation rate-dependent stress-strain behavior of polyurea and polyurethanes.* Polymer, 2006. **47**(1): p. 319-29.
14. Roland, C.M., et al., *High strain rate mechanical behavior of polyurea.* Polymer, 2007. **48**(2): p. 574-578.
15. Arruda, E.M., M.C. Boyce, and R. Jayachandran, *Effects of strain rate, temperature and thermomechanical coupling on the finite strain deformation of glassy polymers.* Mechanics of Materials, 1995. **19**(2-3): p. 193-212.
16. Blumenthal, W.R., et al., *Influence of Temperature and Strain Rate on the Compressive Behavior of PMMA and Polycarbonate Polymers.* AIP Conference Proceedings, 2002. **620**(1): p. 665-665.
17. Cheng, S.-K. and C.-Y. Chen, *Mechanical properties and strain-rate effect of EVA/PMMA in situ polymerization blends.* European Polymer Journal, 2004. **40**(6): p. 1239-1248.
18. Chou, S., K. Robertson, and J. Rainey, *The effect of strain rate and heat developed during deformation on the stress-strain curve of plastics.* Experimental Mechanics, 1973. **13**(10): p. 422-432.

19. Frank, O. and J. Lehmann, *Determination of Various Deformation Processes in Impact-Modified PMMA.* Colloid and Polymer Science, 1986. **264**(6): p. 473-481.
20. Li, Z. and J. Lambros, *Strain Rate Effects on the Thermomechanical Behavior of Polymers.* International Journal of Solids and Structures, 2001. **38**: p. 3549-3562.
21. Mulliken, A.D. and M.C. Boyce, *Mechanics of the Rate-Dependent Elastic-Plastic Deformation of Glassy Polymers from Low to High Strain Rates.* International Journal of Solids and Structures, 2006. **43**(5): p. 1331-1356.
22. Richeton, J., et al., *Influence of Temperature and Strain Rate on the Mechanical Behavior of Three Amorphous Polymers: Characterization and Modeling of the Compressive Yield Stress.* International Journal of Solids and Structures, 2006. **43**(7-8): p. 2318-2335.
23. Sarva, S., A.D. Mulliken, and M.C. Boyce, *Mechanics of Taylor impact testing of polycarbonate.* International Journal of Solids and Structures, 2007. **44**(7-8): p. 2381-2400.
24. Shah, Q.H., *Impact resistance of a rectangular polycarbonate armor plate subjected to single and multiple impacts.* International Journal of Impact Engineering, 2009. **36**(9): p. 1128-1135.
25. Shah, Q.H. and Y.A. Abakr, *Effect of distance from the support on the penetration mechanism of clamped circular polycarbonate armor plates.* International Journal of Impact Engineering, 2008. **35**(11): p. 1244-50.
26. Fleck, N.A., W.J. Stronge, and J.H. Liu, *High Strain-Rate Shear Response of Polycarbonate and Polymethyl Methacrylate.* Proceedings of the Royal Society of London. Series A, Mathematical and Physical Sciences, 1990. **429**(1877): p. 459-479.
27. Gunnarsson, C.A., et al. *Deformation and Failure of Polycarbonate During Impact as a Function of Thickness*. in *SEM Annual Conference*. 2009. Albuquerque, NM.
28. Kohlman, W.G., *Ballistic performance of polycarbonate/polyester and polycarbonate/styrene-acrylonitrile microlayer sheets.* Polymer Engineering and Science, 1995. **35**(14): p. 1191-1195.
29. Kohlman, W.G. and S.P. Petrie, *Mechanical properties of polycarbonate. Polysulfone and polycarbonate-polyetherimide blends.* Advances in Polymer Technology, 1995. **14**(2): p. 111-111.
30. Wright, S.C., N.A. Fleck, and W.J. Stronge, *Ballistic Impact of Polycarbonate - An Experimental Investigation.* International Journal of Impact Engineering, 1993. **13**(1): p. 1-20.
31. Moy, P., T. Weerasooriya, and W. Chen, *Strain Rate Response of a Polycarbonate Under Uniaxial Compression.* Proceedings of SEM Annual Conference on Experimental Mechanics, 2003.
32. Radin, J. and W. Goldsmith, *Normal projectile penetration and perforation of layered targets.* International Journal of Impact Engineering, 1988. **7**(2): p. 229-259.
33. Rittel, D., *A Note on the Dynamic Failure of PMMA.* International Journal of Fracture, 2000. **106**(2): p. 3-8.
34. Moy, P., et al., *Dynamic Stress-Strain Response and Failure Behavior of PMMA.* Proceedings of 2003 ASME IMECE, 2003.
35. Sarva, S., A.D. Mulliken, and M.C. Boyce, *Mechanics of Transparent Polymeric Material Assemblies Under Projectile Impact: Simulations and Experiments.* 2004.
36. Song, J.W., et al., *Aromatic Nylons for Transparent Armor Applications*. 2006.

37. Gama, B.A., et al., *Effect of Non-Linear Material Behavior on the Through-Thickness Stress Wave Propagation in Multi-Layer Hybrid Lightweight Armor.* Advances in Computational and Engineering Sciences - Technical Science Press, 2000.
38. Ball, A., *The Low Velocity Impact Behaviour of Glass-Polymer Laminated Plates.* Journal De Physique IV, 1997. **7**(C3): p. 921-926.
39. Ball, A. and H.W. McKenzie, *On the Low Velocity Impact Behaviour of Glass Plates.* Journal De Physique IV, 1994. **4**(C8): p. 783-788.
40. Choi, H.Y., R.J. Downs, and F.-K. Chang, *A New Approach Toward Understanding Damage Mechanisms and Mechanics of Laminated Composites Due to Low-Velocity Impact: Part I - Experiments.* Journal of Composite Materials, 1991. **25**: p. 992-1009.
41. Sun, C.T. and S. Rechak, *Effect of Adhesive Layers on Impact Damage in Composite Laminates.* ASTM Special Technical Publication, 1988. **972**: p. 97-123.
42. Kerns, J., et al., *Comparison of Irreversible Deformation and Yielding in Microlayers of Polycarbonate with Poly(methylmethacrylate) and Poly(styrene-co-acrylonitrile).* Journal of Applied Polymer Science, 2000. **77**(7): p. 1545-1557.
43. Richards, M., R. Clegg, and S. Howlett. *Ballistic Performance Assessment of Glass Laminates Through Experimental and Numerical Investigation*. in *18th International Symposium and Exhibition on Ballistics*. 1999. San Antonio, TX.
44. Fountzoulas, C.G., et al. *A Computational Study of Laminate Transparent Armor Impacted by FSP*. in *23rd International Symposium on Ballistics*. 2007. Tarragona, Spain.
45. Cheresh, M.C. and S. McMichael, *Instrumented Impact Test Data Interpretation.* Instrumented Impact Testing of Plastics and Composite Materials, 1987. **ASTM STP 936**: p. 9-23.
46. Ireland, D.R., *Procedures and Problems Associated with Reliable Control of the Instrumented Impact Test.* Instrumented Impact Testing, 1974. **ASTM STP 563**: p. 3-29.
47. Ambur, D.R., J.H. Starnes, and C.B. Prasad, *Influence of Impact Parameters on the Response of Laminated Composite Plates.* ASTM Special Technical Publication, 1995. **1230**(389-404).
48. Lee, L.J., K.Y. Huang, and Y.J. Fann, *Dynamic Responses of Composite Sandwich Plate Impacted by a Rigid Ball.* Journal of Composite Materials, 1993. **27**(13): p. 1238-1256.
49. Nairn, J.A., *Measurement of Polymer Viscoelastic Response During an Impact Experiment.* Polymer Engineering and Science, 1989. **29**(10): p. 654-661.
50. Prasad, C.B., D.R. Ambur, and J.H. Starnes, *Response of Laminated Composite Plates to Low-Speed Impact by Airgun-Propelled and Dropped-Weight Impactors.* AIAA/ASME Structures, Structural Dynamics and Materials Conference, 1993. **2**: p. 887-900.
51. Sjoblom, P.O. and J.T. Hartness, *On Low-Velocity Impact Testing of Composite Materials.* Journal of Composite Materials, 1988. **22**: p. 30-52.
52. Zee, R.H., et al., *Ballistic Response of Polymer Composites.* Polymer Composites, 1991. **12**(3): p. 196-202.
53. Aga, Z.A. and E. Woldesenbet, *Bond Thickness Effect on Impact Response and Damage of Adhesively-Boned Graphite/Epoxy Composites.* Journal of Adhesion Science Technology, 2007. **21**(1): p. 21-34.
54. Collombet, F., et al. *Damage criteria for the study of impacted composite laminates*. 1998. UK: Elsevier.
55. Rogers, M.G. and A. Plumtree, *A comparison of Charpy and Izod test modes for polystyrene.* Polymer Testing, 1992. **11**(1): p. 13-21.

56. Weerasooriya, T., P. Moy, and D. Casem, *Fracture Toughness of PMMA as a Function of Loading Rate.* Proceedings of the 2006 SEM Annual Conference on Experimental Mechanics, 2006.
57. Kamal, M.R., et al., *Evaluation of a Variable-Speed Impact Tester for Analysis of Impact Behavior.* Instrumented Impact Testing of Plastics and Composite Materials, 1986. **ASTM STP 936**: p. 58-80.
58. Peraro, J.S., *Prediction of End-Use Impact Resistance of Composites.* Instrumented Impact Testing of Plastics and Composite Materials, 1986. **ASTM STP 936**: p. 187-216.
59. Lammerant, L., I. Verpoest, and A. Vlot, *The Strain Rate Dependence of Mechanical Properties of Composites During Monotonic and Impact Loading.* Proceedings of ICCM 8, 1991: p. 32-K-1:32-K-7.
60. Roach, A.M., K.E. Evans, and N. Jones, *The Penetration Energy of Sandwich Panel Elements Under Static and Dynamic Loading. Part I.* Composite Structures, 1998. **42**(2): p. 119-134.
61. Roach, A.M., K.E. Evans, and N. Jones, *The Penetration Energy of Sandwich Panel Elements Under Static and Dynamic Loading. Part II.* Composite Structures, 1998. **42**: p. 135-152.
62. Vaidya, U.K., et al., *Ballistic Response of Graphite/Epoxy Composite Backed Polycarbonate Plates.* International SAMPE Techincal Conference, 1999. **31**: p. 77-84.
63. Yadav, S. and G. Ravichandran, *Penetration Resistance of Laminated Ceramic/Polymer Structures.* International Journal of Impact Engineering, 2003. **28**(5): p. 557-574.
64. Delfosse, D., et al., *Instrumented Impact Testing at High Velocities.* Journal of Composites Technology & Research, 1993. **15**(1): p. 38-45.
65. Levy, N. and W. Goldsmith, *Normal impact and perforation of thin plates by hemispherically-tipped projectiles -- II. Experimental results.* International Journal of Impact Engineering, 1984. **2**(4): p. 299-324.
66. Kolsky, H., *An Investigation of the Mechanical Properties of Materials at Very High Rates of Loading.* Proceedings of the Physical Society B, 1949. **62**: p. 676-700.
67. Tasdemirci, A., I.W. Hall, and B.A. Gama, *Stress Wave Propagation Effects in Two- and Three-Layered Composite Materials.* Journal of Composite Materials, 2004. **38**(12): p. 995-1009.
68. Gama, B.A., et al., *Innovative Design and Ballistic Performance of Lightweight Compostie Integral Armor*, in *SAE 2001 World Congress*. 2001, SAE: Detroit, MI.
69. Tasdemirci, A. and I.W. Hall, *Experimental and Modeling Studies of Stress Wave Propagation in Multilayer Composite Materials: Low Modulus Interlayer Effects.* Journal of Composite Materials, 2005. **39**(11): p. 981-1005.
70. Martinez, M.A., et al., *Confined Compression of Elastic Adhesives at High Rates of Strain.* International Journal of Adhesion and Adhesives, 1998. **18**(6): p. 375-383.
71. Sanchez-Adsuar, M.S. and J.M. Martin-Martinez, *Structure, Composition, and Adhesion Properties of Thermoplastic Polyurethane Adhesives.* Journal of Adhesion Science Technology, 2000. **14**(8): p. 1035-1055.
72. MacAloney, N. and N.C. Goulbourne, *Viscoelastic Characterization of Aliphatic Polyurethane Interlayers.* 2007: p. 1-36.
73. Richeton, J., et al., *A formulation of the cooperative model for the yield stress of amorphous polymers for a wide range of strain rates and temperatures.* Polymer, 2005. **46**(16): p. 6035-6043.

74. Beatty, M.F. and S. Krishnaswamy, *A theory of stress-softening in incompressible isotropic materials.* Journal of the Mechanics and Physics of Solids, 2000. **48**(9): p. 1931-1965.
75. DeSimone, A., J.-J. Marigo, and L. Teresi, *A damage mechanics approach to stress softening and its application to rubber.* European Journal of Mechanics - A/Solids. **20**(6): p. 873-892.
76. Dorfmann, A. and R.W. Ogden, *A constitutive model for the Mullins effect with permanent set in particle-reinforced rubber.* International Journal of Solids and Structures, 2004. **41**(7): p. 1855-1878.
77. Krishnaswamy, S. and M.F. Beatty, *The Mullins effect in compressible solids.* International Journal of Engineering Science, 2000. **38**(13): p. 1397-1414.
78. Goulbourne, N., et al. *Modeling of a dielectric elastomer diaphragm for a prosthetic blood pump*. 2003. San Diego, CA, USA: SPIE.
79. Goulbourne, N.C., M.I. Frecker, and E. Mockensturm. *Electro-elastic modeling of a dielectric elastomer diaphragm for a prosthetic blood pump*. 2004. San Diego, CA, USA: SPIE.
80. Kofod, G., *Dielectric Elastomer Actuators*, in *Department of Chemistry*. 2001, The Technical University of Denmark.
81. Chen, F.-K. and C.-J. Chen, *On the Nonuniform Deformation of the Cylinder Compression Test.* Journal of Engineering Materials and Technology, 2000. **122**(2): p. 192-197.
82. Kihara, K., et al., *A study and evaluation of the shear strength of adhesive layers subjected to impact loads.* International Journal of Adhesion and Adhesives, 2003. **23**(4): p. 253-259.
83. Yokoyama, T. and H. Shimizu, *Evaluation of Impact Shear Strength of Adhesive Joints with the Split Hopkinson Bar.* JSME International Journal, 1998. **41**(4).
84. Srivastava, V., et al., *Effect of Loading Rate and Geometry Variation on the Dynamic Shear Strength of Adhesive Lap Joints*. 2004. p. 769-780.
85. Srivastava, V., A. Shukla, and V. Parameswaran, *Experimental Evaluation of the Dynamic Shear Strength of Adhesive-Bonded Lap Joints.* Journal of Testing and Evaluation, 2000. **28**(6): p. 438-442.
86. Guedes Pinto, A.M., et al., *Shear strength of adhesively bonded polyolefins with minimal surface preparation.* International Journal of Adhesion and Adhesives, 2008. **28**(8): p. 452-456.
87. Harris, J.A. and R.D. Adams, *An assessment of the impact performance of bonded joints for use in high energy absorbing structures.* ARCHIVE: Proceedings of the Institution of Mechanical Engineers, Part C: Mechanical Engineering Science 1983-1988 (vols 197-202), 1985. **199**(23): p. 121-131.
88. Chalkley, P.D. and W.K. Chiu, *An improved method for testing the shear stress/strain behaviour of adhesives.* International Journal of Adhesion and Adhesives, 1993. **13**(4): p. 237-242.
89. Rai, K.N. and D. Singh, *Impact resistance behavior of polymer nanocomposite transparent panels.* Journal of Composite Materials, 2009. **43**(2): p. 139-51.
90. Garland, P.P. and R.J. Rogers, *An experimental study of contact forces during oblique elastic impact.* Journal of Applied Mechanics, 2009. **76**(3): p. 031015 (8 pp.).

Appendix A: Mathematica Codes

A.1 Mathematica file for calculating hysteresis loop areas

SetDirectory[“Directory”] *Define directory where file is located*

data1=Import["File Name.xls"]; *Import excel file*

data1=data1[[1]];

dt=t; *Define time between data points*

initial=X; *First data point*

final=Y; *Last data point*

sum1=Table[dt/2 (data1[[i]]+data1[[i+1]]),{i,initial,final-1}];

sum2=Sum[sum1[[i]],{i,1,Length[sum1]}]

Algorithm for calculation of area using the formula for trapezoid area:

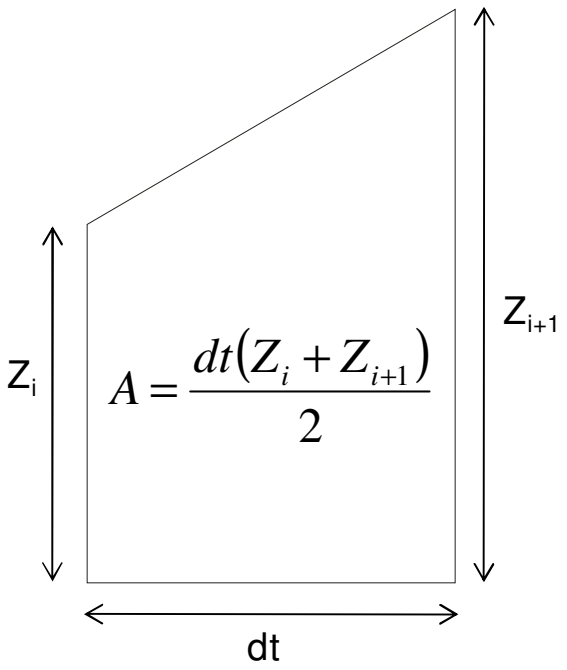

A.2 Mathematica file for fitting a Mooney-Rivlin model to the tensile loading data

Area=3.175*0.635*10^{-6}; *Calculate cross-sectional area*

f=Area*(2 C1-2 C2/λ1) (λ1-1/$λ1^2$)/.C2→-C2

Fitting function for uni-axial force in terms of stretch and two constants (C1 and C2)

SetDirectory["Directory"] *Define directory where file is located*

data=Import["File Name.xls"]; *Import tensile data*

fit=NonlinearModelFit[data[[1]],f,{C1,C2},λ1];

Fit experimental data with function defined previously as "f" and solve for constants

fit["BestFitParameters"] *Output constants*

f1[λ1_]=fit["BestFit"] *Output fitting function with calculated constants and area*

fit["RSquared"] *R-squared value representing accuracy of fit*

DataPlot=ListPlot[data[[1]]];

ModelPlot=Plot[f1[x],{x,1,2}];

Show[DataPlot,ModelPlot]

Representative output with data points being experimental data and a line fit:

{C1→4.36402×10^6,C2→7.75941×10^7}

2.01612×10^{-6} (8.72805×10^6+1.55188×10^8/λ1) (-(1/$λ1^2$)+λ1)

0.999755

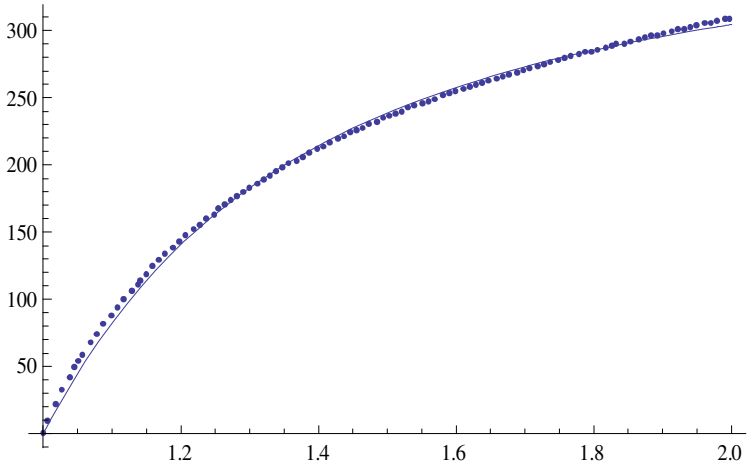

data1=Table[f1[λ1],{λ1,1,2,0.05}]; *Define what to export including bounds and time step (0.05)*

Export["File Name.xls",data1,"Table"] *Export data file*

Appendix B: Dynamic Shear Adhesion Bracket

B.1 Cutaway schematic of steel bracket to retrofit experimental setup for shear impact

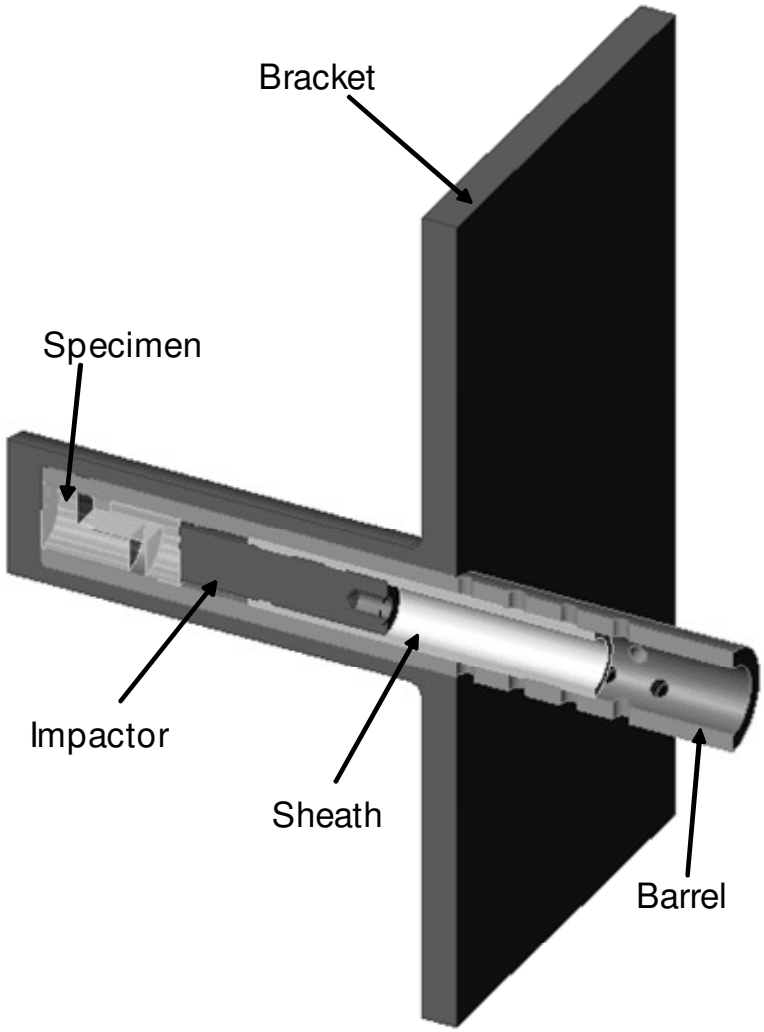

Appendix C: Force and Displacement Metric Summary

C.1 Complete quantitative metric results

Component Materials	Boundary Condition	Impact Speed (m/s)	1st Force Peak (N)	Loading Rate (N/s)	Local Minimum (N)	2nd Force Peak (N)	Loading Pulsewidth (ms)	Loading Impulse (Ns)	Maximum Displacement (mm)	Response Frequency (Hz)	2% Settling Time (ms)	Decay Constant (s^{-1})
PMMA/PC	Un-Bonded	12.2	413.7	4812	141.25	390.2	1.954	N/A	6.22	178.9	34.4	229.9
PMMA/PC	Un-Bonded	22.1	818.1	11126	194	669.1	1.641	N/A	8.15	165.8	31.6	263.3
PMMA/DF/PC	Un-Bonded	11.7	349.7	3426	76.2	341	1.36	N/A	4.84	162.1	45	205.8
PMMA/DF/PC	Un-Bonded	22.7	1004.4	12820	178.2	742	1.1	N/A	7.81	172.1	37.5	216.1
PMMA/IM/PC	Un-Bonded	12.2	359.7	3081	79.7	357.5	1.339	N/A	5.39	156.5	46.8	187.4
PMMA/IM/PC	Un-Bonded	22.4	939	12851	218.2	599.7	1.138	N/A	8.11	162.9	39.6	195.5
PMMA/DF/PC	Bonded	12.3	521.1	5817	248.6	576.2	0.8	0.321	2.9	340.1	19.9	425.6
PMMA/DF/PC	Bonded	22.7	1138.9	14991	579.7	1171	0.72	0.676	4.79	371.7	14.6	458.9
PMMA/IM/PC	Bonded	12.4	464.4	5204	181.1	382.5	1.109	0.384	3.87	234.2	21.8	409.8
PMMA/IM/PC	Bonded	22.3	1054.8	14554	305.6	773.4	0.991	0.687	5.81	265.3	19.8	368.7
PMMA/VHB4905/PC	Bonded	11.8	410.6	4567	179.1	390.7	0.887	0.28	3.25	244.5	9.71	452
PMMA/VHB4905/PC	Bonded	21.4	994.3	14040	461	913.3	0.777	0.586	5.24	312.5	8.5	478
PMMA/VHB5925/PC	Bonded	11.9	386.8	4395	217.6	369.1	1	0.291	3.75	324	8.43	550.9
PMMA/VHB5925/PC	Bonded	22.1	917.3	12055	418.1	769.1	0.9	0.59	5.63	343.3	6.43	535.8
PMMA/VHB4936/PC	Bonded	12.3	463.7	5363	226.7	510.5	0.715	0.354	2.92	419.1	9.39	488.7
PMMA/VHB4936/PC	Bonded	21.9	945.3	12310	496.5	1029.7	0.677	0.487	4.4	453.4	8.13	515.6
PMMA/VHB4930/PC	Bonded	12.7	466.6	5369	206.4	510.7	0.736	0.261	2.94	412.4	10.4	447.8
PMMA/VHB4930/PC	Bonded	21.9	1015.6	13848	491	1098.8	0.689	0.529	4.88	426	9.19	495.5